Structural Response of Novel PU Structures under Quasi-Static, Impact and Blast Loading - Experimental and Numerical Analyses

Thesis submitted in accordance with the requirements of

the University of Liverpool for the degree of Doctor in Philosophy

by

Adil Jamil

February, 2018

UNIVERSITY OF LIVERPOOL

Abstract

Due to the continuing risks of impacts and explosions and repercussions usually resulting in the loss of life or serious injury, the aim of this research was to develop novel structures that can be applied to scenarios of dynamic loading conditions that would assist in mitigating these risks. Two types of polyurethanes were used in this research, i.e. thermoset polyurethane (TSPU) and thermoplastic polyurethane (TPU). The TSPU allows for easy modification of the microstructure and in this study, hollow glass microspheres (HGMs) were added at different volume percentages to develop a syntactic TSPU material. This led to the development of graded foams, in order to reduce inertial effects in dynamic loading.

The work was extended to investigate reinforcing the TSPU and the TPU matrix with carbon fibre reinforced polymer (CFRP) tubes, providing a higher load-bearing capacity under quasi-static loading. Reinforcing the syntactic TSPU resulted in a 47.7 % increase in specific energy absorption (SEA), with the average value reaching 56.28 kJ/kg under quasi-static loading. In addition to this, the specific compressive strength (σ_c/ρ) increased by 65 % reaching 55 kPa/(kg/m^3).

Further study was carried out on the TPU, taking advantage of the materials versatility. Although, the SEA values of TPU were lower than the TSPU under quasi-static loading conditions, presenting a low modulus and lower plateau stresses, the CFRP reinforced TPU provided greater energy absorbing characteristics. The benefits of TPU were apparent under low-velocity impact (LVI) and split-Hopkinsons pressure bar (SHPB) tests, where the TPU produced much

higher plateau stress responses, which increased with higher impact energies.The competitiveness of TPU was further studied under low-velocity perforation tests, with a comparison against a widely used aluminium alloy 2024-T3 (AA 2034-T3). The results of which showed that TPU is capable of providing not only a progressive response, but also a higher energy absorption capability.

With the results obtained from the dynamic tests, TPU was the chosen material to act as the core for a sandwich panel, to be tested under blast loading conditions. AA 2024-T3 skins were used as facings to enhance the blast resistance of the sandwich structures. The experimental results highlighted an improvement in blast resistance following the addition of skins to the TPU core. An increase in the impulse loading resistance was observed, relative to the monolithic 5 mm TPU, with increasing core thicknesses of 5, 10 and 20 mm, where increases of 6.3, 15.4 and 59.5 % were achieved, respectively.

Finally, finite element (FE) models were developed using a commercially available software, i.e. ABAQUS and validated with the relevant experimental data. A crushable foam model was developed for the purposes of simulating the response of the TSPU specimens, with good correlation. An elasto-plastic constitutive model was used for the TPU, and strain-rate effects were introduced using the Cowper-Symonds power law. The AA 2024-T3 was modelled using the Johnson-Cook constitutive model. These were then used for the dynamic loading conditions, with validations under low-velocity perforation. Numerical simulations of the blast response of the TPU panels were conducted by converting the explosive loading regime applied to the panels, to a simplified pressure pulse loading. Good agreement was obtained between the numerical and experimental results for the mid-point back face deflections. A further study was carried out on the CFRP tube which was modelled using an in-built ABAQUS 2D Hashin criteria and a user defined modified 3D Hashin criteria, with more favourable results being apparent with the use of the user defined model.

Contents

Abstract **i**

Contents **vi**

List of Figures **xiv**

Declaration **xv**

Acknowledgements **xvi**

Publications **xvii**

Nomenclature **xviii**

List of Abbreviations **xxiii**

1 Introduction **1**

1.1 Overview 2

1.2 Background 2

1.3 Motivation and Contribution of this Research 8

1.4 Thesis Outline 9

2 Literature Review **12**

2.1 Crashworthiness 13

2.2 Blast Resistance 16

2.3 Sandwich Structures 22
2.4 Fibre-Metal Laminates (FML) 24
2.5 Core Materials 25
2.5.1 Metallic core 26
2.5.2 Honeycomb 27
2.5.3 Polymer cores 28
2.6 Syntactic Foams 34
2.7 Graded Structures 35
2.8 Reinforcement(s) 36
2.9 Numerical Modelling 41
2.9.1 Modelling polymers 43
2.9.2 Modelling composites 44
2.9.3 Modelling blast loading 48
2.10 Summary of Literature Review 54

3 Experimental Methodology 56
3.1 Manufacturing 57
3.2 Mechanical Testing 63
3.2.1 Quasi-static testing procedure 63
3.2.2 Dynamic testing 65
3.2.3 Blast tests 76
3.3 Summary of Experimental Methodology 82

4 Experimental Results and Discussion 83
4.1 Results and Discussion 84
4.1.1 Quasi-static compression results 84
4.1.2 Quasi-static tensile results 91
4.1.3 Low velocity impact (LVI) results 92
4.1.4 Split-Hopkinsons pressure bar (SHPB) results 99

4.1.5 Blast results . . . 102
4.2 Summary of Experimental Results . . . 107

5 Finite Element (FE) Modelling and Results 109
5.1 Time Integration . . . 110
5.1.1 Abaqus/Standard . . . 110
5.1.2 Abaqus/Explicit . . . 110
5.2 Constitutive Relationships . . . 110
5.2.1 Elasto-plastic . . . 111
5.2.2 Johnson-Cook . . . 115
5.2.3 Crushable foam . . . 116
5.2.4 Modified 3D Hashin's failure criteria . . . 120
5.3 Finite Element (FE) Modelling . . . 124
5.3.1 Quasi-static modelling . . . 124
5.4 Dynamic Modelling . . . 127
5.4.1 Low velocity perforation . . . 127
5.4.2 Blast modelling . . . 128
5.5 Finite Element Modelling Results and Discussion . . . 130
5.5.1 Quasi-static simulation results . . . 130
5.5.2 Dynamic simulation results . . . 136
5.6 Summary of Finite Element Modelling . . . 141

6 Conclusions and Recommendations for Future Work 142
6.1 General Summary . . . 143
6.2 Conclusions of Experimental and Numerical Work . . . 144
6.3 Recommendations for Future Work . . . 146

References 173

Appendices 174

A Mould design for the manufacturing of the TSPU **175**

B SHPB Matlab code for data processing **180**

List of Figures

Figure 1.1 Road accidents that resulted in fatalities in the United Kingdom, data from Ref. [7]. 3

Figure 1.2 Illustration of aircraft components exposed to the risk of bird strikes. [14] 5

Figure 1.3 Classification of composites. 6

Figure 2.1 Typical stress-strain characteristics experienced under uniaxial compression under quasi-static loading: 2.1a, stress-strain curve with strain-hardening characteristic; 2.1b, stress-strain curve with strain-softening characteristic; and 2.1c, stress-strain curve with perfectly plastic characteristics [42]. 16

Figure 2.2 Typical pressure-time history from a far-field explosion [46]. 17

Figure 2.3 Strain-rates associated with different types of loading [51]. 19

Figure 2.4 Typical ballistic pendulum [53]. 20

Figure 2.5 Diagram of a simplified shock tube. 21

Figure 2.6 Construction of a sandwich structure [57]. 22

Figure 2.7 Heirarchical description of cellular materials classification [100]. 26

Figure 2.8 Schematic representation of a segmented TPU copolymer morphology [114]. 31

Figure 2.9 Schematic representation of TPUs morphology [114]. . . . 32

Figure 2.10 Crushing characteristics of continuous fibre-reinforced composite tubes (a) fragmentation, (b) splaying, (c) brittle and (d) buckling [168]. 39
Figure 2.11 Double Chamfer Trigger (mm), where L_w is the weakened length [173]. 40
Figure 2.12 Length scales used in computational materials science. . . 42
Figure 2.13 Classification of composite crushing numerical models [191]. 48
Figure 2.14 Simplified pressure-time loading histories for rectangular and triangular pressure pulse loading 50

Figure 3.1 CFD simulation of the resin transfer process into the mould. 57
Figure 3.2 Variation of hollow glass microspheres (%, volume) and density (kg/m^3) of the syntactic TSPU. 58
Figure 3.3 (a) Example of the cross section of stepwise graded foam (TSPUG1), with density variation through-thickness and (b) optical micrograph of TSPUM3 illustrating the embedding of glass microspheres in the TSPU matrix. 59
Figure 3.4 Curing temperature history for TPU. 61
Figure 3.5 Various triggers used on the CFRP tubes. NC - No Trigger, ChI - 45° inner chamfer, ChO - 45° outer chamfer, T - Top, B - Bottom.. 62
Figure 3.6 One and four CFRP tube configurations used with the TPU and TSPU matrices. 62
Figure 3.7 Photographs of *INSTRON 4505* (a) and *INSTRON 5989* (b) universal testing machines 63
Figure 3.8 Geometry of tensile specimens (ASTM D638 - type V) . . 64
Figure 3.9 Tensile set-up with clip-on extensometer. 65

Figure 3.10 High speed camera (HSC) impact rig set up for unreinforced samples (a) and laser Doppler velocimeter (LDV) impact rig set up for tube reinforced samples (b). 66
Figure 3.11 Schematic arrangement of laser Doppler velocimeter (LDV) [214]. 67
Figure 3.12 Flowchart illustrating the steps of the filtering process for the LDV raw data. 69
Figure 3.13 Typical velocity-time raw data from LDV showing full raw data (a) and reduced data (b). 69
Figure 3.14 Schematic of the perforation test set-up. 71
Figure 3.15 Schematic of the compression SHPB test set-up. 72
Figure 3.16 Schematic of the SHPB experimental load process. 74
Figure 3.17 Waveform (a) and stress-strain (b) curve extraction process flowchart. 76
Figure 3.18 Photograph and schematic of the air-blast test arrangement. 78
Figure 3.19 Diagram of explosive stand-off distance (SOD) and assumed loading conditions, i.e. uniform or localised loading [219]. 78
Figure 3.20 Schematic of the ballistic pendulum. 79
Figure 3.21 Sine wave output from oscilliscope. 80

Figure 4.1 Energy absorbed and specific energy absorbed for TSPU (M0-M12). 84
Figure 4.2 Stress-strain curves for TSPU M0, M3, M7 and M12 under quasi-static loading. 85
Figure 4.3 Photographs of the collapse mechanisms of M0 (a,b), M12 (c,d) and G1 (e,f) under quasi-static loading. 86
Figure 4.4 Quasi-static response of CFRP tubes with various chamfers. 86

Figure 4.5 Quasi-static stress vs. strain curves for (a) 1 CFRP tube reinforced TSPUM0, M3, M7 and M12, (b) 4 CFRP tube reinforced TSPUM0, M3, M7 and M12 and (c) unreinforced and reinforced 1 and 4 tube TPU. 88
Figure 4.6 SEA and plateau stresses at 25 and 50% for the unreinforced (a) and reinforced (b) syntactic TSPU under quasi-static loading. 89
Figure 4.7 Ashby plot comparing the specific compressive properties of the unreinforced/reinforced non-syntactic TSPU M0 and syntactic TSPU. Material data from Ref. [104]. 90
Figure 4.8 Stress-strain curves at three different orientations of 0°, 45° and 90°. 91
Figure 4.9 Nominal stress-strain curves for TPU (a) and failure strain (b) for increased strain-rates. 92
Figure 4.10 Quasi-static vs. dynamic stress-strain curves for (a) M0 and M12, (b) G1 and G2. 93
Figure 4.11 SEA and plateau stresses at 25 and 50% for the unreinforced TSPU M0, M12, G1 and G2 under dynamic loading 94
Figure 4.12 Stress vs. strain (a) and SEA vs. strain-rates (b) for TPU under dynamic loading. 95
Figure 4.13 Stress vs. strain traces for (a) reinforced TPUT1, TSPUM0T1, M3T1, M7T1 and (b) reinforced G2 with and without chamfered tubes. 96
Figure 4.14 SEA and plateau stresses at 25 and 50 % strain for the reinforced foams under dynamic loading. 96
Figure 4.15 Typical failure of reinforced (4.15a) TSPUM0 and (4.15b) TPU samples under dynamic compressive loading. 97
Figure 4.16 Quasi-static and dynamic perforation response of TPU and 2024-T3. 98

Figure 4.17 True stress vs. true strain for TPU at various strain-rates. 99
Figure 4.18 Failure of TPU observed at strain-rates (a) 7170 and (b) 8316 s^{-1}. 100
Figure 4.19 True stress vs. true strain for TSPUM0, M3, M7 and M12 at various strain-rates. 101
Figure 4.20 Plot of strain-rate sensitivity ($\sum$) versus strain-rate for samples TSPU M0, M3, M7 and M12. 102
Figure 4.21 Back face tearing failure of AA/TPU/AA (C3). 105
Figure 4.22 Partial tearing failure of TPU (A5) without skins. 105
Figure 4.23 Localised failure of CFRP tubes for sample E1 (22.24 Ns). 106

Figure 5.1 Initial yield surface (a) CIH (b) CVH [183]. 117
Figure 5.2 Compression model used for the TSPU and TPU validation in ABAQUS. 125
Figure 5.3 Compression model used for the graded TSPU in ABAQUS. 125
Figure 5.4 Tensile model used for TPU validation in ABAQUS. 126
Figure 5.5 Loading and boundary conditions adopted in the finite element tube model. 127
Figure 5.6 Geometry, mesh, boundary and loading conditions of the TPU perforation sample. 128
Figure 5.7 Dimensions, loading, boundary conditions and mesh generation of quarter model sandwich panel. 129
Figure 5.8 Toplogy of an eroding contact surface. 129
Figure 5.9 Stress vs. strain comparsion of the experimental and numerical of the TSPU M0, M3, M7, M12, G1 and G2 specimens. . 131
Figure 5.10 Experimental and numerical response of TSPUG1 under quasi-static loads at 25 and 50% strain (ϵ). 132
Figure 5.11 Experimental (Exp) vs. numerical (Sim) blast response. . . 134

Figure 5.12 Experimental (Exp) vs. numerical (Sim) blast response. . . 134
Figure 5.13 Load-displacement traces for experimental and numerical quasi-static compresion of CFRP tube, with comparisons between using the VUMAT subroutine and 2-D Hashin criteria. 135
Figure 5.14 Experiment and numerical comparison of load vs. displacement for compression (a) and tensile models (b). 136
Figure 5.15 Back face view of the penetrated TPU panel (a) experimental (b) numerical. 137
Figure 5.16 Back face view of the penetrated AA 2024-T3 panel (a) experimental (b) numerical. 137
Figure 5.17 Back face view of the penetrated AA 2024-T3 panel (a) experimental (b) numerical. 138
Figure 5.18 Load-displacement traces for experimental and numerical perforation of AA 2024-T3. 138
Figure 5.19 Experimental (Exp) vs. numerical (Sim) blast response. . . 139
Figure 5.20 Experimental (Exp) vs. numerical (Sim) blast response. . . 139
Figure 5.21 Numerical blast response of the back face tearing failure of specimen C3 (18.44 Ns) 140

Figure A.1 Dimension of top plate (mm). 176
Figure A.2 Dimension of sections 1 and 2 (mm). 177
Figure A.3 Dimension of section 3 and 4 (mm). 178
Figure A.4 Dimension of the bottom plate (mm). 179

List of Tables

Table 1.1 Categories of various impacts [8] 4

Table 2.1 Specific energy absorption (SEA) comparison of various core materials. 25

Table 3.1 Physical properties of thermoset polyurethane [211]. 59

Table 3.2 Technical specifications of micro-spheres (K-series) [211]. . . 59

Table 3.3 Density variation through the thickness of the graded TSPU specimens G1 and G2. 60

Table 3.4 General setting of the Burst Spectrum Analyser (BSA). . . 68

Table 3.5 Properties of PE4. 77

Table 3.6 Description of blast test specimens. 77

Table 4.1 CFRP tubes under quasi-static compression with with various chamfers providing yield stress (σ_y) and specific energy absorption (E_s). 87

Table 4.2 Total energy absorbed, E_T, for TPU and AA 2024-T3 under quasi-static and dynamic perforation. 98

Table 4.3 Charge mass and diameter, impulse, failure and back face deflection for the specimens. T - full tearing and PT - partial tearing around the boundary 103

Table 4.4 Comparison of various specimens subject to uniform blast loading with comparisons made against areal density (kg/m^2), approximate material cost (GBP/kg), SOD (mm) and resistance to impulse (Ns) prior to failure. 104

Table 5.1 Material properties and parameters for TPU used in the finite element modelling. 114

Table 5.2 Isotropic hardening data for TPU. 115

Table 5.3 Johnson-Cook parameters and the assumed elastic properties for AA 2024-T3 [226]. 115

Table 5.4 Damage constants for the AA 2024-T3 [226]. 116

Table 5.5 Material properties for the crushable foam model (TSPUM0, M3, M7 and M12). 120

Table 5.6 Summary of elasticity properties and the damage initiation data for the CFRP [229]. 123

Table 5.7 Comparison of experimental and simulation results for the syntactic TSPU specimens (M0, M3, M7, M12, G1 and G2). . . . 133

Declaration

This thesis submitted for the degree of Doctor in Philosophy (Ph.D.) in the faculty of Engineering at the University of Liverpool. The research project reported herein was carried out, unless otherwise stated, by the author, in the School of Engineering between 2013-2016.

I confirm that this thesis is my own work, that I have not plagarised the work of other researchers, and that full and appropriate acknowledgment has been given with references.

Acknowledgements

The support of my supervisors, Dr Zhongwei Guan and Professor Wesley J. Cantwell, is greatly appreciated, their helpful support and desire to achieve perfection in all aspects of my research was crucial to the success of this Ph.D. thesis. The financial support by the School of Engineering of Liverpool University is also gratefully acknowledged.

The support of collaborating universities is acknowledged and appreciated. The University of Manchester for allowing use of their testing facilities (600 kN Instron *5989*). The University of Cape Town, South Africa for allowing use of their ballistic pendulum. The Nanjing University of Science and Technology, PR China for allowing use of their split-Hopkinson Pressure Bar (SHPB). Also, Covestro for providing the Desmopan DP 9852 TPU pellets used in this research.

My sincere gratitude extends to all the staff at the Department of Engineering, especially Dr Robert Birch for his valuable advice and guidance. Additionally, I would like to extend my appreciations to many of my colleagues who I had the privilege to work alongside in the School of Engineering.

Last but not least, a huge debt of gratitude is extended to my family, who have patiently endured my Ph.D. journey and offered their support through difficult times.

Publications

- A. Jamil, Z. W. Guan and W. J. Cantwell, The static and dynamic response of CFRP tube reinforced polyurethane, Composite Structures, 161, pp. 85-92 (2017). DOI: 10.1016/j.compstruct.2016.11.043

- A. Jamil, Z. W. Guan, W. J. Cantwell, X. F. Zhang and G. S. Langdon, Blast response of aluminium/thermoplastic polyurethane sandwich panels - experimental work and numerical analysis (Submitted).

Nomenclature

a	Acceleration (m/s^2)
A	Area (m^2)
A_0	Initial cross-sectional area (m^2)
A_B	Cross-sectional area of the bar (m^2)
A_D	Decay coefficient
A_s	Cross-sectional area of the specimen (m^2)
β	Weight factor
c	Speed of light (m/s)
C_0	Wave velocity (m/s)
C_d	Damage elastic matrix
c_p and c_v	Specific heat under constant pressure and volume, respectively (J/K)
d_f, d_m and d_s	Current state of fibre, matrix and shear damage, respectively
D	Damage variable
D^{el}	Fourth order elasticity tensor
D_s	Distance to the charge (mm)
D_h	Overall damage variable
E	Energy (Joules, J)
E_m	Internal specific energy per unit mass (J/kg)
E_s	Specific Energy Absorption (kJ/kg)
E_T	Total Energy Absorption (J)
E_Y	Young's Modulus (N/m^2)
E_{Y1} and E_{Y2}	Longitudinal and transverse moduli, respectively (N/m^2)

E_{Yz}, E_{Yr} and $E_{Y\theta}$	Young's moduli in the z, r and θ directions, respectively (N/m^2)
ϵ	Strain tensor
ϵ_{11}, ϵ_{22}, ϵ_{33}	Principal strains
ϵ_d	Densification strain
ϵ^{el}	Elastic strain
ϵ_f	Equivalent strain to fracture
ϵ_I, ϵ_R and ϵ_T	Incident, reflected and transmitted strain, respectively
ϵ_m	Mean strain
$\dot{\epsilon}_m$	Mean strain-rate (s^{-1})
$\epsilon_{Nominal}$	Nominal strain
ϵ^{pl}	Plastic strain
ϵ_{True}	True strain
ϵ_y	Yield strain
η	Stress triaxiality (N/m^2)
F	Force (N)
f_{GM}	Volume fraction of microspheres
G	Shear modulus (N/m^2)
G_{ij}	Shear modulus in the i-j plane (N/m^2)
γ	Heat capacity ratio
I_m	Measured impulse (Ns)
L_S	Specimen length (mm)
μ	Viscosity (Ns/m^2)
M	Mass of pendulum (kg)
m	mass (g)
ν	Poisson ratio
ν_{ij}	Poisson's ratio for the transverse strain in the j-direction
ν_{12}	In-plane Poisson's ratio
ν_{23}, ν_{23}	Interlaminar Poisson's ratio

ν_{pl}	Plastic Poisson's ratio
ω_D	State variable
ω_d	Actual frequency
ω_n	Natural frequency
p	Pressure stress (N/m^2)
p_c	Positive hydrostatic compressive yield stress (N/m^2)
p_t	Negative hydrostatic tension yield stress (N/m^2)
P_1 and P_2	Surface loads (N)
$P(t)$	Pressure at time t (N/m^2)
P_{SO}	Peak overpressure (N/m^2)
P_{SO}^-	Maximum negative pressure (N/m^2)
ϕ	Diameter (mm)
R_0	Radius (mm)
ρ	Density (kg/m^3)
ρ_0	Original density (kg/m^3)
ρ_s	Density of solid phase (kg/m^3)
ρ_{GM}	Density of glass microspheres (kg/m^3)
ρ_{PU}	Density of polyurethane resin (kg/m^3)
σ	Stress tensor (N/m^2)
σ_{11}, σ_{22}, σ_{33}	Principal stresses (N/m^2)
σ_c^0	Uni-axial compression yield stress (N/m^2)
σ_m	Mean stress (N/m^2)
$\sigma_{Nominal}$	Nominal stress (N/m^2)
σ_{True}	True stress (N/m^2)
σ_v	von Mises equivalent stress (N/m^2)
σ_y	Yield stress (N/m^2)
$\sum$	Sensitivity parameter
S_{ij}	Second invariant stress deviator tensor

S_L	Longitudinal shear strength (N/m^2)
S_T	Transverse shear strength (N/m^2)
t	Time (s)
τ	Blast load duration (s)
t_A	Arrival time of shock wave (s)
t_O	Positive phase duration (s)
t_0^-	Duration of the negative phase (s)
T	Natural period of pendulum
T_{abs}	Absolute temperature (K)
u	Kinematic viscosity of the fluid ($m^2\,s^{-1}$)
U_1	Contact face of incident bar
U_2	Contact face of transmission bar
V	Volume (m^3)
V_{SF}	Measured volume of syntactic foam (m^3)
W	Charge mass (g)
W_{SF}	Measured weight of syntactic foam (g)
X_C	Compressive strength in longitudinal direction (N/m^2)
X_T	Tensile strength in longitudinal direction (N/m^2)
X_1	Maximum forward displacement of pendulum
X_2	Maximum backward displacement of pendulum
$\dot{X}_0$	Initial velocity of pendulum (m/s)
$\ddot{X}_0$	Acceleration of pendulum ($m\,s^{-2}$)
Y_C	Compressive strength in transverse direction (N/m^2)
Y_T	Tensile strength in transverse direction (N/m^2)
Z	Scaled distance

List of Abbreviations

1D, 2D and 3D	One, Two and Three Dimensional, respectively
AA	Aluminium Alloy
ALE	Arbitrary Lagrangian Eulerian
ARALL	Aramid Reinforced Aluminum Laminates
BSA	Burst Spectrum Anayser
CDM	Continuum Damage Mechanics
CF	Carbon Fibre
CFRP	Carbon Fibre Reinforced Polymer
CIH	Crushable Foam with Isotropic Hardening
CONWEP	Conventional Weapons Effects Program
CVH	Crushable Foam with Volumetric Hardening
DAS	Data Acquisition Station
DfT	Department for Transport
EoS	Equation of State
FAA	Federal Aviation Administration
FE	Finite Element
FGF	Functionally Graded Foam
FM	Fracture Mechanics
FML	Fibre-metal Laminate
FRCS	Fibre Reinforced Composite Structures
FRP	Fibre Reinforced Plastics
FSI	Fluid Structure Interaction
GAMBIT	Generalised Acceleration Model for Brain Injury Threshold

GF	Glass Fibre
GFPP	Glass Fibre Reinforced Polypropylene
GLARE	Glass Laminate Aluminium Reinforced Epoxy
HFC	Hashin Failure Criterion
HGM	Hollow Glass Microspheres
HIC	Head Injury Criteria
HIP	Head Injury Power
HS	Hard Segment
HSC	High Speed Camera
JWL	Jones-Wilkins-Lee
LDS	Laser Displacement Sensor
LDV	Laser Doppler Velocimeter
LVI	Low Velocity Impact
MPDM	Material Property/Stiffness Degradation Method
MR	Magnetorheological
PAS	Polyarysulfone
PE4	Plastic Explosive No. 4
PEEK	Polyether-ether-ketone
PEI	Polyether-imide
PI	Polyimide
PMI	PolyMethacrylImide
PP	Polypropylene
PS	Polystyrene
PSF	Polymer Matrix Syntactic Foam
PTFE	Polytetrafluoroethylene
PU	Polyurethane
PUF	Polyurethane Foam
PVC	Polyvinyl Chloride

RDX	Nitramide
R.E.	Relative Effectiveness Factor
Re	Reynolds Number
SEA	Specific Energy Absorption
SHPB	Split-Hopkinsons Pressure Bar
SOD	Stand-off Distance
SS	Soft Segment
TEA	Total Energy Absorption
TNT	Trinitrotoluene
TPU	Thermoplastic Polyurethane
TSPU	Thermoset Polyurethane
UD	Uni-directional
UMAT	User Material
VARTM	Vacuum Assisted Resin Transfer Method
VF	Volume Fraction
VUMAT	Vectorised User Material
WHO	World Health Organisation

Chapter 1

Introduction

This chapter provides a brief introduction to composite materials for energy absorption along with their applications. The rationale behind the use of efficient energy-absorbing structures will be presented. Additionally, the motivation, the aim, objectives and significance of the study are discussed.

1.1 Overview

Sandwich structures are becoming increasingly popular due to their energy absorbing capability. Tube-reinforced core structures are a material system whereby a metallic, polymeric or composite tubes are inserted into a core with the aim of increasing the energy-absorbing capacity of the cores without compromising on the weight. Syntactic foams are a new classification of material, more specifically these are composite materials that incorporate porous, hollow or solid particles within a metallic or polymer matrix. Additionally, functionally-graded foams (FGFs) have been presented as an excellent means of introducing progressive energy absorption by varying the foam density in a predefined manner.

The polyurethane (PU) industry is a rapidly expanding business that currently produces some 12 million metric tons of PU raw material annually, with revenues forecast to reach $US 74 billion by the year 2022 [1]. Polyurethane has been classed as one of the most versatile materials [2]. As a result of the wide variety of polyols and isocyanates that are available as raw materials, the structure of the polymer can be modified in order to satisfy specific design requirements for a given application. Subsequently, these polymers have been widely used in applications as diverse as biomaterials for implants [3] as well as in electronic and technological applications [4, 5].

1.2 Background

History presents evidence of the risk and repercussions of impacts and explosions to both structural integrity and consequently human life. Due to this, a great deal of interest has been expended by the engineering community as well as government agencies to improve impact and shock resistance of engineering structures. A prime example of catastrophic failures in aerospace structures due to damage caused by impacts can be seen with the Columbia space shuttle, which

demonstrated the need for proactive efforts by the research community on impact resistant materials.

According to the Department for Transport (DfT), in the year 2013, it was reported that there were 1,713 fatalities in the United Kingdom due to road traffic accidents, Figure 1.1. Although, this figure is approximately 50 % lower than that of the year 2000, there is a requirement to lower if not eradicate the number of fatalities. On a wider scope, according to the World Health Organisation (WHO), road traffic injuries caused an estimated 1.25 million deaths worldwide in the year 2013. That is, one person dies every 25 seconds due to road traffic accidents [6]. Preservation of life is of upmost importance and can be achieved by the introduction of a barrier between life and death. One of the challenges, which are present in avoiding serious injury or fatalities, is to strategically employ materials that disperse the levels of energies experienced in a crash, in a more controlled and progressive manner.

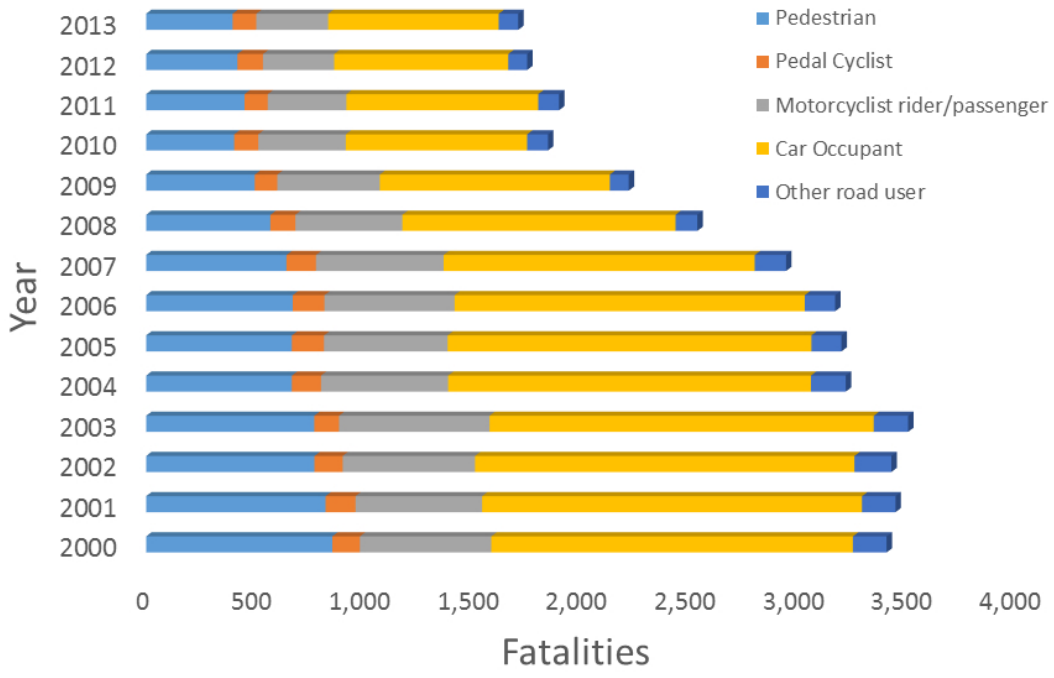

Figure 1.1: Road accidents that resulted in fatalities in the United Kingdom, data from Ref. [7].

Generically speaking, an impact consists of various velocities as illustrated in Table 1.1. High-velocity impact response is dominated by stress wave propagation through the thickness of the material, which means that the structure does not have time to respond, resulting in localised damage. Boundary condition effects can be ignored since the impact event passes before the stress waves reach the boundary [8]. Foreign object damage, blast loading, structural impacts and terminal ballistics are usually associated with high strain-rate loading of composite materials. Under impact, composite materials experience significant strain, which is dependent upon the severity of the impact, temperature range and strain-rate. Therefore, it is important to categorise the strain-rates and temperatures of the intended application [8]. When impact velocities are below 5 m/s, the response type is controlled by the impactor/plate mass ratio rather than impact velocity [8, 9]. The dynamic structural response of a target, during low velocity impact (LVI), is important since the contact duration is long enough for the entire structure to respond to the impact and consequently more energy is absorbed elastically [8].

Table 1.1: Categories of various impacts [8]

Categories	Speed	Examples
Low velocity impact	< 10 m/s	Tool drops
Intermediate velocity	10 m/s - 50 m/s	Foreign object debris, secondary blast debris or tornado/hurricane debris
High velocity/ballistic	50 m/s - 1000 m/s	Small arms fire or explosive warhead fragments
Hyper velocity	> 2 km/s	Micrometeorites

The Federal Aviation Administration (FAA) [10] reported that during the years from 1990 to 2013, over 243 commercial aircraft were destroyed as a result of approximately 90,000 bird strikes [11]. Heimbs [12, 13] reported the potential hazards of commercial aircraft which may be susceptible to exterior or interior uncontained impact of an aircraft, such as turbine engine failure, i.e. the blade

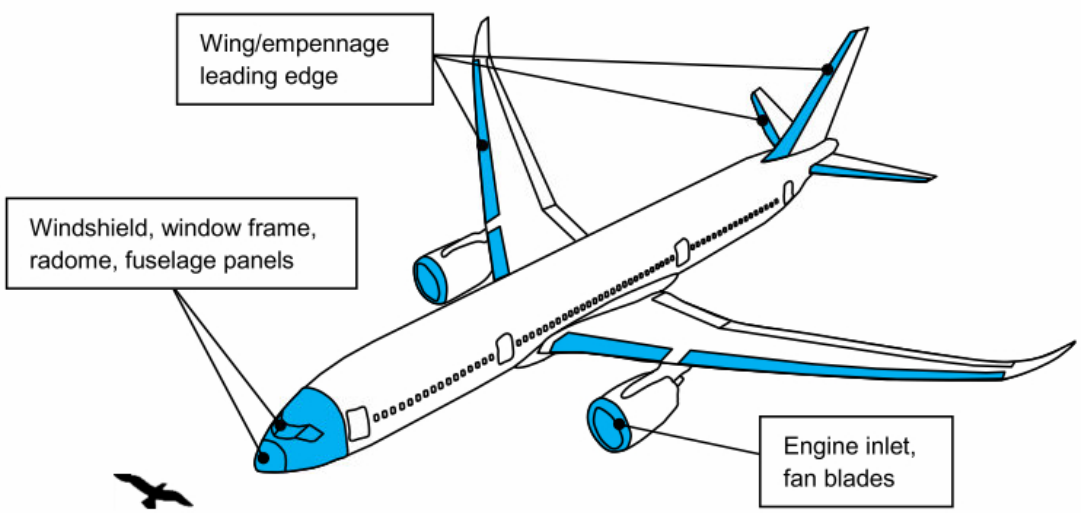

Figure 1.2: Illustration of aircraft components exposed to the risk of bird strikes. [14]

from the engine fan, rim release of a wheel rim fragment and tire rubber impact in the case of wheel rupture. In addition to bird strikes, exterior impacts may occur from runway debris, stones, hail or ice. Figure 1.2, illustrates the areas of which exterior impacts are most likely to occur in particular with bird strikes, such as the fuselage panels, windshield, radome, wing/empennage leading edge or engine inlet and fan blades.

Blasts are an event where a considerable amount of energy is released in a relatively short time period. Explosions may have many causes, such as the ignition of a gas in a processing plant, the rapid depressurisation of a pressure vessel [15, 16] in an aircraft that may have a breach its structural integrity [17] or the detonation of explosives [18]. Although accidental explosions, i.e. mechanical failure of pressurised structures may be prevented through diligent design and maintenance, explosions are usually associated with deliberate actions, i.e. military or terrorist activity. According to the US State Department figures [19] in 2015, on average, there were 981 terrorist attacks worldwide, resulting in 28,328 fatalities. With the continuing threat in terrorist activities, both nationally and internationally, attention is focusing on the need to design and construct lightweight structures

offering increased protection to both civil and military personnel.

Composite materials offer excellent strength and stiffness properties when compared to more conventional materials. Composite materials are being widely used due to their energy absorbing capacities under both impact and blast loading and can be classified in many forms as shown in Figure 1.3. The application of composites in both the automotive and aerospace industry provides an efficient way to reduce weight without compromising structural integrity, and in some cases to enhance structural integrity. Needless to say, the reduction of weight offers substantial fuel savings for the land transport and aerospace industries.

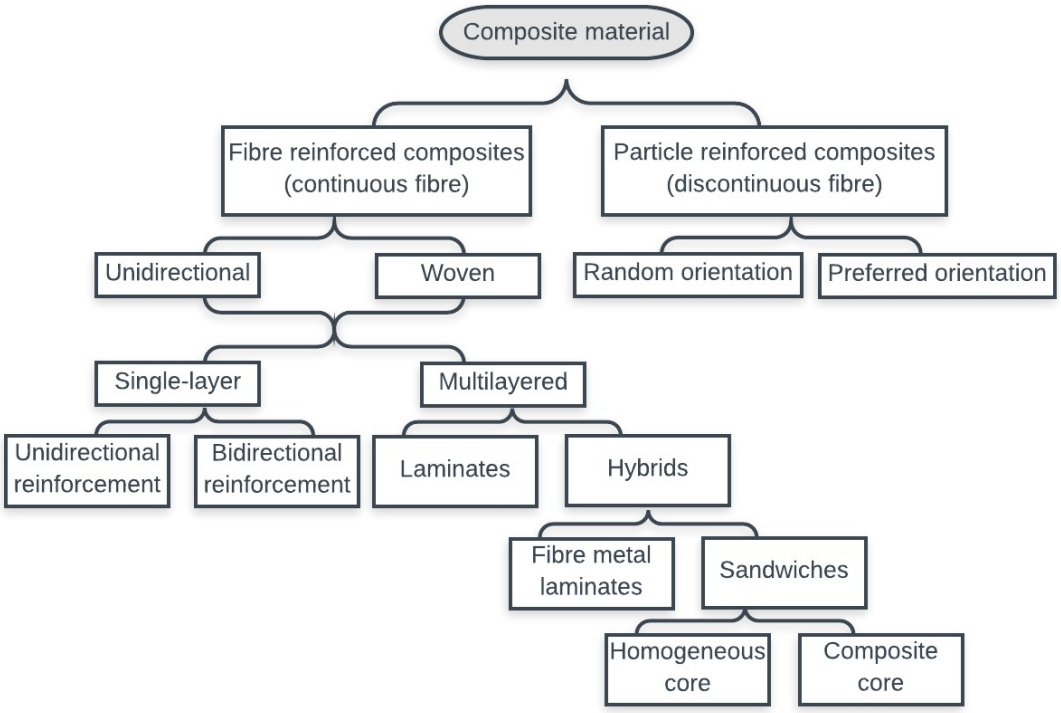

Figure 1.3: Classification of composites.

Sandwich structures are popular, due to their excellent specific properties. The concept of sandwich construction can be traced back to the middle of the 19th century [20], however it is thought that the principles of sandwich construction may have been applied much earlier. The inclusion of the sandwich concept began to generate momentum during the start of World War II, where sandwich panels

were exploited for their weight to stiffness ratios, high structural efficiency and durability. They have since been widely used in the aerospace, shipbuilding, and construction industries.

Sandwich structures are known as efficient energy absorption systems due to their high strength/weight ratio and high stiffness/weight ratio. The core of a sandwich structure bears the shear loads, whereas the skins, i.e. outer face plates, increase the stiffness and subsequently carry the bending forces [21]. Much research has been carried out to develop structures that are able to withstand loads from conventional explosives. Fundamentally, the properties of sandwich structures assist in dispersing the mechanical impulse that is transmitted into the structure. Generally, these structures consist of a lightweight core with two external face layers. The core material can be divided into several categories such as honeycomb [21], foam [22–25], textile, functional [26] and truss cores [27].

Syntactic foams are a type of composite material that are synthesised by filling a matrix, i.e. polymer, ceramic or metallic with hollow particles (microbaloons or microspheres). These types of composite materials generally enable higher energy absorption properties, primarily due to a prolonged plateau region and subsequently the densification strain (ϵ_d), providing higher specific energy absorption, i.e. energy absorption per unit mass (J/kg). This is due to the mechanisms of the cells walls of syntactic foams experiencing a continuous plastic collapse at a critical value known as the "plateau stress", until the material reaches the densification strain.

Polymers have gained popularity as energy absorbers, due to their low cost, ease of production, corrosion resistance and relatively low density. The characteristics of polymers have been exploited from low velocity impact to higher strain-rate loading as a basis for applications in blast and impact damage mitigation [28]. They are increasingly being implemented as energy absorbers [29], due to their ability to absorb impact energy in a controlled manner, and are apprecia-

ble to various applications from automobiles to aircrafts [30–33]. Some commonly used polymers are Polyvinyl Chloride (PVC), Polystyrene (PS), Polyether-imide (PEI) and Polyurethane (PU). Polymers can be classified into two types, i.e. thermosets and thermoplastics, both of which are long chain molecules however, they differ in their bonding. Thermosetting plastics are held together by strong covalent bonds, whilst in thermoplastics the long chain molecules are held together by weak van der Waals forces:

- Thermosetting resin is a petrochemical material that cures via a cross-linking procedure known as a curing process. This is an irreversible process and can be done at room temperature or the resin can be heated at various temperatures. Thermosetting materials have a three-dimensional network of covalent bonds. These bonds cannot be easily broken by heating and, therefore, cannot be remelted and formed as easily as thermoplastics. The cross-linking procedure forms a molecule with a larger molecular weight, resulting in a higher melting point. Also in this process, the molecular weight would increase so that the melting point is higher than the surrounding ambient temperature, resulting in the formation of a solid material.

- Conversely, thermoplastics are not characterised by the cross-linking network. Heat can be used to break the van der Waal forces between the molecules and change the form of the material from a solid to a liquid. Unlike thermosetting polymer, thermoplastics can be remoulded due to the intermolecular interactions that increase upon cooling and restore the bulk properties.

1.3 Motivation and Contribution of this Research

Due to the continuing threat of both impact and explosions to the structural integrity of transport vehicles and consequently to human safety, there is a con-

tinuing drive to develop composite materials that provide high strength-to-weight in order to contribute to the development of high-speed and energy-efficient transport systems. The issue of climate control provides the need to develop lightweight composite structures to replace some existing metallic ones in the transportation sector. This research makes a comparison of two types of polyurethane cores, i.e. thermosetting and thermoplastic, under quasi-static and dynamic loading.

Further investigations are carried out in reinforcing the cores with carbon fibre reinforced polymer (CFRP) tubes, which are lightweight yet provide higher energy absorption properties in comparison to traditional materials such as metallic structures. Comparisons are made between using a thermoplastic polyurethane (TPU) and a thermosetting PU (TSPU) core, with modifications made to the TSPU core by developing a syntactic material with the use of glass microspheres and further modifications to develop a novel graded structure to improve the dynamic response of the cores. Split-Hopkinsons pressure bar (SHPB) tests are carried out at Nanjing University of Science and Technology, PR China (PRC), to characterise these materials at high strain-rates. From these results a material was then selected to act as the core material of a sandwich panel in order to carry out blast tests at the University of Cape Town, South Africa.

1.4 Thesis Outline

The format of this thesis combines both an experimental and a numerical study with the aim of investigating quasi-static and dynamic performance of a polymeric core, namely polyurethane. Two sets of polyurethane are investigated, i.e. thermoset and thermoplastic. The aim was to develop a structure which can provide progressive energy absorbing characteristics for use under impact loading conditions. Both materials will be subject to quasi-static, LVI and SHPB tests. Subsequently, a material will be selected which can help mitigate blast loading on

structures. Finally, finite element (FE) models are developed with comparisons made with experimental work. The outline of the thesis is given below:

- Chapter 1 (Introduction) - provides a brief introduction to composite materials for energy absorption along with their applications. The rationale behind the use of efficient energy-absorbing structures will be presented. Additionally, the motivation and objectives of the research and significance of the study are discussed.

- Chapter 2 (Literature Review) - provides an overview of the current literature with a focus on polymers, reinforcements and applications under quasi-static and dynamic loading. Further review covers numerical modelling of structural response of the relevant composites subject to various loading regimes i.e. quasi-static, dynamic and blast modelling.

- Chapter 3 (Experimental Methodology) - presents the details of the manufacturing of the specimens and the experiments conducted during the course of this research study. A variety of mechanical testing and experimental techniques are used to investigate the quasi-static and dynamic characteristics of graded and ungraded TSPU syntactic foam as well as TPU samples. The first section of this chapter explains in detail, the manufacturing steps of processing the syntactic TSPU foams (graded/ungraded) and the TPU. The experiments cover quasi-static, dynamic compression and perforation, and blast tests.

- Chapter 4 (Experimental Results and Discussion) - presents the experimental results obtained and a discussion. Firstly, the mechanical response of the syntactic TSPU and the TPU under quasi-static loading conditions will be presented, with further observation made for reinforcing these materials with CFRP tubes. Secondly, the dynamic response of the aforementioned

materials (unreinforced/reinforced) under low velocity impact (LVI) will also be presented. Further results are presented on the syntatic TSPU and TPU under high strain-rate loading conditions with the use of a split-Hopkinson pressure bar (SHPB). Finally, the blast response of the TPU in a sandwich structure configuration with the TPU as the core and AA 2024-T3 skins is also investigated and discussed.

- Chapter 5 (Finite Element (FE) Modelling and Results) - presents the development of the numerical modelling of the materials investigated using the finite element method to simulate the response of the materials/structures subjected to various loading conditions. Finally, the results of the finite element simulations and validation against the experimental data obtained in Chapter 3 are presented, reproducing various responses of quasi-static and dynamic loading.

- Chapter 6 (Conclusions and Recommendations for Future Work) - presents conclusions of this study, summarising the overall findings. In addition to this recommendations for future work to be carried out based on the current study are given.

Chapter 2

Literature Review

This chapter provides an overview of the current literature with a focus on polymers, reinforcements and applications under quasi-static and dynamic loading. Further review covers some of the numerical modeling aspects of relevant applications, i.e. quasi-static, dynamic and blast modelling.

2.1 Crashworthiness

"Crashworthiness" is defined as the degree of which a vehicle is able to absorb impact energy whilst protecting the occupant(s) [34]. Therefore, the primary concern of crashworthiness is focused on the absorption of impact energy through a controlled failure mechanism and modes that enable a progressive decay in the load profile during absorption. The key challenge for the design of crashworthy structures is to establish a controlled dissipation of the energy, avoiding rapid decelerations (inertial effects), to protect passengers from serious internal injury, i.e. brain damage. The assessment of the crashworthiness of a structure can be determined via a series of tests and numerical studies [35]. Fundamentally, tests are carried out to determine the energy absorption capacity of a structure.

The law of conservation of energy states that "The total energy of an isolated system remains constant and is said to be conserved over time. Energy can neither be created nor destroyed; rather, it transforms from one form to another" [36]. This transfer of energy is regarded as work done. In impact circumstances, the force acted upon a body or systems is regarded as the work done, i.e. W_{crush}. The product of the force, i.e. F_{crush}, exerted and the distance travelled, i.e. L_{crush}, is equal to the energy transmitted to a system and can be defined as,

$$W_{crush} = F_{crush} \cdot L_{crush} \tag{2.1}$$

An ideal energy absorber is defined as,

$$E_{crush} = W_{crush} = m \cdot a \cdot L_{crush} \tag{2.2}$$

where, m is the mass of the body and a is the acceleration .

An ideal energy-absorption system transforms all of the work input into work output. The efficiency of an energy absorbing system takes into account the ratio

of the work output (W_{crush}) and work input (E_{crush}) as defined by the following equation,

$$Efficiency = \frac{W_{crush}}{E_{crush}} \tag{2.3}$$

The energy absorption capability of a component can usually be analysed by conducting a compression test [37], where quasi-static testing is commonly carried out in order to characterise the performance of a particular energy-absorbing structure. These tests are usually straightforward in comparison to dynamic testing and provide researchers with some indication of the failure mechanisms involved. Routinely, specimens are compressed to about 80 % of their original thickness [38]. Cellular materials differ from solid materials in terms of their mechanical properties, due to differences in their microstructures [39]. The stress-strain curves can be used to characterise the Young's modulus (linear elasticity) of a material, the plateau strength (plastic yielding) and densification strain. In order to achieve higher levels of energy absorption, one should aim for a crushing mechanism that can be controlled to enable reinforcement to fail in a stable and progressive manner [40, 41], particularly for dynamic loading.

Quasi-static tests are carried out under a constant load which is time dependent yet slow enough to ensure inertial effect contributions to the system are negligible. The primary aim of these tests is to gather data about the materials behaviour under loading, and usually used to predict the materials behaviour under various loading conditions. The compressive stress-strain curve output from such tests can often be simplified into three regimes, namely, the linear elastic regime, the plateau regime, and the densification regime [37]. These three regimes are shown in Figures 2.1a, 2.1b and 2.1c for cellular solids characterised with different types of stress-strain curves. For many types of cellular solids, the plateau regime starts from the compressive yield strain, ϵ_y or compressive yield stress,

σ_y, representing the initiation of the new deformation mechanism of the cell wall or the cell wall failure, and ends at a critical strain, ϵ_d, representing the onset of densification, i.e. the point at which the material cannot be compacted any further, and can be expressed as a function of the relative density as,

$$\epsilon = f\left(\frac{\rho_0}{\rho_s}\right) \tag{2.4}$$

where ρ_0 is the original density of the cellular solid, and ρ_s is the density of the solid phase (cell wall material) of the cellular solid. For $\epsilon \geq \epsilon_d$, the compressive properties of a cellular solid are dominated by the compressive properties of the cell wall material.

The relative density of a cellular solid is dependent on the the geometry and arrangement of the cells. For various cell geometries and their relative densities can be found in [37]. Based on experimental results, a linear function to determine the densification strain for both elastic and plastic foams is recommended [37,42] as,

$$\epsilon_d = 1 - \alpha\left(\frac{\rho_0}{\rho_s}\right) \tag{2.5}$$

where α varies between 1.4 and 2.0 [43].

A number of experimental methods can be implemented in order to evaluate the impact response of materials. Traditional falling darts, Charpy tests, Izod and Gardner tests are only suitable for ranking polymers in terms of their impact performance due to the fact that they only impose inhomogeneous stress-strain fields and variable strain-rates. A series of physical phenomena takes place upon impact such as elastic, shock, and plastic wave propagation as well as fracture, fragmentation, perforation or spallation [44]. The drop-weight impact test method, where a weight of a specified mass is guided by rails and free falls from a height to strike the specimen, has been used to study the dynamic response of

structures and material behaviour at different energies.

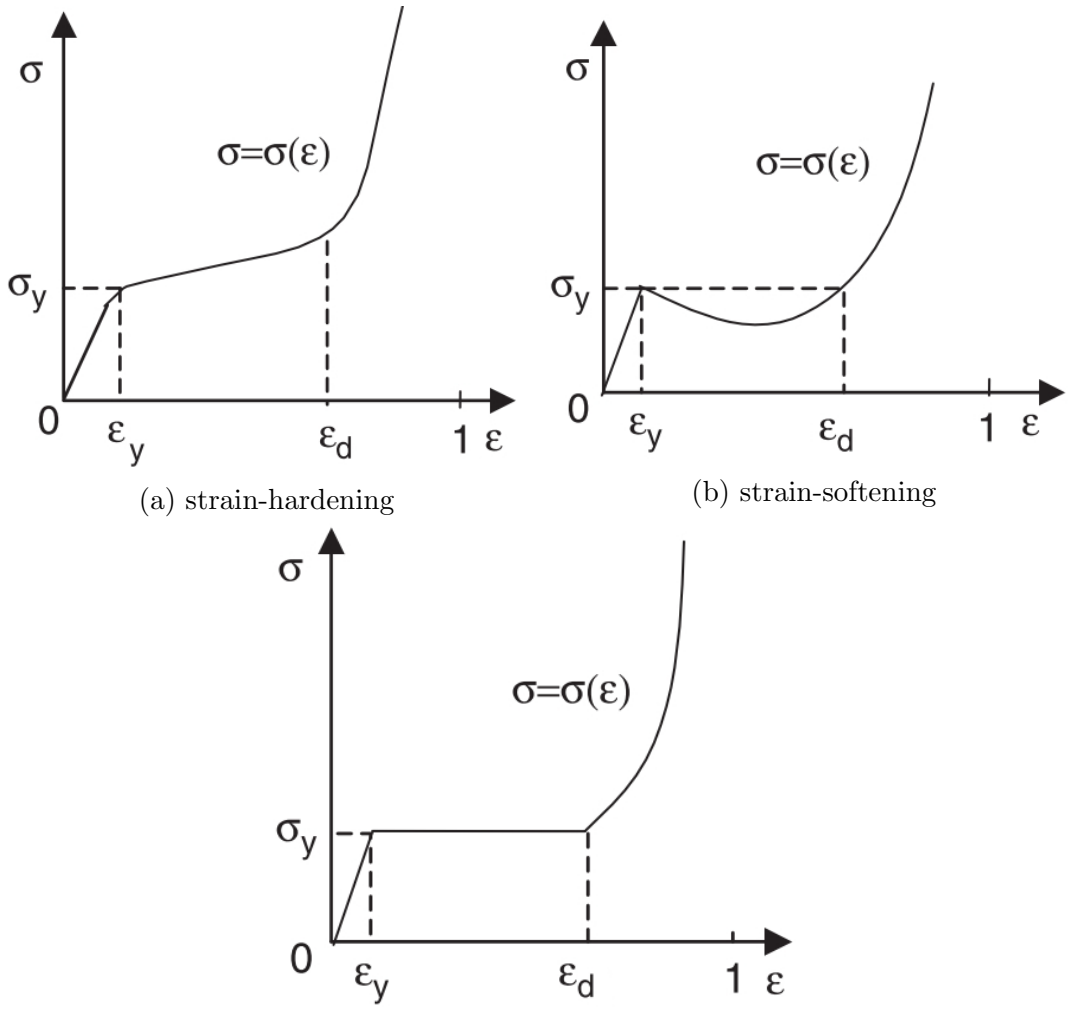

(a) strain-hardening

(b) strain-softening

(c) perfectly-plastic

Figure 2.1: Typical stress-strain characteristics experienced under uni-axial compression under quasi-static loading: 2.1a, stress-strain curve with strain-hardening characteristic; 2.1b, stress-strain curve with strain-softening characteristic; and 2.1c, stress-strain curve with perfectly plastic characteristics [42].

2.2 Blast Resistance

A blast wave describes the layer of compressed air that lies in front of the hot gas that is generated due to detonation of explosives; the blast wave contains most of the energy released by the explosion. Blast wave pressure time history is characterised by positive and negative specific impulses and by its peak value of

over pressure above ambient pressure, this over pressure decays as the blast wave expands further from the explosion source [45], as shown in Figure 2.2. The main characteristics of the pressure wave are the arrival time, t_A of the shock wave, including the time of the detonation wave to propagate through the explosive charge. The peak overpressure, P_{SO}, which is usually an instantaneous pressure rise and then decreases exponentially until it reaches the ambient pressure, P_0. The positive phase duration, t_O, which is the time for reaching the ambient pressure. After which the pressure drops below the ambient pressure until the maximum negative pressure, $P_{SO}{}^-$, where $t_O{}^-$ is the duration of the negative phase.

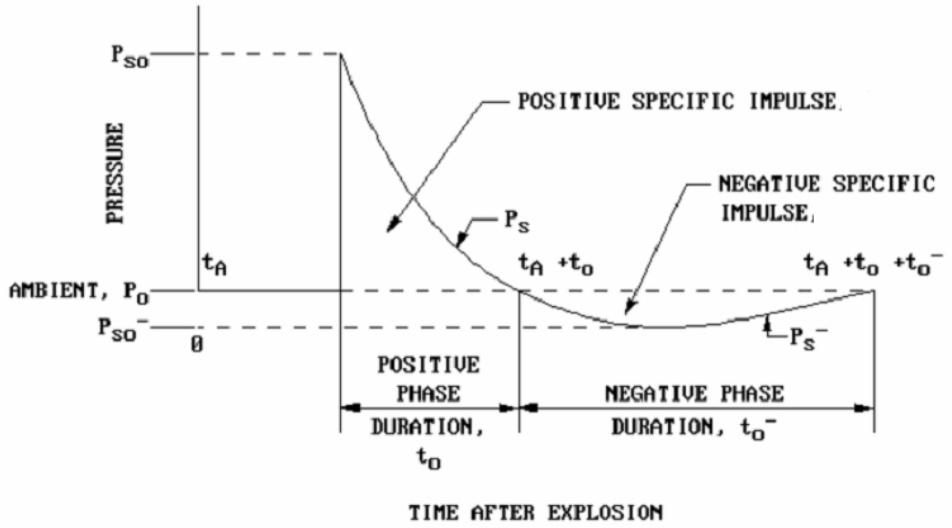

Figure 2.2: Typical pressure-time history from a far-field explosion [46].

High strain-rate characterisation can be carried out using a split-Hopkinson pressure bar (SHPB), which can be carried out in compression, tension or torsion. Despite various setups and techniques currently used for the SHPB, the principles for the testing and measurements are the same. That is, the specimen is placed between the ends of two straight bars, usually metallic, and these are known as the incident and transmitted bars. A striker (bullet) is released at a certain velocity and strikes the incident bar, this creates a stress wave (incident wave) which propagates through the bar reaching the specimen. Upon reaching the specimen

the incident wave is split into two smaller waves. One of the two smaller waves is known as the transmission wave which travels through the specimen and into the transmitted bar, causing plastic deformation in the specimen. The second wave is referred to as the reflected wave and is reflected away from the specimen and travels back into the incident bar. In order to measure these waves, strain gauges are placed on the bars to measure strains caused by the waves. With the assumption that the deformation of the specimen is uniform, the stress and strain can be calculated from the amplitudes of the incident, transmitted, and reflected waves.

SHPB tests have been used by researchers for high strain-rate ($10^3 - 10^4$ s^{-1}) testing. The SHPB enables one to establish a materials high strain-rate properties under compression, tensile, shear and torsion. It's popularity is due to the simplicity of the experimental procedure and is based on the early work by Bertram Hopkinson [47]. Typically the stress-strain relationship for the specimen material is established by the incident, reflected and transmitted waves. It is a common practice to measure the incident and reflected waves using a strain gauge at the center of the input and output bars [48]. Although it was initially developed for compression testing, it was extended by Harding *et al.* [49] and Duffy *et al.* [50] for tensile and torsion testing, respectively. This type of loading is a good indication of how a material will respond in blast loading scenarios, due to the high strain-rates that are involved.

Simulation of blast events can be considered complex and requires consideration of the blast wave pressure time history and special consideration of the structural response to the blast loading [15]. Figure 2.3 presents the various strain-rates that are associated with quasi-static, impact and blast loads. Blast loads usually involve very high strain-rates in the range of $10^3 - 10^4$ s^{-1}; the high strain-rate (loading) rate would change the dynamic and mechanical properties of target structures and consequently the expected damage mechanisms for various

structural elements.

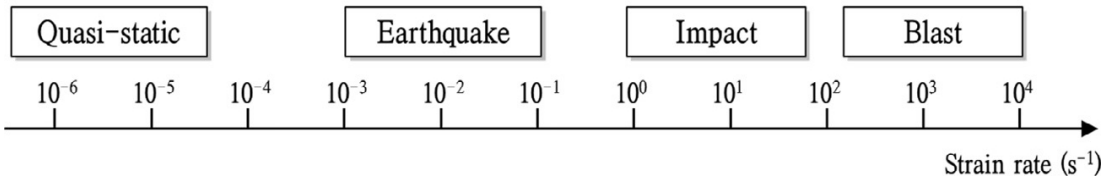

Figure 2.3: Strain-rates associated with different types of loading [51].

An explosive material is a reactive substance with high levels of potential energy. The sudden release of this potential energy results in an explosion. Explosives can be classified as low explosives or high explosives. The former is used primarily to propel projectiles, whereas the latter when detonated, creates a high energy shock wave. High explosives detonate at a faster rate than lower explosives ranging from 3-9 km/s. High explosives can be sub-categorised as primary and secondary explosives. Primary explosives consist of materials that can easily be detonated with the addition of heat as an ignition sources, i.e. impact, spark or flame. These types of explosives, an example of which is Lead Azide [15], are usually higher in cost in relation to secondary explosives and may be used as detonators to initiate secondary explosives. Secondary explosives have a much higher energy output in comparison to primary explosives. Examples of secondary explosives may include TNT (Trinitrotoluene) and RDX (Nitramide). PE4 (Plastic Explosive No. 4) is a British Military explosive and consists primarily of RDX, with large energy output of 5130 kJ/kg [15]. Blast loading on a structure is the consequence of an explosion or explosions and can be classified as:

- Nuclear explosions from subatomic activity and the result of the rapid release of energy from a high-speed nuclear reaction, as described by the well known $E = mc^2$ equation.

- Chemical explosions from rapid oxidation of fuel elements found in explosive compound, e.g. TNT or plastic explosives PE4.

- Physical explosions an example of which would be the rupture of a vessel with pressurised gas or liquid.

The response of structures subjected to both uniform and localised blast loading conditions has been a topic of investigation widely reported in the literature over the past four to five decades. It has been established that a materials' low failure strain is one of the limiting factors in the performance of composite laminates such as fibre reinforced plastics (FRPs) [52]. This is particulary critical in blast loadings, due to the high strain-rate impulsive loadings that are involved. Therefore, the search in finding a material which possess higher strain to failure property would be expected to perform better in blast and impact loadings [52].

Ballistic pendulums, an example of which is shown in Figure 2.4, are commonly used to test the blast response of a structure. Here, a controlled explosion is detonated on one end of the pendulum and directed down an open ended tube with the shock wave impending the structure that is to be analysed, resulting in oscillations of the pendulum. This will be discussed in more detail in Chapter 3.

Figure 2.4: Typical ballistic pendulum [53].

As described, the actual pressure-time loading associated with an explosion, is a complex decaying pressure oscillation. Many possible blast loading scenarios exist, in which simple empirical descriptions of the incident pressures on blast-loaded structures are complicated by close proximity detonation, high degrees of

confinement, and geometric variations [28]. There have been many ways to test shock wave loading on a structure other than controlled explosive detonations at various scales, including pressure blow down rigs, soft projectile impact and shock tubes.

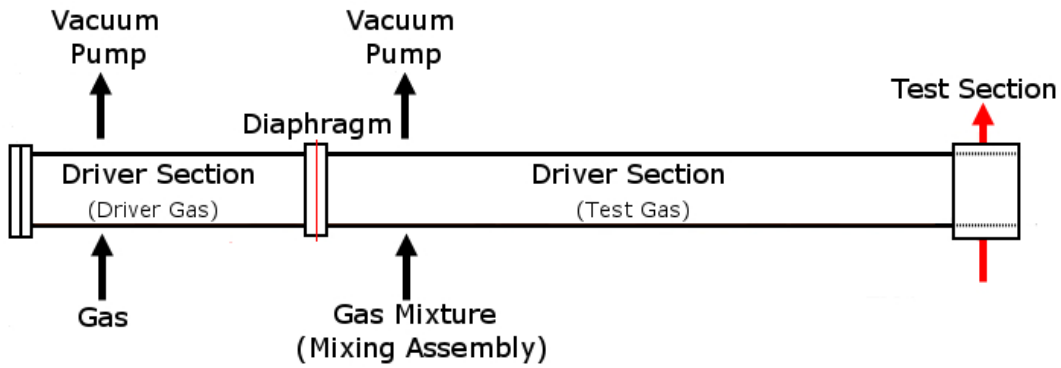

Figure 2.5: Diagram of a simplified shock tube.

A shock tube uses a similar principle to blast loading at far stand-off distances (SODs), since the length of the tube (SOD) is greater than the diameter of the exposed test plate area, which results in a uniform loading of the test specimen. A typical shock tube is illustrated in Figure 2.5. It is a device that is used to replicate and direct a blast wave towards a structure. It typically consists of a metallic tube made of two compartments, consisting of a high pressure one and a low pressure one, separated by a diaphragm. Once the gas in the high pressure compartment is increased to a predetermined high pressure, the diaphragm is ruptured, creating a propagating pressure wave that travels down the low pressure compartment toward the test specimen, positioned at the shock tube exit. Shock tube experiments are a safer alternative to the use of explosives and can be carried out in a safe and experimentally ideal environment; this allows for accurate measurements of the shock wave, as it is possible to direct the blast wave at various sensors, measuring devices and observing the structural response of target plates.

2.3 Sandwich Structures

One approach which has proven effective in providing impact or blast resistance, is to introduce a sacrificial layer surrounding the protected structure and to maximise the energy absorption with the use of a sacrificial layer [54–56]. Sandwich structures have been presented as a viable structure when bending stresses and super light-weight construction is of major concern, with an example being shown in Figure 2.6. The concept of sandwich construction can be traced back to the middle of the 19th century [20], however, it is thought that the principles of sandwich construction may have been applied much earlier. The inclusion of the sandwich concept began to generate momentum during the start of World War II, where the sandwich panels were exploited for their stiffness to weight ratios, high structural efficiency and durability.

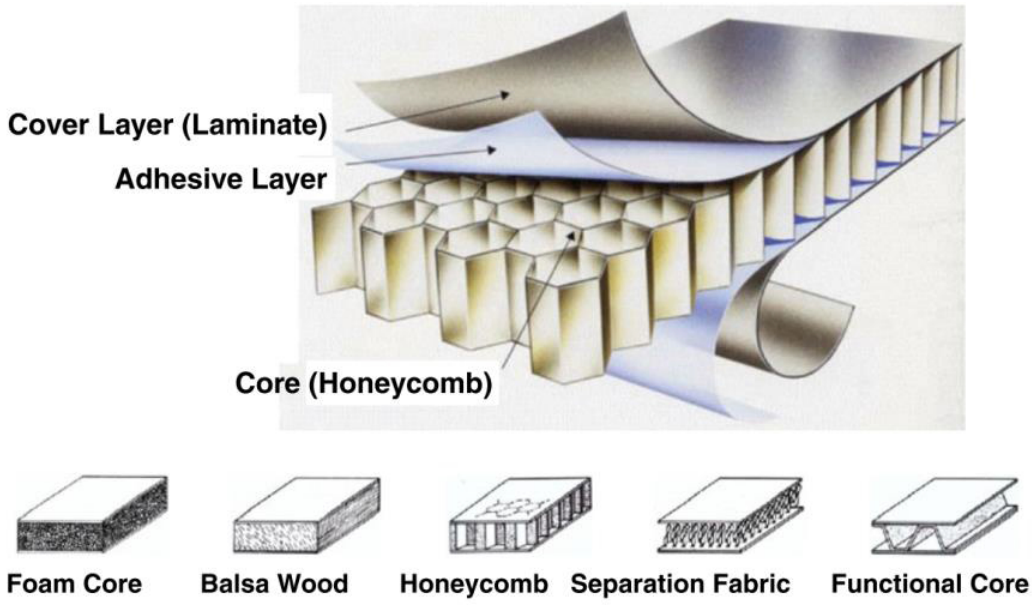

Figure 2.6: Construction of a sandwich structure [57].

Commonly, fibre composites, foams, magnetorheological (MR) fluids, or porous materials are used as high energy absorbing materials. However, sandwich structures present a interdisciplinary concept by enabling engineers to combine material selection, design and function integration for meeting the high requirements

of multi-functional modern day materials. Sandwich systems take advantage of the properties of the various material components, i.e. low density of core, high bend resistance of face sheet and core combination, sound and vibration insulation, high energy absorption, high load-capacity at a low weight. The core of a sandwich structure bears the shear loads, whereas the skins, i.e. outer face plates increase the stiffness and carry the bending forces [21]. Subsequently, they have been widely used as primary energy absorbing materials in the aerospace, naval and construction industries.

Early sandwich constructions used in aircraft structures had their facings made of plywood, wood pulp fibres, and their core made of cork, balsa wood, and synthetic materials such as cellulose acetate. Later aircraft and spacecraft applications had the faces and cores made of aluminum alloys, titanium and stainless steel [58]. Sandwich structures with composite facings have shown to be quite popular in the manufacturing of aircraft components due to their light weight, good mechanical properties and lack of corrosion.

Much research has been carried out to develop structures that are able to withstand various loads from LVI [23, 59–65], ballistics [66–69] and explosives [21, 70–76]. Fundamentally, their properties assist in dispersing the mechanical impulse that is transmitted into the structure. A great variety of design configurations have been used for sandwich cores. Generally, core materials may consist of polymer foams [23] and metal foams [22, 24, 25, 77] as well as honeycomb [21] and truss structures [27].

The mechanical behaviour of sandwich structures is strongly dependent upon the loading rate [78–80]. This is made apparent with quasi-static loading and dynamic loading. In quasi-static loading the structure can experience ductile behaviour, however for impact loading it may behave in a brittle manner and fail catastrophically. Structures should be designed to withstand quasi-static and fatigue loads in addition to maximum energy absorption in the case of an impact

- this requirement is in particular demand with the transportation industry.

The added benefit is by concentrating failure in the core region, which enables the face sheets to remain intact, preventing potentially injurious effects of fragmentation [81]. In order to investigate the damage and energy absorption characteristics specific to composite honeycomb sandwich panels, Zhou *et al.* [82] studied the effects of various skin thicknesses and core densities. It was established that by increasing the skin thickness an increase was seen in both the initial threshold and ultimate loads as well as the absorbed energy of the panels [81,82].

2.4 Fibre-Metal Laminates (FML)

Fibre-metal laminates (FMLs) have attracted interest from a number of researchers due to their improved fatigue and impact resistance [83–89]. FMLs belong to the class of heterogeneous mixtures examples of which include ARALL (Aramid Reinforced Aluminum Laminates). These FMLs were the first FML developed [53] and offer a fatigue resistant hybrid composite that consists of layers of thin high strength aluminum alloy sheets surface bonded with aramid fibers. Glass Laminate Aluminium Reinforced Epoxy (GLARE) have attracted a lot of interest from researchers [83, 85, 90] because of the improvement in fatigue and impact resistance. To be more precise FMLs are a stack of composite layers sandwiched between metallic sheets that provide excellent impact resistance in various applications [88] such as the work carried out by Vlot *et al.* [83] on the investigation of GLARE, which consists of a number of thin aluminium 2024-T3 sheets and a uni-directional/bi-axial glass-fibre-reinforced epoxy. Additional investigations on GLARE were carried out in 1996 by Fleisher [91] where data was presented from blast test results on a lightweight luggage container capable of withstanding a bomb blast greater than the Lockerbie air disaster in 1988.

Some of the drawbacks of thermoset-based FMLs are the long processing cycles

and low interlaminar fracture toughness properties [92]. However, new FMLs based on thermoplastic matrices developed at the University of Liverpool had shorter processing times and higher fracture toughness [93]. Additionally, FMLs made from glass fibre reinforced polypropylene (GFPP) composite were shown to be capable of absorbing significant energy with extensive plastic deformation in the aluminium and composite layers as well as localised microcracking of the glass-fibre reinforced polypropylene [90].

2.5 Core Materials

Core materials refers to the materials that form part of a sandwich structure with skins placed on the top and bottom faces. Many current core energy absorbers consist of honeycombs [78], thin walled tubes [94], metal foams [22, 25] and polymers [29]. Table 2.1 provides a comparison of the SEA of various metal foams, polymer foams and honeycombs in relation to the materials density.

Table 2.1: Specific energy absorption (SEA) comparison of various core materials.

Core	Material	Density (kg/m^3)	SEA (kJ/kg)
Metallic Foams	Al matrix syntactic foams toughened with Al particles [95]	1450-2050,	27.3-41.7,
	Closed-cell foamed Al [96]	270-430	27.56-30.22
Polymer Foams	Polyethylene (PE) [14]	69	1
	Polyisocyanurate (PI) [14]	80	9
	PolyMethacrylImide (PMI) [14]	52-160	12-17
	Polyurethane foam (PUF) [14]	72-104	2-3
	Polyvinyl chloride (PVC) [14, 23]	40-250	8-15
Honeycombs	Aluminium alloy (AA) 3003 [14]	28.6-82.6	9-16
	AA 5052 [14]	27-192	8-45
	Nomex [14]	29-48	7-13
	Nomex Ox [14]	48	14
	Polypropylene (PP) [97]	40	3.1
	Natural fibre [98]	0.1-0.4	0.6-6.5

It known that increasing the thickness of a sandwich structures increases its compression and flexural stiffnesses [99]. Cellular materials are commonly used for

sandwich cores due to their low density, enabling one to increase the sandwich core thickness without significantly increasing the weight of the structure [99]. Figure 2.7, provides a hierarchical description of some cellular materials classifications, where the cellular material with stochastic or periodic microstructures is configured as the cores of sandwich panel structures.

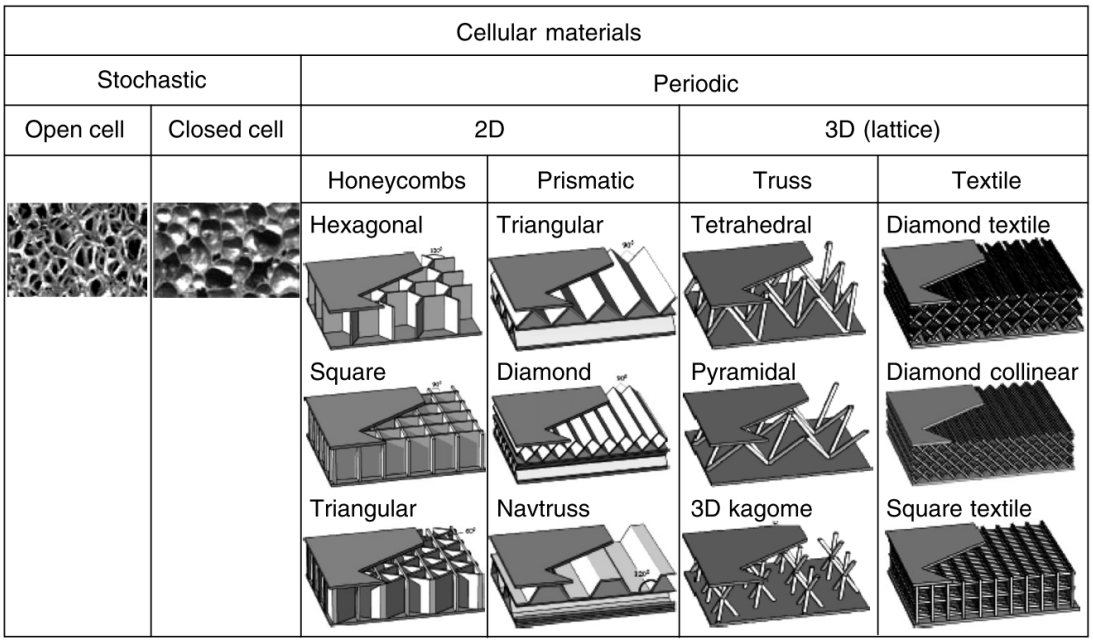

Figure 2.7: Heirarchical description of cellular materials classification [100].

2.5.1 Metallic core

Metal foams (metfoams) are characterised structurally by their cell topology, i.e. open or closed cells, relative density, cell size/shape and anisotropy. These foams - frequently aluminium - benefit from their low densities and novel physical, mechanical, thermal, electrical and acoustic properties. They are desirable for applications such as lightweight structures, energy absorption and for thermal management [43]. The cellular structure of a metal foam consists of a solid metal with a large volume fraction (VF) of gas filled pores with typical values within the region of 0.75 to 0.95 [100]. The VF is defined as the ratio of the volume of void space to the overall volume of the material. These pores may form an

interconnected network to form and open cell structure or the pores may be sealed forming a closed cell structure as illustrated in Figure 2.7. The strength of foamed metal possesses a power law relationship to its density, that is, a 20 % dense material is more than twice as strong as 10 % dense material [100]. The mechanical properties and fabrication state of the art of the metal foams have been extensively studied and documented [37, 43, 101].

2.5.2 Honeycomb

Lattice materials are not generally the best choice for energy absorption applications, instead hexagonal honeycombs, metal foams and egg-box materials prove to be the best candidates [102]. Egg-box structures have also been proposed for energy absorption and has similar energy absorption capacity as hexagonal honeycombs and is superior to that of metal foams [102]. Potentially they are cheaper than lattice material, honeycomb or metal foam as it has the advantage of being cold or hot stamped from a wrought sheet in a single step operation [102]. Honeycombs can be made of either Nomex, Aluminium or thermoplastics like polypropylene, and can be found in numerous aircraft applications [14].

The strength of honeycombs in terms of high energy absorption is through the formation of successful folds of each cell, with hoop stretching of the cell wall between each fold [102]. Each successive fold leads to large oscillations in the collapse stress. Contrarily, open-cell metal foams/closed-cell metal foams absorb energy primarily by the bending of the cell edges at stationary plastic hinges. In parallel to honeycombs, fluctuations in the macroscopic stress versus strain curve can be observered, however successive collapse of layers of the foam is the cause of this behaviour [102]. Deshpande *et al.* [102] experimentally and theoretically investigated the compressive collapse of egg-box material with the goal of establishing its ability to absorb energy. It was shown that the energy absorption capacity of egg-box material makes it a competitive candidate against

materials such as metal foams and honeycombs. It differentiates from metal foams in its deformation, as the material deforms by travelling plastic hinges which sweep through the micro-structure. In addition to this, each material element that enters and leaves the travelling hinge undergoes cyclic plastic straining.

2.5.3 Polymer cores

Polymeric materials are popular due to their flexibility in design since they can be manufactured into complex shapes, in addition to their low cost [37], corrosion resistance [103] and high energy absorption per unit of mass capacity [34]. Polymers have increasingly been implemented as the matrix for many composite structures for example carbon fibre reinforced polymers (CFRP). The most common polymers used are polystyrene (PS), polyvinyl chloride (PVC), polypropylene (PP), polyether-imide (PEI) and polyurethanes (PU), to name a few. The key to optimising polymer selection for impact resistance is to understand the correlation among mechanical properties, deformation mechanisms and failure.

The morphology of polymers has been reported to have a direct influence on their impact strength. In automotive applications, the dynamic deformation of polymers has been an important consideration in vehicle crashworthiness [103]. Additionally, the low velocity impact (LVI) energy absorbing characteristics of polymers have been applied in safety equipment and component packaging. At much higher strain-rates, polymers are proving to be a viable application in defense for blast resistance, spall containment and impact damage mitigation [103].

Polyvinyl Chloride (PVC)

PVC - Vinyl - is one of the cheapest and widely used of polymers, alongside polyethylene. PVC as its pure form, i.e. a thermoplastic, is rigid and not very tough [104]. The incorporation of plasticisers creates flexible PVC, a material with rubber-like properties. On the other hand, the introduction of reinforce-

ments, such as glass fibres, provides the material with sufficient stiffness, strong and tough mechanical properties that may be used on roofs, flooring and building panels [104]. Both the flexible and rigid PVC can be foamed to provide lightweight structural panels. This polymer can be blended with other polymers to extend the range of properties [104].

Polystyrene (PS)

Polystyrene (PS) is an optically clear, cheap, easily molded polymer. In its simplest form PS is brittle, however, the mechanical properties can be dramatically improved by blending PS with polybutadiene, this reduces transparency. Polybutadiene, a synthetic rubber, has a high resistance to wear. The single largest use of PS is foam packaging [104].

Polyether-imide (PEI)

Polyether-imide (PEI) is known for its high strength and rigidity, specifically under long-term heat exposure. It is an amorphous thermoplastic with characteristics similar to Polyether-ether-ketone (PEEK). The rigid aromatic imide units provide PEI with its high performance properties at elevated temperatures, whilst the ether linkages provide it with the chain flexibility necessary for good melt flow and processability [53]. It is well suited for extreme service environments [53]. At room temperature, its mechanical properties exceed those of most thermoplastics, and retention of these properties reach as high as 191 °C. PEI has proven itself to have commendable impact strength and ductility, displaying sensitivity when subjected to high strains [53].

Polyurethane (PU)

Polyurethanes were first discovered by Otto Bayer in 1937 [105] and encompass the series of polymers whose molecular backbone contains a substantial number of

urethane linkages, regardless of the content of the rest of the macromolecule [106]. The urethane linkage is formed via the reaction between an isocyanate group and a hydroxyl group. Initial studies into these polymers focused on forming linear polyurethanes by reacting diisocyanates with diols, but it was very quickly realised that a multitude of polymers with wide-ranging properties could be produced [107]. Early work focused on polyester-based polyols; however, the enhanced hydrolytic stability and immense versatility afforded by polyether-based polyols saw them become a preferred precursor in polyurethane synthesis [107]. Therefore, the vast selection of polyols, isocyanates, and chain extenders allows polyurethanes to be varied from soft thermoplastic elastomers to adhesives, coatings, flexible foams, and rigid thermosets [108].

Polyurethane foams (PUFs), are thermosetting polyurethanes, and have widely been studied and used in various areas of science and engineering for over 50 years. They are widely used as energy absorbers, mainly as a shock absorbing material in small transportation packages [109] - these are usually low density open-cell foams. These polymers are commonly formed by reacting a di- or poly-isocyanate with a polyol. Both the isocyanates and polyols used to make polyurethanes, contain two or more functional groups per molecule. PUFs are able to successfully compete with metals, plastics and rubbers depending on a particular application. Rigid PUFs are widely used in the building industry due to their characteristics, i.e. heat resistance and high softening point as well as their low density combined with high compression and bending strength [110].

Polyurethanes and polyureas both cure to yield systems that can vary from rigid to very flexible solids in their final properties. Polyureas are quite similar to polyurethanes, but with some distinct differences. Whilst polyurethanes are made from the reaction of an isocyanate with a polyol, polyureas are formed from an isocyanate reacting with a multi-functional amine. It is also possible to make so-called hybrid systems, in which the isocyanate is reacted with

a mixture of hydroxyl and amino groups. Polyureas react at a much higher rate than polyurethanes, and the systems can gel within a few seconds after mixing. Polyureas have therefore been successful in the coatings industry, where the two components are mixed using a spray equipment.

Whilst most polyurethanes are thermosetting polymers that do not melt when heated, thermoplastic polyurethanes (TPUs) are also available. The stress-strain behaviour of both polyurea and polyurethane have shown to present significant rate dependence [52, 111–113]. Within the polyurethane family, TPU has been popular due to its ability to alter its microstructure and thus its mechanical behaviour. It offers various physical property combinations and processing application and is highly elastic, flexible and resistant to abrasion, impact and weather [2]. TPUs are a class of polymers that bridge the gap between rubbers and plastics and their processing techniques span across extrusion, injection, blow and compression. There are three main chemical classes of TPU; polyester, polyether and a smaller class known as polycaprolactone. Polyether TPUs, are slightly lower in specific gravity than polyester and polycaprolactone grades. They offer a low temperature flexibility and good abrasion and tear resilience and provide excellent hydolysis resistance - making them suitable for water applications. A typical representation of a segmented TPU copolymer is shown in Figure 2.8.

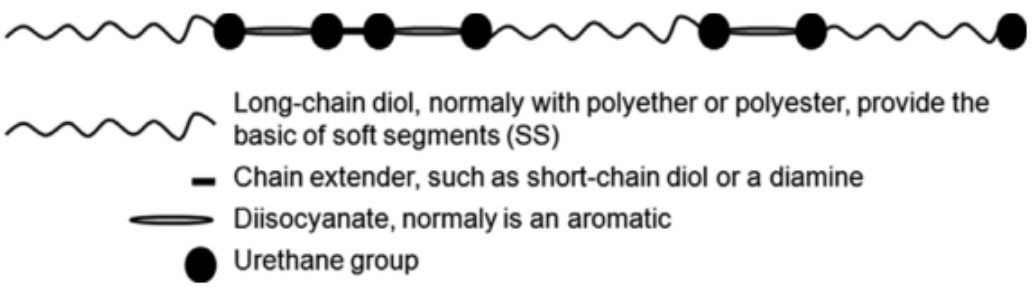

Figure 2.8: Schematic representation of a segmented TPU copolymer morphology [114].

TPUs cover an extremely wide range of applications today due to their re-

markable properties and versatility [115]. The superiority of TPUs properties are widely believed to be related to their multi-phase microstructure, in which the hard domains act as reinforcing filler connected by thermally reversible cross-links and embedded in the soft matrix [115–117]. These block co-polymers are composed of rubbery soft segments (SSs) and rigid hard segments (HSs) [115–117], as shown in Figure 2.9. TPUs are an important class of two-phase elastomers, and a better understanding of their behaviour is still necessary in the context of generic interest in the constitutive response of nano-structured composites [115].

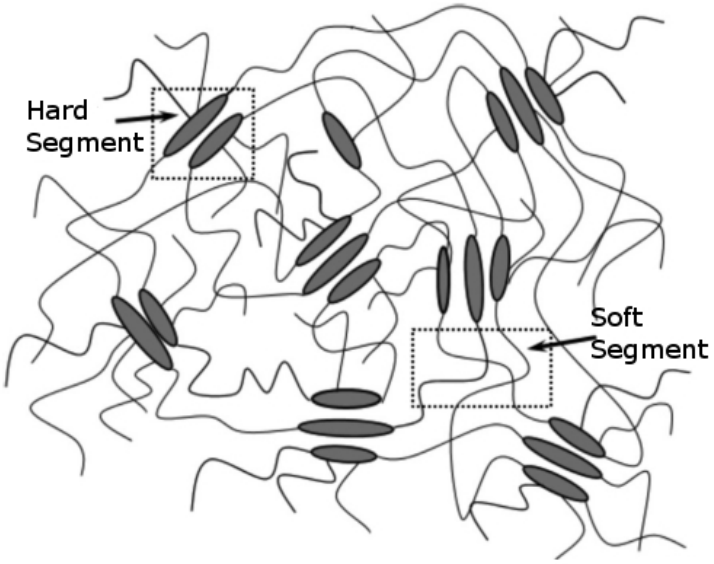

Figure 2.9: Schematic representation of TPUs morphology [114].

The versatility of TPU was exemplified by the study undertaken by Fahim *et al.* [118], which utilised the nanostructure of TPUs with the use of graphene nanopowder (6-8 nm). With the HSs acting as multi-functional tie points functioning both as physical cross-links and reinforcing fillers, while the SSs act as the elastomeric matrix accounting for the elastic properties of TPU, the presence of these two segments can show different extents of phase separation, offering new possibilities on tuning the polymeric matrix properties. The incorporation of graphene nano-powder led to enhanced electrical conductivity, thermal stability and compressive strength; opening up a new dimension for the production

of lightweight, low cost solar cells, packaging films, automobile components and biomedical applications including medical implants.

Bahei-El-Din and Dvorak [119] studied the effects of including an interlayer, such as polyurethane rubber and a fairly compliant elastomeric foam, between the outer face sheet and foam core. They concluded that these interlayers were capable of absorbing significant parts of the incident energy and protect the foam core from excessive deformation [81].

A summary of the advantages of TPU [120] are as follows:

- Abrasion resistant [113],
- Oil and solvent resistant; polyurethane has excellent resistance to oils, solvents, fats, greases and gasoline,
- Load bearing; Polyurethane has a higher load-bear capacity than any conventional rubber. Because of this characteristic, it is an ideal material for load wheels, heavy duty couplings, metal-forming pads, shock pads, expansion joints and machine mounts,
- Tear resistant,
- Weather resistant; polyurethane has outstanding resistance to oxygen, ozone, sunlight and general weather conditions,
- Excellent noise (acoustics) abatement properties [121]; the hard urethanes are now being used as gears in products where engineers desire sound reduction. The soft urethanes are used to replace rubbers for improved sound/vibration dampening,
- Flex-Life; most formulations offer extremely high flex-life and can be expected to outlast other elastomer materials where this feature is an important requirement. Dust boots, bellows, diaphragms, belts, couplings and similar products are made from urethane for this reason,

- Electrical properties; polyurethane has excellent electrical insulating properties and is used successfully in many moulded wire and cable harness assemblies.

2.6 Syntactic Foams

Perhaps one of the most commonly used reinforcements for polymer matrix composites is glass fibre, due to its low cost, high tensile, impact strength and high chemical resistance. Disadvantages however include relatively low modulus, self-abrasiveness, low fatigue resistance and poor adhesion to matrix resins. Glass fibres can be produced in either continuous filament or staple form [53]. Light polymer composites with a high specific surface are obtained with the use of hollow microspheres (HGMs), and have been named as spheroplastics [122–124]. Their distinctive features include low heat conductivity and density [125].

HGMs are widely used as fillers of polymer matrix syntactic foams (PSF), as a result of their low heat conductivity and density [125]. PSF are a class of lightweight materials that consist of thin-walled hollow particles, dispersed within a polymer material. Low-density sheet moulding compounds based on hollow glass microspheres are being increasingly used, particularly for boats and deep-water submarines [126] and as core materials for various other applications. These composites can present various advantages, i.e. lower weight, lower cost for low volume production in consequence of lower tool costs, no corrosion effects and more design freedom [126], in addition to their ability to provide high specific mechanical characteristics, i.e. specific compressive strength and stiffness. In particular applications such as impact loading, syntactic foams are a good application due to their ability to reduce impact force transmitted through the structure [127].

It has been illustrated in several studies that low density open cell polyurethane

foams filled with hollow microspheres can enhance the strength and elastic modulus of foams in compression [125, 128–133] as well as lowering the thermal expansion coefficient [129]. These gas filled foams are known to have very low mechanical properties and were enhanced by introducing microspheres to fill in the voids, increasing the mechanical properties. Despite the wide experience accumulated in the field of syntactic foams, it is nevertheless a topical area of study, due to the possibility to tailor the material properties by varying the size, wall thickness and volume-fraction. In addition to this, currently there is a lack of results which utilise the polyurethane resin as a solid matrix medium reinforced with hollow spheres [134], rather than a gas filled expanded foam.

2.7 Graded Structures

In addition to the syntactic foams, one may wish to modify the distribution of the particles in order to enhance the mechanical behaviour of the foams. Increasing a foams density may increase the Total Energy Absorption (TEA, E_T). However this is not always the case for specific energy absorption (SEA, E_s), that is, the energy absorbed (J) per unit mass of material (kg). In order to improve the energy absorption characteristics, one may continuously vary the foam density in a predefined manner; this is known as a functionally graded foam (FGF) [135]. Depending on a particular geometrical configuration, it is possible to obtain an optimal combination of thickness and density to maximise specific energy absorption of a structure [135]. The aim of a graded structure is to control the compression deformation behaviour of the material, which has been shown in several studies [64, 135–137] that graded structures can outperform their monolithic counterparts. Graded materials have their composition, density or microstructure changed in the through-thickness direction of the structure. Particularly for dynamic applications, these structures are attractive due to the

progressive response under dynamic loading.

Optimising the material response to dynamic loading has been a focus of study for many researchers [138–141]. During an impact event, functionally graded foams are capable of reducing the duration of the high acceleration. This provides a benefit for many applications such as the head protection industry, as many head injury criteria, i.e. HIC (Head Injury Criteria) [142], HIP (Head Injury Power) [143] and GAMBIT (Generalised Acceleration Model for Brain Injury Threshold) [144] require acceleration durations as indicators of the likelihood for a person suffering significant head trauma. In this respect, functionally graded foams may provide benefits for protective headgear, by reducing the risk of brain injury to the wearer after a fall [145]. Likewise, FGFs may be applicable to vehicles by providing the benefit of progressive deceleration which in turn lowers the g-forces that contribute to serious injury of passengers.

2.8 Reinforcement(s)

Composite materials offers substantial energy-absorption and crashworthiness properties, which have attracted the attention of a range of sectors. In 2011, the Lamborghini Aventador LP700-4 was the first production car to apply a fully carbon fibre monocoque design for a lightweight structure capable of absorbing the high levels of energies associated with a car crash [146]. Carbon fibres (CFs) are a widely used reinforcement for composites due to its high modulus and high strength. In the carbon structure, carbon atoms are arranged in the form of hexagonal layers with very dense packing in the layer planes. The high strength bond between carbon atoms in the plane result in an extremely high modulus, whilst the Van der Waals type bond between the neighbouring layers results in a lower modulus in that direction [53].

Attempts have been made to introduce metallic tubular structures in the

design of crashworthy designs, placed in strategic locations. If designed correctly, the introduction of tubular structures are capable of absorbing significant energy when loaded in an axial direction [147]. There have been several studies reported on the axial crushing behaviour of composite and metallic tubes [96, 148–155]. It has been shown that composite materials can offer extremely higher values of SEA than metallic tubular structures [30, 31, 148, 156–166]. The purpose of crush tubes is to absorb and convert kinetic energy into gross plastic deformations under severe loading conditions. The energy-absorbing capacity of such tubes has attracted interest from vehicle manufactures, i.e. Chrysler and Ford. As a matter of fact, Jacob *et al.* [165] calculated that 0.66 kg of higher performance thermopastic matrix composite is required to absorb the energy of a medium-sized car traveling at 35 mph.

Alia *et al.* [97] reported the findings of low density polymer foams reinforced with T700 CFRP tubes, with promising results. The specific energy absorption (SEA) was shown to increase with decreasing inner diameter to thickness ratio and it was shown that a tube with a diamteter to thickness ratio of 6.3 provided the highest energy absorption per unit mass.

In contrast to metals, especially in compression, most composites are generally characterised by a brittle rather than ductile response to loadings. While metal structures collapse under crush or impact by buckling and/or folding in accordion (concertina) manner which involves extensive plastic deformation, the failure of composites is characterised by fracture mechanisms involving fibre fracture, matrix cracking, fibre-matrix debonding, delamination and inter-ply separation. To reduce the overall weight and improve the fuel economy of vehicles, more and more metal parts are being replaced by polymer composite materials. The total energy absorbed (E_T) during progressive crushing of a composite tube in splaying mode is given by,

$$E_T = E_{lc} + E_{sf} + E_{ff} + E_{fr} + others \tag{2.6}$$

where, E_{lc} is the energy required for longitudinal cracking of the tube wall, E_{sf} is the energy required for splitting of fronds into beams, E_{ff} is the energy required for fibre fracture, and E_{fr} is the energy associated with frictional heating. Frictional heating occurs due to the sliding of fronds against the crushing platen, sliding of fronds against the debris wedge, and relative motion between the split fronds.

Farley and Jones [167] reported four crushing modes for carbon fibre tubes, i.e. transverse shear, fragmentation, lamina bending and splaying, as shown in Figure 2.10. These modes are said to be very useful in designing a structure that is able to decelerate an object in impact events. Only brittle fibre reinforced composites are able to crush in transverse shearing and lamina bending modes.

The actual mechanisms and sequence of damage are highly dependent on the geometry of the structure, lamina orientation, type of trigger and crush speed, all of which can be suitably designed to develop high energy absorbing mechanisms. Introducing a chamfer, i.e. trigger to one end of a tube enables an initiation of crushing, where failure begins at the chamfer tip and the damage zone propagates down the tube without catastrophic failure [30]. The SEA capability and the progressive crushing modes are affected by the type of reinforcing fibres used in the composite material. Hamada *et al.* [30] showed experimentally that thermoplastic tubes display higher energy absorption capabilites than thermoset tubes. This attribute was due to the superior fracture toughness of thermoplastics compared to thermosets. Hamada *et al.* [30] also tested various thermoplastic matrices, i.e. poly-ether-ketone (PEEK), polyetherimide (PEI), polyimide (PI) and polyarysulfone (PAS). Among the thermoplastic tubes investigated, the carbon/PEEK tubes displayed the highest energy absorption capability [30].

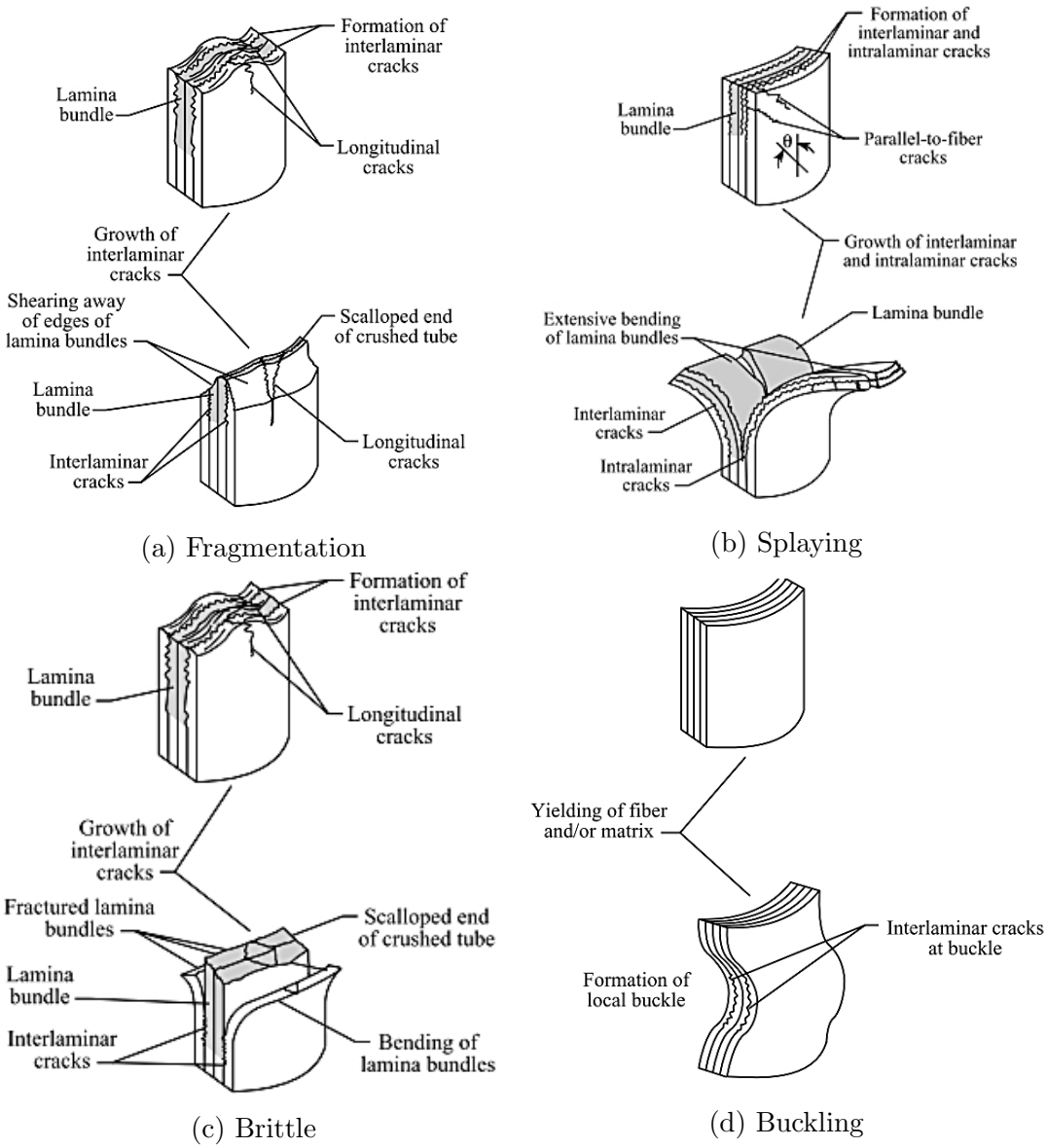

(a) Fragmentation (b) Splaying

(c) Brittle (d) Buckling

Figure 2.10: Crushing characteristics of continuous fibre-reinforced composite tubes (a) fragmentation, (b) splaying, (c) brittle and (d) buckling [168].

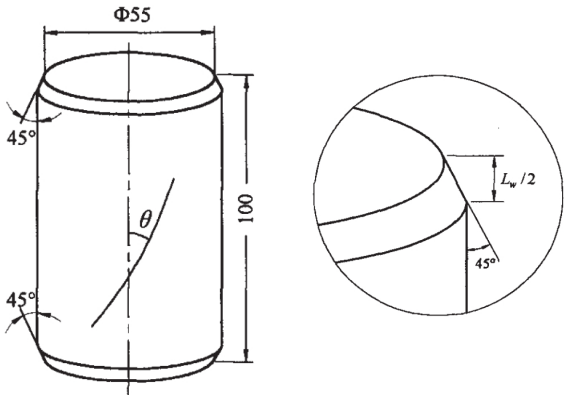

Figure 2.11: Double Chamfer Trigger (mm), where L_w is the weakened length [173].

Many researchers have reported that the main factors affecting energy absorption are testing conditions, tube geometries, constituent materials and fabrication conditons [31,156,157,159,168–172]. Song *et al.* [173] investigated the energy absorption behaviour of double-chamfer triggered continuous glass fibre reinforced epoxy circular tube as shown in Figure 2.11, and focused on the influence of fibre ply orientation and trigger pattern. When constituent materials and fabrication techniques are established, ply pattern is the key factor that affect crushing behaviour, including macroscopic collapse mode, microscopic energy dissipating mechanisms, crushing force history and energy absorption efficiency - these are interrelated [173]. Chamfer angles between 30° to 45° are recommended to initiate stable crushing [174].

2.9 Numerical Modelling

Experimental testing has limitations in allowing a researcher to fully understand the response of a structure subject to an explosion due to the destructive capability and short durations of dynamic events as well as difficult instrumentation. This is in addition to the costly nature associated with experimental trials. For this reason, accuracy in numerical modelling of these events is important as it reduces the costs and time involved in assessing a design against blast load. Modelling issues which are subject to research include consideration of strain-rate effects of the various materials [175]. Establishing a good mesh discretisation, i.e. the process of transferring continuous functions, models and equations into discrete counterparts, can reduce the percentage of error, providing optimal results.

Many researchers have been taking full advantage of the developments of computing technology and focused on the numerical simulations rather than experiments which proves to be both convenient and economical [176]. The finite element analysis (FEA) is perhaps the most powerful computational methods when structural analysis of composites materials is the aim. A starting point for analysis would be in the use of a validated finite element (FE) model, with a reasonably fine mesh, correct boundary conditions and material properties, to name a few. A reasonable resemblance needs to be obtained for stress and strains to that of the real structure, as a minimum requirement.

A central aim of computational material physics is to accurately describe specific materials on length scales that span from electronic to macroscopic. The hetrogenous nature of materials suggests that there will be microscale constituents whose composition, orientation and evolution influence macroscale properties [177]. Figure 2.12 shows a variation in the typical length scales used in computational materials science, where the length scales for describing the response of materials range from atomic ($< 10^{-9}$ m) to structural length scales.

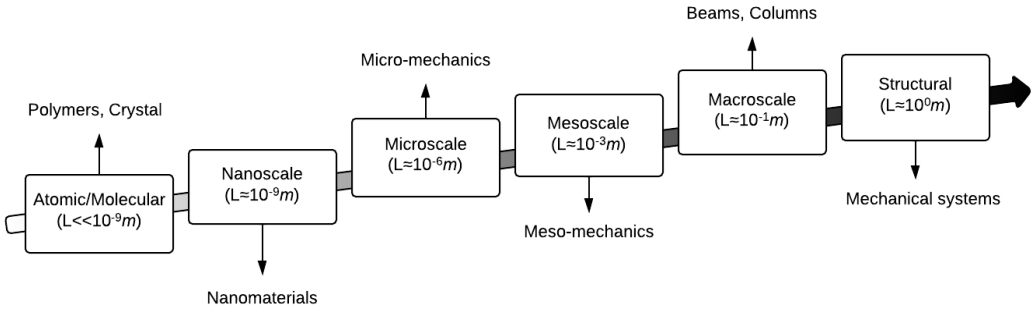

Figure 2.12: Length scales used in computational materials science.

Hydrocodes are computer codes that encompass several different numerical techniques in order to solve a wide variety of non-linear problems in solid, fluid and gas dynamics. They are particularly suited to modelling blast, impact and penetration events [178]. These codes are popular due to their ability to handle complex problems where a Lagrange processor and an Eulerian processor can work side by side on the same problem. The Lagrange processor uses a mesh which deforms with the material it contains while the Eulerian processor has a fixed mesh in space which allows the material to move through it [178]. The Lagrange processor is typically used for solid, continuum structures, while the Eulerian processor is used for modelling gases, liquids or solids where large deformations are likely to occur. The phenomena to be studied with such programs could be characterised as highly time dependent with both geometric non-linearities, such as large strains and deformations, and material non-linearities, such as plasticity, failure, strain-hardening and softening, multiphase Equation of State (EoS) [179].

AUTODYN [180] is one hydrocode program which is used to resolve problems involving the interaction of structural, fluid and gas simultaneously [176]. Three types of Eulerian solvers are provided in AUTODYN: Euler, Euler Godunov and Euler Flux Corrected Transport (FCT Euler). The Euler solver used in AUTODYN 2D is based on a first-order approach which enables multi-material to be modelled. However, second order schemes are only available in AUTODYN

3D where applications are usually used in the blast and ballistic analysis. It has the capability to allow different solver (or processor) as Lagrange, Euler to function simultaneously in a one model analysis [176].

ABAQUS [181] and LS-Dyna [182] are general-purpose FE programs used to analyse the nonlinear dynamic response of 3D structures. They can predict how a prototype is likely to respond to real-world events, with the purpose of minimising the time spent in design. They incorporate fully automated contact analysis capability and error-checking features enabling users to solve many complex problems, and are able to perform Lagrangian dynamic analysis with an explicit, central difference integration scheme.

2.9.1 Modelling polymers

Numerical modelling of polymerical foams can be considered somewhat complex, which is predominate when the cellular material involved presents well defined elastic and plastic anisotropic mechanical behaviour. This occurs particularly for dynamic and quasi-static structural analyses for sandwich composite aircraft structures, where skins are made from composite material and the core is comprised from polymeric foams [183].

The microstructure of the cells influences strength and stability of a polymeric foam [184]. The research carried out by Gong *et al.* [184] set out to understand the response of open cell foams in uni-axial compression. It was established that the microstructures consist of interconnected frameworks forming cells with nearly straight edges. The anisotropic mechanical behaviour is not an uncommon characteristic found in foams. The micro mechanisms of failure is of great significance in the hardening process, since the mechanisms can indicate brittle, plastic or perfect plastic response of the material after its elastic regime and according to the type of loading applied [183].

In order for one to master the modelling of such structures and materials, it

is important to revise the theories of elasticity and plasticity in order to properly manage yield surfaces and hardening laws [183]. With the addition of numerical issues from non-linear FEA to these various elastic-plastic behaviours makes the modelling of anisotropic response a significant task. A user subroutine may need to be used to implement a particular material model, if the material model in FEA software does not yield representative results. It is to be noted that numerical issues that arise from the assumptions made in the implemented material model can accumulate in the simulations rendering large errors.

Although, isotropic material models are important, the anisotropic degree of cellular materials is often neglected without any insight into the material's micromechanics. One of the disadvantages of considering anisotropic material models is number of parameters that need to be identified; usually up to ten different types of experimental tests are required. For simplicity, many engineers and designers prefer to use isotropic material models in order to predict the mechanical behaviour of products made from anisotropic cellular materials, in order to save time and cost for experimental testing [183].

2.9.2 Modelling composites

There is a requirement for reliable FE models of composite materials under dynamic loading. The orthotropic nature of such materials means that predicting damage in advanced composites currently are either highly complex or inaccurate due to their simplicity. Many parameters need to be taken into account when predicting damage which can be divided into four areas, i.e. a failure criteria approach which can be based on equivalent stress or strain, a fracture mechanics approach based on energy release rates, a plasticity or yield surface approach and a damage mechanics approach. This is in contrast to the numerical modelling of metallic materials which are generally taken as isotropic and can be analysed using a elasto-plastic model [185].

A number of failure theories are available in the literature, which do not just predict the initiation of failure but also for progressive failure up to ultimate load. The popularity of failure theories resides in their ease of use, examples of which include, maximum strain, maximum stress, Tsai-Hill, Tsai-Wu [186] and Hashin [187] failure theories due to their simplicity, ease of understanding and implementation in analysis.

Failure criteria approaches to modelling composite failure have generally been developed and restricted to the static regime [188]. They can be divided into specific failure criteria for various damage mechanisms, or polynomial-based criteria, such as the Tsai-Wu [186] failure criterion, which describes the failure surface in stress or strain space [188].

Models for progressive failure of composite structures range from the simple material property/stiffness degradation methods (MPDM) to the more sophisticated MPDM based on continuum damage mechamics (CDM) and fracture mechanics (FM). The methodology behind MPDM is that the damage material post-initial failure behaviour is modelled by reduced stiffnesses [189]. CDM has not only been used to model general damage in composites but also delaminations. within the framework of MPDM, CDM-based approaches to stiffness reduction appear less arbitrary since they are based on irreversible thermodynamics considerations [189].

FEA usually use strength-based failure criteria to predict failure events in composite structures. A number of criteria exist for uni-directional (UD) laminas subject to plane stress. The most commonly used are maximum stress criterion, maximum strain criterion, truncated maximum strain criterion and interacting failure criterion [190]. In ABAQUS, Hashin, maximum strain and maximum stress failure criteria are deemed adequate failure criteria [190].

The Hashin failure criteria (HFC) [187] presents four separate modes of failure i.e. fibre tension, fibre compression, matrix tension and matrix compression, these

are predicted by the following set of equations:

(a) Tensile fibre failure,

$$F_f^t = \left(\frac{\hat{\sigma}_{11}}{X^T}\right)^2 + \beta\left(\frac{\hat{\sigma}_{12}}{X_L}\right)^2, \text{ if } \hat{\sigma}_{11} \geq 0 \tag{2.7}$$

(b) Compressive fibre failure,

$$F_f^c = \left(\frac{\hat{\sigma}_{11}}{X_T}\right)^2, \text{ if } \hat{\sigma}_{11} < 0 \tag{2.8}$$

(c) Tensile matrix failure,

$$F_m^t = \left(\frac{\hat{\sigma}_{22}}{Y_T}\right)^2 + \beta\left(\frac{\hat{\sigma}_{12}}{S_L}\right)^2, \text{ if } \hat{\sigma}_{22} \geq 0 \tag{2.9}$$

(d) Compressive matrix failure,

$$F_m^c = \left(\frac{\hat{\sigma}_{22}}{2Y_T}\right)^2 + \left[\left(\frac{Y_C}{2S_T}\right)^2 - 1\right]\frac{\hat{\sigma}_{22}}{Y_C} + \left(\frac{\hat{\sigma}_{12}}{Y_C}\right)^2, \text{ if } \hat{\sigma}_{22} < 0 \tag{2.10}$$

where X_T and X_C are the tensile and compressive strengths in the longitudinal directions. Y_T and Y_C are the tensile and compressive strengths in the transverse directions. S_L and S_T are the longitudinal and transverse shear strengths. β is a weight factor to give more or less emphasis to the influence of shear on fiber failure. In many cases β can be set to zero, where it is assumed that there is no shear stress contribution involved in the initiation of fibre tensile failure.

The material stiffness is given prior to damage initiation as,

$$\sigma = C_d\epsilon \tag{2.11}$$

The damage elastic matrix which provides a relationship between stress and strain controls the degradation of the materal stiffness and can be expressed as,

$$C_d = \frac{1}{D_h}\begin{bmatrix} (1-d_f)/E_{Y1} & (1-d_f)(1-d_m)\nu_{21}/E_{Y1} & 0 \\ (1-d_f)(1-d_m)\nu_{12}/E_{Y2} & (1-d_m)/E_{Y2} & 0 \\ 0 & 0 & (1-d_s)GD_h \end{bmatrix} \tag{2.12}$$

where G is the shear modulus and D_h is an overall damage variable which is expressed as,

$$D_h = 1 - (1-d_f)(1-d_m)\nu_{12}\nu_{21} \tag{2.13}$$

where d_f, d_m and d_s reflect the current state of the fibre, matrix and shear damage, respectively.

Generally, micro-mechanical and macro-mechanical models are used for the crushing of composite materials [191], as illustrated in Figure 2.13. In order to accurately reproduce the matrix crack propagation phenomenon, a micro-mechanical FE model is required, using a fine solid 3D mesh [192]; since the interface of some hydrocodes, i.e. ABAQUS, is limited, the material model needs to be defined using a custom material model, i.e. UMAT or VUMAT [89, 192]. These types of analysis involve a higher number of elements resulting in larger computational cost and are usually used in cases where crack growth in the main focus [191].

Thorough testing of advanced constitutive models with the purpose of simulating experimental results generally requires complex finite element models such as, advanced structural elements, thermomechanical loading, complex loading conditions, contact and friction conditions and static and dynamic analysis. A materials' model developer should not focus on the development and maintenance of the FE model rather one should focus on the development of the material model.

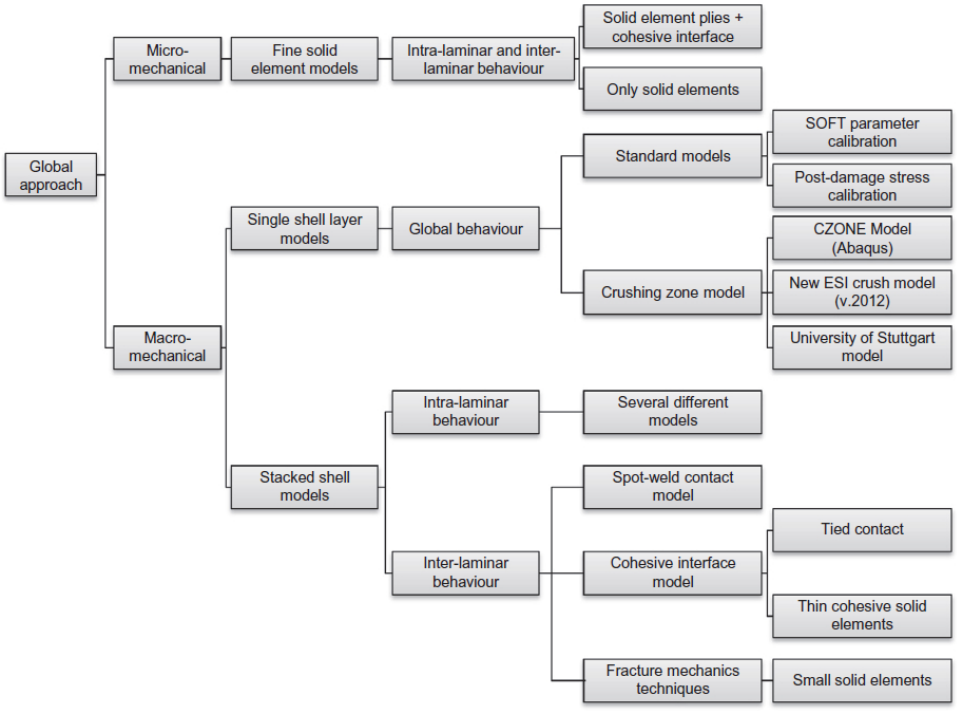

Figure 2.13: Classification of composite crushing numerical models [191].

2.9.3 Modelling blast loading

The dynamic loads originated by explosions are impulsive and result in high strain-rates in the material [193]. These types of loads, generally, invoke behaviour such as overstrength and increased stiffness in relation to the characteristics observed in quasi-static loading. It is therefore crucial for correct validation to be carried out of any theoretical and numerical schemes that may be used for structural designs involving high strain-rate loadings that are associated with blasts, produces significant displacements and damage. Many researchers depend exclusively on blast analysis using simulation techniques without sufficient test results in developing new blast resistant materials due to national security reasons and limited explosion test sites [194].

There are a number of numerical ways to apply impulsive blast loads to a structure, such as a simplified pressure pulse loading, empirical models such as CONWEP (Conventional Weapons Effects Program) or fluid structure interaction

(FSI). The former two rely upon the Lagrangian approach, which allows the use of a much smaller model since only the structure is modelled, whereas the the latter involves a Lagrangian-Eulerian coupling, which requires a much larger model, i.e. the fluid and structure domain, and therefore increased computational cost.

Pressure pulse loading

The actual pressure-time loading associated with an explosion is a complex decaying pressure oscillation that may require simplification when modelling the effects of blast on structures. In order for one to use rectangular pressure pulse loading for a complex pressure distribution over the blast area, the impulsive loading theory can be implemented, so long as the impulse is represented accurately. Due to inertia, the blast impulse can be transferred to the plate before the plate starts deforming. The pressure loading with the implementation of a rectangular [195, 196] or triangular [195] pulse, applied to the exposed blast area for a certain time. The time in this instance is identified once the intensity of the pressure pulse provided a negligible contribution to the deformation of the panels. The pressure pulse can be defined as,

$$P_{SO} = \frac{I_m}{A\tau} \tag{2.14}$$

where, P_{SO} is the peak overpressure, I_m the measured impulse from the experiment, A the blast area on the plate tested and τ is the blast load duration.

The impulsive loading assumption enables the simplification of the pressure-time load, as long as the impulse is represented accurately. The work presented by Farrow *et al.* [195] investigated the use of both rectangular and triangular pressure pulse loading for the prediction of midpoint deflections, deformation shapes, residual strains and dynamic yield stress of circular plates subjected to uniform blast loading, using the ABAQUS finite element software. It has been

reported [195] that these types of simplified pressure pulse loading are able to produce favourable predictions when the predictions of midpoint deflection is the aim. Simplifications of the blast loading pulses, i.e. rectangular and triangular, are displayed in Figure 2.14, and represented by Equations (2.15) and (2.16), respectively.

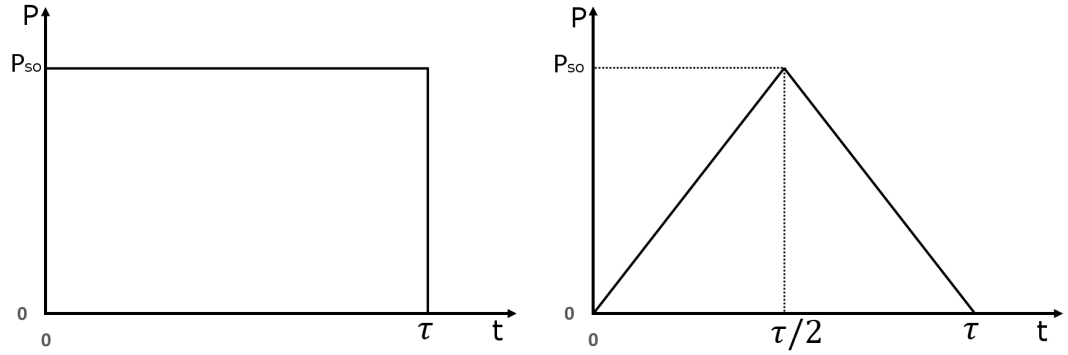

(a) Rectangular (b) Triangular

Figure 2.14: Simplified pressure-time loading histories for rectangular and triangular pressure pulse loading .

$$P(t) = \begin{cases} P_0 & 0 \leq t \leq \tau \\ 0 & t > \tau \end{cases} \tag{2.15}$$

$$P(t) = \begin{cases} \frac{2P_{SO}}{\tau} \cdot t & 0 < t \leq \tau/2 \\ 2P_{S0} - \frac{2P_{SO}}{\tau} \cdot t & \tau/2 < t \leq \tau \end{cases} \tag{2.16}$$

Empirical models

The severity of blast, for a given explosive, depends on the charge weight and stand-off distance which are usually combined into a single parameter called scaled distance (Z) [197, 198]. Empirical models that enable the computation of structure blast loading are based on abacuses which are themselves functions of the scaled distance:

$$Z = \frac{D_s}{\sqrt[3]{W}} \tag{2.17}$$

where D_s is the distance to the charge and W is the mass of the charge. These abacuses define parameters which in turn define incident and reflected pressure shock waves. Only the positive phase of the wave is defined and as a result, the pressure profile could be defined by abacuses interpolations.

Empirically developed applications such as CONWEP [199] and TM51300 (available in LS-DYNA) are methods of modelling blast loads. There has been extensive research to date on the use of CONWEP as a blast loading technique [200–203]. The CONWEP program is made up from a collection of conventional weapons effects calculations from empirical relationships and curves, as defined by TM5-855-1 [204]. This program was developed by the US Government for military purposes and is now publicly accessible in softwares such as ABAQUS, AUTODYN and LS-DYNA. CONWEP assumes an exponential decay of the pressure with time as described by the Friedlander equation (2.18) [205].

$$P(t) = P_{SO}\left[1 - \frac{t - t_A}{t_O}\right] exp\left[\frac{-A_D(t - t_A)}{t_O}\right] \tag{2.18}$$

with $P(t)$ as the pressure at time, t; P_{SO} as the peak incident pressure; t_O as the positive phase duration; A_D as the decay coefficient and t_A as the arrival time [199]. The decay constant is iteratively calculated from the impulse, overpressure, and duration of the positive equation as:

$$I = \int_{t_A}^{t_A + t_O} p(t)dt \tag{2.19}$$

By utilising TNT equivalency tables, CONWEP enables a user to accomodate for a variety of explosives. This equivalence is used to quantify the energy released by a mass of a specific explosive in relation to the equivalent mas of TNT, i.e. relative effectiveness factor (R.E.). The R.E. number for PE4 for example is 1.33 [18]. The charge diameter and stand-off distance (SOD) ratio needs to be taken into consideration in order to stay within the capabilities of CONWEP.

Ideally, CONWEP should be used for spherical charges detonated in unconfined free air blast conditions, however, scaling factors may be implemented within ABAQUS for a cylindrical disk shaped charge detonated in a vented tube.

Fluid Structure Interaction (FSI)

The propagation of blast waves in an air domain is governed by three fundamental equations of fluid dynamics, i.e. mass conservation, momentum conservation and energy conservation equations, which combine to yield the Navier-Stokes equation that governs the blast wave propagation in air [206]. In 1958, von Neumann [207] provided a solution of air blast from a point source explosion in an infinite three-dimensional space, with the assumption that the air was an ideal gas. The EOS and total energy for the air were defined as $P = c\rho T$ and $E = [c/(\gamma - 1)]T_{abs}$, where c is the specific gas constant defined by Equation (2.20), γ as the heat capacity ration defined by Equation (2.21) and T_{abs} is the absolute temperature.

$$c = c_p - c_v \tag{2.20}$$

$$\gamma = \frac{c_p}{c_v} \tag{2.21}$$

where c_p is the specific heat under constant pressure and c_v is the specific heat under constant volume.

Von Neumann [207] concluded that the free air blast pressure (P) could be expessed as,

$$P = \frac{8}{25(\gamma + 1)}\rho_{air} f(t, \gamma, \theta) \tag{2.22}$$

where ρ_{air} is the initial density of the air before blast, t is the time, γ is the heat capacity ratio and θ is a parameter representing the location of the point of interest in the free air domain. $f(t, \gamma, \theta)$ is a complication function of t, γ, and

θ; valid for $1 < \gamma < 2$. Equation (2.22) showed that, by increasing the initial air density ρ_{air}, the blast pressure in the air, due to explosion, would increase. This theoretical fact can be employed to increase the blast pressure in numerical simulation and to partially compensate the loss of energy, or numerical damping, due to large element size.

In an ideal sense, during an air-blast simulation, the air and detonation products, as well as the structural response of the target should be considered simultaneously [208]. For this an Arbitrary Lagrangian Eulerian (ALE) technique is typically developed for the analysis of high-explosives on the dynamics of the generated pressure wave, the CONWEP approach is not an adequate approach to model such situations [209]. Using this approach, the air and detonation products may be described by utilising an Eulerian formation in a gaseous domain, whilst the structural response can be treated in the Lagrangian domain. This approach however, requires considerably more computational time in relation to the simplified pressure pulse or CONWEP loading models.

An issue which is related to the accurate modelling of explosion phenomenon using ALE, is the application of a proper equation of state. One of the most widely used is the Jones-Wilkins-Lee (JWL) [210] equation, which scales the pressure of detonation products as shown in Equation (2.23). The JWL equations describe the pressure generated by chemical energy of the condensed explosive.

$$p = A\left(1 - \frac{\omega\rho}{R_1\rho_0}\right)e^{-R_1\frac{\rho_0}{\rho}} + B\left(1 - \frac{\omega\rho}{R_2\rho_0}\right)e^{-R_2\frac{\rho_0}{\rho}} + \omega\rho E_m, \tag{2.23}$$

where the constitutive properties A, B, $R1$, $R2$, and ω are empirically determined parameters and are obtained by fitting experimental data. E_m is the internal specific energy per unit mass and ρ is the instantaneous density of the detonation products.

2.10 Summary of Literature Review

Polymer materials are a popular choice for the core material of many sandwich panels, due to their flexibility in design, low cost, corrosion resistance and high energy absorption per unit mass. Although, there are a wide variety of polymer materials, polyurethane foams are widely used as energy absorbers. The versatility of polyurethanes makes it a prime candidate for such applications. This study aims to use both thermoset polyurethane (TSPU) and thermoplastic polyurethane (TPU), as the core material of a sandwich structure.

Syntactic foams are a class of lightweight materials which are comprised of a matrix which are either metallic or polymer, with thin-walled hollow partices, i.e. microspheres or microbaloons. With advantages that include lower weight, lower cost for volume production and more freedom in design, the TSPU (casting resin) is the chosen material for the development of a syntactic foam consisting of hollow glass microspheres (HGMs). Currently there is a lack of results which utilise the polyurethane resin as a solid matrix medium reinforced with hollow spheres, rather than a gas filled expanded polyurethane foam. The aim is to decrease the density of the solid polyurethane whilst increasing the specific energy absorption (SEA) values of the TSPU with the use of HGMs.

Furthermore, to control the load during compression in energy absorbing structures, developments in the grading of the syntactic foams can be made, resulting in functionally graded foams (FGF). Graded structures enables researchers to optimise a materials response. These structures can offer many benefits, such as increased SEA values as well as reducing inertial effects under dynamic applications.

The introduction of tubular structures offer additional energy absorption without compromising the weight of the core material. The literature review suggests that many studies focus on metal tubes as a reinforcement for core materials.

However, carbon fibre reinforced polymer (CFRP) tubes reinforcement are showing promising results, due to the failure mechanisms associated with such materials. CFRP tubes offer themselves as a good reinforcement to be embedded in both the TSPU and TPU as a reinforcement, to further increase the SEA values under quasi-static and dynamic applications. These materials may be suited to a number of energy-absorbing structures, such as those employed in automobiles, aircraft and ships, where crash safety is of great importance.

In regards to computational modelling, there are a wide variety of constitutive models available in softwares such as ABAQUS. Researchers however, need to correctly determine the behaviour of materials, i.e. isotropic, anisotropic or orthotropic. Isotropic material modelling is generally preferred, since it limits the amount of experiments that need to be carried out to characterise a material. Furthermore, for composite materials such as CFRPs, there are a number of mathematical models available to simulate the behaviour of these, whilst there is also an option for a user defined model to be introduced for more accurate modelling. Finally, the literature survey suggests that there are several ways to model the blast loading onto a structure. However, it is suggested that converting the explosive loading regime to a pressure pulse loading, ensures low computational cost without compromising on accuracy, so long as the material properties are correctly validated.

Chapter 3

Experimental Methodology

This chapter presents the details of the manufacturing of the specimens and the experiments conducted during the course of this research study. A variety of mechanical testing and experimental techniques are used to investigate the energy-absorbing characteristics of graded and ungraded thermoset polyurethane (TSPU) syntactic foam as well as thermoplastic (TPU) samples. The first section of this chapter explains in detail, the manufacturing steps of processing the syntactic TSPU foams and the TPU. The experiments cover quasi-static, dynamic compression, perforation, and blast tests.

3.1 Manufacturing

TSPU, a highly cross-linked polymer, was manufactured using vacuum assisted resin transfer method (VARTM). The TSPU has two parts, the resin (Part A) - the formulated polyol was mixed with hollow glass microspheres (K20 series, $\phi = 30 - 115$ µm, $\rho = 0.2$ g/cc) [211] for several minutes to ensure that the microspheres were well distributed, after which the hardener (Part B) - the isocyanate - was added to the mixture. The mix ratio of both components was 100:100 g/g. The resin was transferred through a channel and into the 200 x 200 mm mould with a depth of 20 mm. However, prior to this a vacuum pump was attached to the outlets, to minimise the amount of trapped air and enabling the resin to flow into the mould by introducing a pressure difference. The design of this mould can be found in Appendix A. For illustration purposes, Figure 3.1 shows a fluid simulation carried out using $ANSYS$ [212], this simulation indicates the mechanisms of the VARTM that was employed for the manufacturing of the TSPU sample. The flow was set to laminar due to the Reynolds number (Re), Equation (3.1), being less than 2000.

$$Re = \frac{\rho u \phi}{\mu} \tag{3.1}$$

where ρ is the density of the fluid, u is the kinematic viscosity of the fluid, ϕ is the diameter of the inlets and μ is the viscosity of the fluid.

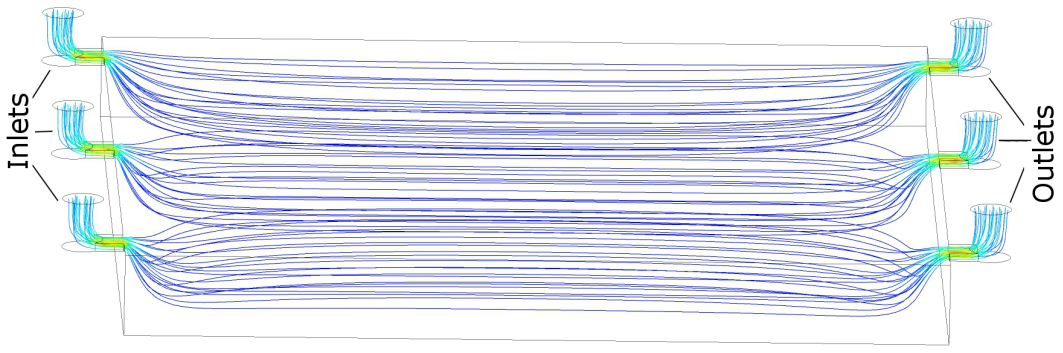

Figure 3.1: CFD simulation of the resin transfer process into the mould.

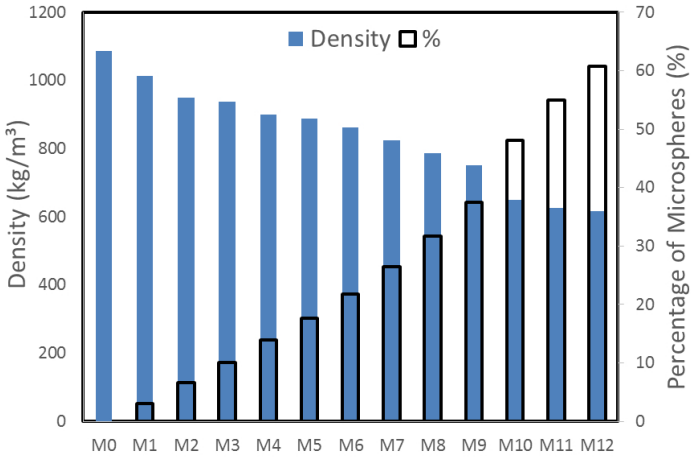

Figure 3.2: Variation of hollow glass microspheres (%, volume) and density (kg/m^3) of the syntactic TSPU.

Figure 3.2 shows the density variations of the syntactic TSPU as a function of the percentage of microspheres within the matrix. M0 is defined as the pure TSPU, without any microspheres and M1 - M12 refer to the syntactic TSPU with varying levels of density.

The volume fraction of the microspheres was calculated using the following equation,

$$\frac{W_{SF}}{V_{SF}} = \rho_{GM} \cdot (f_{GM}) + \rho_{PU} \cdot (1 - f_{GM}) \tag{3.2}$$

where W_{SF} and V_{SF} are the measured weight and volume of the syntactic foam. ρ_{GM} and ρ_{PU} represent the densities of the glass microspheres and the resin, respectively. The density of the TSPU resin is approximately 1087 kg/m^3. Rearranging Equation (3.2) provides the volume fraction of the microspheres (f_{GM}) as,

$$f_{GM} = \frac{\rho_{PU} - \rho_{SF}}{\rho_{PU} - \rho_{GM}} \tag{3.3}$$

where ρ_{SF} represents the density of the syntactic foam.

During the manufacturing process one cannot fully ensure the hollow micro-

Table 3.1: Physical properties of thermoset polyurethane [211].

Density (kg/m^3)	1050- 1100
Flexural Modulus (MPa)	800-1300
Shore Hardness	75-80
Elongation at break (%)	4-6
Tensile strength (MPa)	10-15
Flexural Strength (MPa)	30-40

Table 3.2: Technical specifications of micro-spheres (K-series) [211].

Technical Details K series	K20
Form	Free flowing powder
Particle size (µ)	30 -115
Elongation at break (%)	4-6
Colour	White
Isostatic Crush Strength (kPa)	≈ 3447
True density (g/cc)	20
pH of water dispersion	9.1 - 9.9

spheres are fracture free. Careful processing is advisable but may not completely eradicate this issue. Fracturing of the spheres would open up their cavity, which could subsequently be filled with the resin. Therefore, the volume fraction of microspheres can only be provided as an approximation. Further details of the TSPU and microspheres, as provided by the manufacturer, can be found in Tables 3.1 and 3.2, respectively.

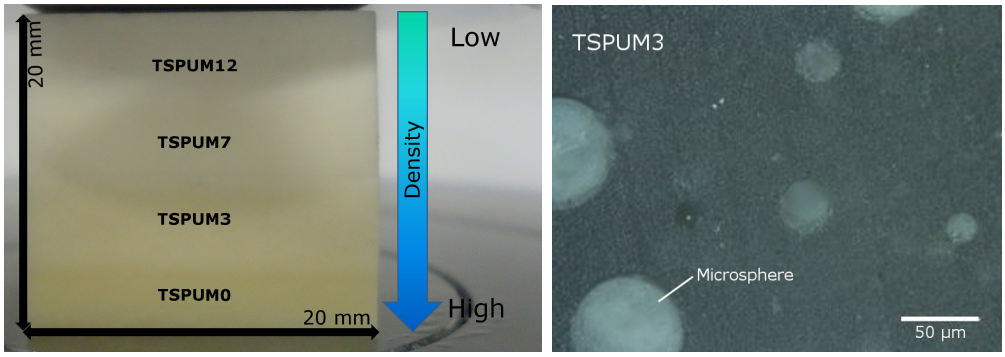

(a) TSPUG1 cross-section (b) Optical micrograph

Figure 3.3: (a) Example of the cross section of stepwise graded foam (TSPUG1), with density variation through-thickness and (b) optical micrograph of TSPUM3 illustrating the embedding of glass microspheres in the TSPU matrix.

Figure 3.19a presents an example (TSPUG1) of one of the graded foams used in this study, with a four-density variation at a 5 mm depth increment. Figure 3.3b shows an optical micrograph taken on the surface of the composite with a surface finish of approximately 5 µm, which illustrates the dispersion of the microspheres within the TSPU matrix. The investigation on the stepwise graded foams, i.e. G1 and G2, uses the different densities for the individual foams as detailed in Table 3.3.

Table 3.3: Density variation through the thickness of the graded TSPU specimens G1 and G2.

Thickness (mm)	G1	G2
0-5	M0 (1087 kg/m^3)	M0 (1087 kg/m^3)
5-10	M3 (937 kg/m^3)	M3 (937kg/m^3)
10-15	M7 (825 kg/m^3)	M7 (825 kg/m^3
15-20	M12 (617 kg/m^3)	

TPU is a linear segmented block copolymer consisting of hard and soft segments that can be moulded when heated before returning to a solid phase when cooled. Specimens based on the polyether grade TPU (Desmopan DP 9852 [213]) were used in this study and manufactured using a hot press. The TPU pellets were pre-dried at 110 °C for 3 hours and placed into a mould that was initially heated to 50 °C. In order to prevent the sample from sticking to the mould, a silicon based grease was applied on the interior surface of the 150 x 150 mm mould. A pressure of 350 kPa and a temperature of 220 °C were maintained for 25 minutes as illustrated in Figure 3.4. The specimen was then cooled at room temperature and removed from the mould when the temperature was below 50 °C. The specimens were then washed with distilled water, followed by washing with ethanol in order to minimise contamination. The TPU panels had a density of 1150 kg/m^3. In preperation for the blast tests aluminium alloy (AA) 2024-T3 skins (1.2 mm thickness) were bonded to the TPU core using a fast-curing contact adhesive (Timebond) to fabricate sandwich panels with three core thicknesses of,

5, 10 and 20 mm.

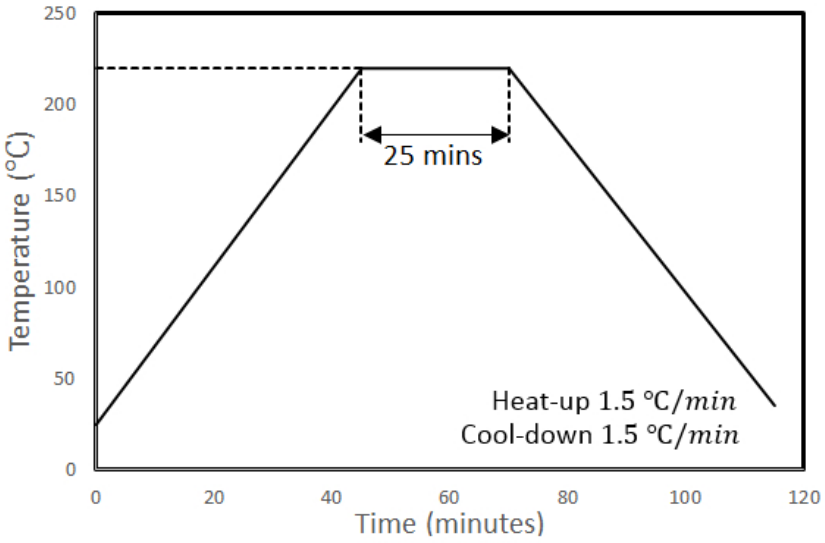

Figure 3.4: Curing temperature history for TPU.

For the reinforcement, T700 unidirectional carbon fibre (CF) tubes [211], with a density of 1600 kg/m^3 and an outer diameter of 10 mm (ϕ/t ratio = 6.3), were embedded within the TSPU and TPU matrices. More specifically, these tubes are 'roll wrapped' with a [90,0,90,0,90] configuration. The use of 'roll wrapped' tubes ensures that the tube has a favourable crush strength, providing maximum strength in the axial direction. This is in contrast to 'pultruded' tubes, which feature 100 % longitudinal fibre orientation, making them vulnerable to crushing forces in the axial direction.

A further study was carried out to analyse the effect of various chamfers on the CFRP tube with the use of single and double triggers with comparisons made against no trigger. Figure 3.5 illustrates the various chamfers that were investigated in this study. The chamfers were manufactured at 45°, where ChI refers to chamfers created on the inner diameter of the tubes and ChO on the outer diameter. In accordance with previous research [97], the use of chamfers, i.e. crush initiators, as a collapse trigger mechanism encourages suitable progressive crushing of the specimens. Chamfers were processed with the use of a Lathe and

a Dremel® tool with thread pins.

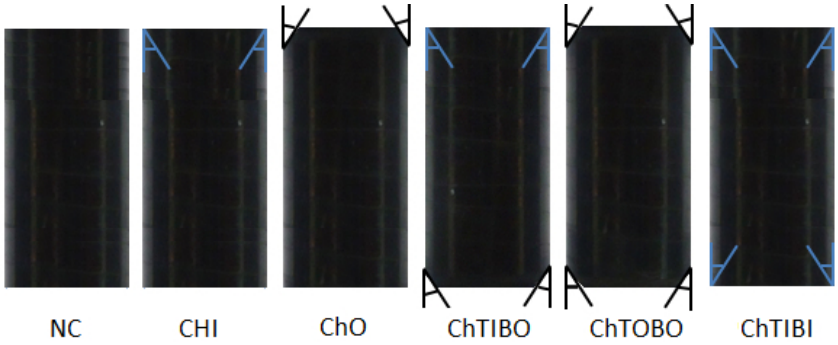

Figure 3.5: Various triggers used on the CFRP tubes. NC - No Trigger, ChI - 45° inner chamfer, ChO - 45° outer chamfer, T - Top, B - Bottom..

For the TSPU the CFRP tubes were embedded during the resin transfer process in a one-step process, ensuring a more uniform bonding between the tubes and the TSPU matrix. The embedding of the tubes within the TPU matrix was not as straightforward, this required an additional step of drilling 8 mm holes for the tubes to be inserted in the desired configuration. The arrangement of the tubes in the TSPU and TPU matrix is illustrated in Figure 3.6.

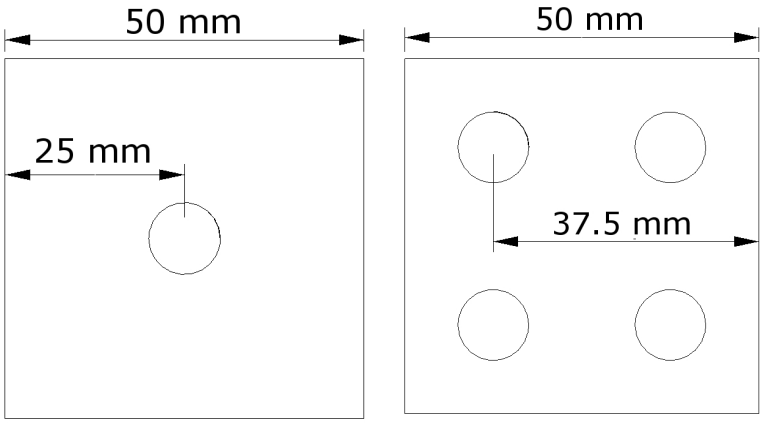

(a) One tube. (b) Four tube.

Figure 3.6: One and four CFRP tube configurations used with the TPU and TSPU matrices.

3.2 Mechanical Testing

3.2.1 Quasi-static testing procedure

Compression

Compression tests on the TPU and TSPU specimens were carried out on a 100 kN Instron *4505* universal servo hydraulic testing machine, as shown in Figure 3.7a. Tests were performed with loading axis orientated in the "through the thickness" direction. A 600 kN Instron *5989* (Figure 3.7b) was used to test the reinforced specimens. Standard laboratory conditions were 23 $\pm$2 °C with 30-40% relative humidity. For the quasi-static compression testing, the sample dimensions were 20 x 20 x 20 mm. In order to minimise friction between the platen and the specimens, both platens were greased. The cross-head displacement rate was set to 1 mm/min and at least three repeated tests were conducted for each material.

(a) 100 kN Instron 4505 universal testing machine.

(b) 600kN Instron 5989 universal testing machine.

Figure 3.7: Photographs of *INSTRON 4505* (a) and *INSTRON 5989* (b) universal testing machines

The specific energy absorption, E_s, is defined as,

$$E_s = \frac{(\int_0^{\epsilon_d} \sigma \cdot d\epsilon)}{\rho} \tag{3.4}$$

where ϵ_d is the densification strain and ρ is the density of the sample.

Tensile

Tensile tests were conducted on the TPU specimens in accordance with ASTM D638 (type V) using dog-bone shaped specimens (gauge length - 9.5 mm, width - 3.2 mm, thickness - 3 mm). In order to evaluate the strain rate sensitivity of the TPU specimens, tests were carried out at cross-head displacement rates of 1,10 and 100 mm/min. A comparison against aluminium alloy (AA) 2024-T3 is made where tensile specimens were in accordance with ASTM E8/E8M (subsize specimen), with a thickness of 1.2 mm. The TPU was tested at three different orientations (0°, 45° and 90°), which were manufactured from a single TPU panel as shown in Figure 3.8, in order to determine whether there is any possible material anisotropy.

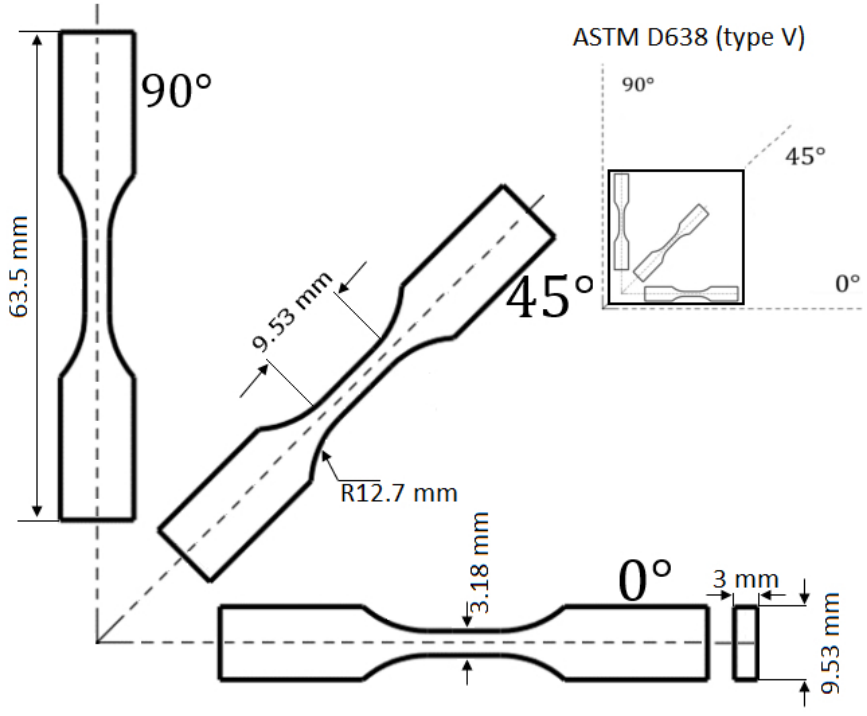

Figure 3.8: Geometry of tensile specimens (ASTM D638 - type V)

An extensometer was used to measure the initial extension of the TPU sample, as shown in Figure 3.9. The experimental method used for the tensile experiments does not take into account local measurements of true stress, true strain and true

strain-rate after the onset of necking. Therefore, nominal stress, strain and strain-rate were used to characterise the overall response of the TPU and AA 2024-T3 specimens under tension and later converted to true stress-strain using Equations (3.5) and (3.6).

$$\sigma_{True} = \sigma_{Nominal}(1 + \epsilon_{Nominal}) \tag{3.5}$$

$$\epsilon_{True} = ln(1 + \epsilon_{Nominal}) \tag{3.6}$$

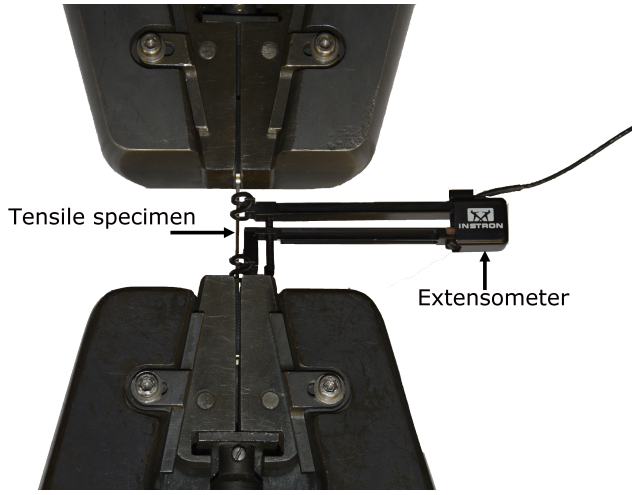

Figure 3.9: Tensile set-up with clip-on extensometer.

3.2.2 Dynamic testing

Dynamic compression tests are required in order to investigate the influence of low, intermediate and high strain rates on the mechanical properties of the specimens. Low velocity impact (LVI) tests are carried out in order to investigate the dynamic response of the samples with various impact energies and velocities. Further investigation is carried out with the use of a split-Hopkinson pressure bar (SHPB) also know as a Kolsky bar, which is used for the evaluation of high strain-rate effects in materials. Finally, blast tests are carried out in order to ob-

serve the 'real life' response of the sandwich panels under explosive shock loading conditions.

Low velocity compression impact testing

The purpose of the drop-hammer tests was to investigate the influence of higher energies on the mechanical properties of the specimens, this was carried out with the use of the instrumented drop hammer impact tower. Instrumented drop-hammer tests were also undertaken to investigate the influence of a higher strain rate on the mechanical properties of the specimens. A drop mass of 25.6 kg was used for the lower energies (64 - 276 J) for the samples without tube reinforcements.

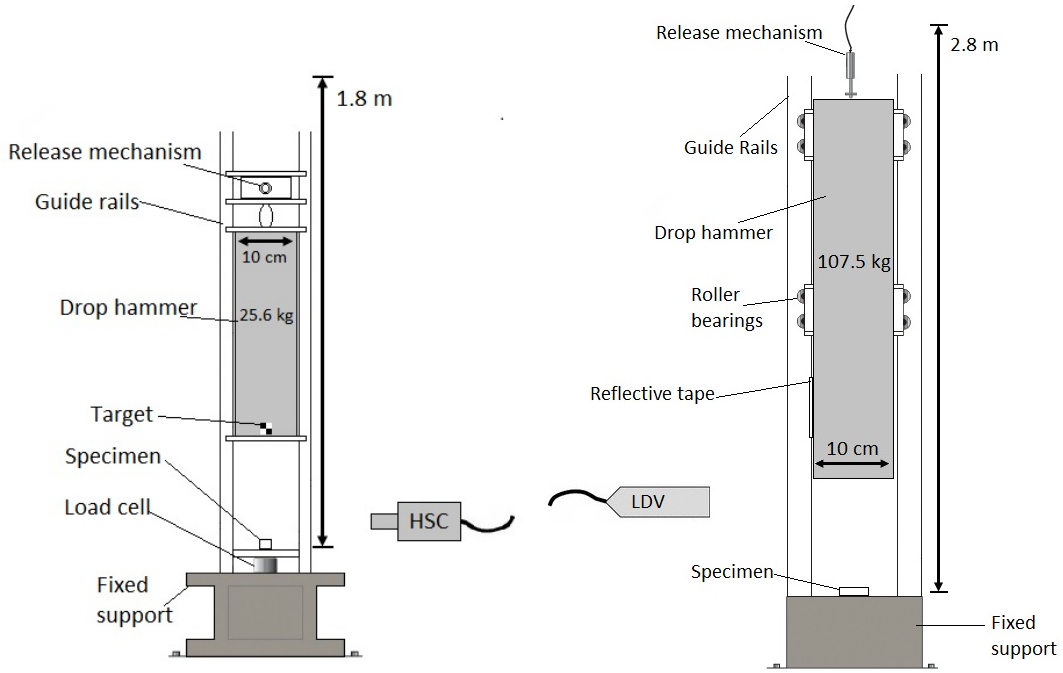

(a) HSC (b) LDV

Figure 3.10: High speed camera (HSC) impact rig set up for unreinforced samples (a) and laser Doppler velocimeter (LDV) impact rig set up for tube reinforced samples (b).

The variation of load with time was measured with the use of a Kistler piezoelectric load cell (maximum capacity = 120 kN), located between the carriage and the flat impactor, as shown in Figure 3.10a. Loading data was acquired

as voltage output and transferred into a module 64K Data Acquisition Station (DAS) at a frequency of 100 kHz. A High Speed Camera (HSC) was used to measure displacement and velocity. For the reinforced samples, an impact rig set up with a drop weight mass of 107.5 kg was used, as shown in Figure 3.10b, which provided higher impact energies (360 - 2046 J). The variation of velocity and time was measured using a Dantec Flowlite laser Doppler velocimeter (LDV) system [214], to obtain load and displacement data.

The LDV was used in order to measure the velocity of the impactor as well as the contact force and deformation of the samples. LDV is a non-contacting instrument which does not directly influence the system or become influenced by it [214]. In contrast to instrumentations such as load cells, the magnitude of the contact force is not limited to the capacity of the instrumentation.

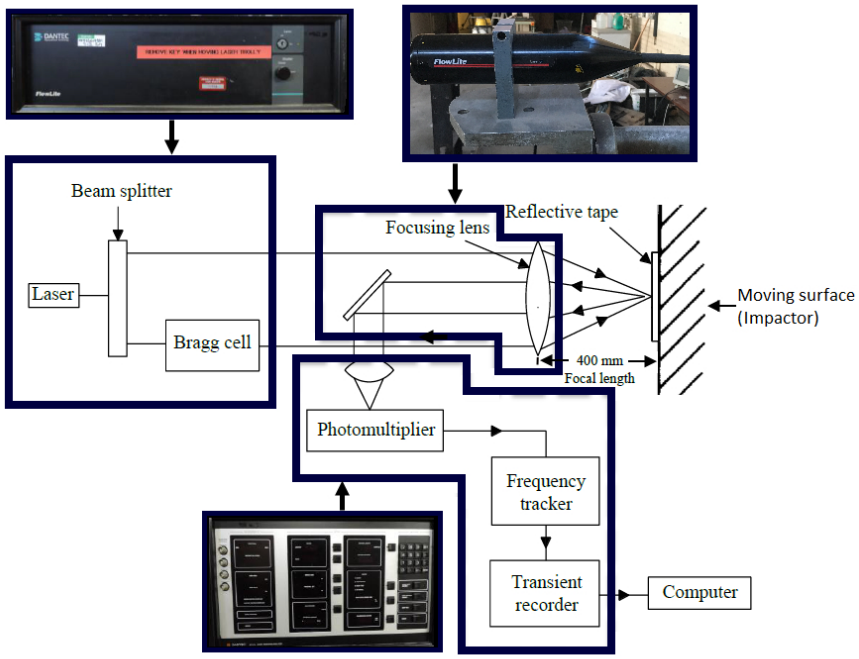

Figure 3.11: Schematic arrangement of laser Doppler velocimeter (LDV) [214].

The schematic set up of the LDV system as illustrated in Figure 3.11, consists of a laser system (two beams, red colour Helium-Neon laser, continuous wave with 632 nm wavelength), Bragg Cell (shifting the frequency of laser beam), Optic

Table 3.4: General setting of the Burst Spectrum Analyser (BSA).

Context	Parameter	Value	Units
BSA Range/Gain	Velocity Range - Centre	3.31	m/s
	Velocity Range - Span	13.2	m/s
	Record Length	16	-
	High Voltage	848	V
	Signal Gain	35	dB
	Calibration		m/s
BSA Data Collection/Buffering	Data Collection Mode	Continuous	-
	Output Buffer Mode	Burst	-
	Number of Burst	100,000	-
	Measurement Intervals	10	S
	Validation Level	0	-
	Dead Time	0	ms
	Duty Cycle	100	%

unit (transmitting and receiving optics) with lenses, Fibre-optic cable and Burst Spectrum Analyser (BSA) enhanced signal processor, model 57N21, which was linked to a computer via an interface card, optic unit and a fibre optic cable. Two laser beams were focused together via a lens on the optic unit. A 25 mm width by 200 mm long high intensity reflective tape was placed on the surface of the impactor, this is due to the backscatter-type LDV requiring some reflected beams impinging the impactor to be collected at the same lens for further processing. The focal length from the lenses to the reflective tape was set at 400 mm. A computer was linked to the BSA via an interface card and setting of the BSA prior to the impact test was performed using BSA Flow software. The general settings for the BSA is provided in Table 3.4.

The flow chart illustrating the steps of the filtering process of the LDV raw data is presented in Figure 3.12. The full LDV raw data, an example of which is shown in Figure 3.13a, was reduced manually to within the regions of the contact and rebound of the impactor and sample, as shown in Figure 3.13b. Linear interpolation of the reduced data set was carried out using Impression 6.0 software (Nicolet Instrument Technologies Inc.) in order to obtain an equal time

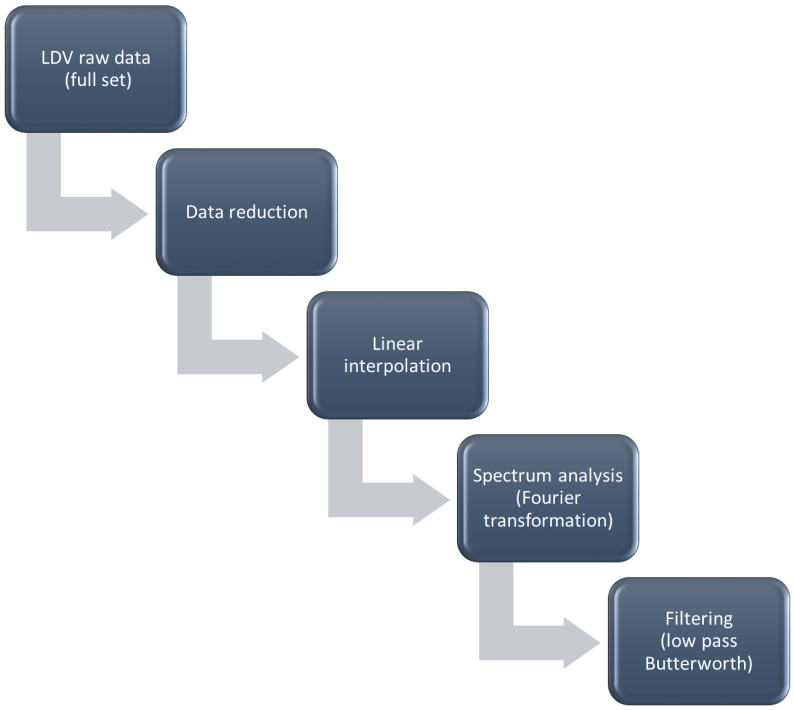

Figure 3.12: Flowchart illustrating the steps of the filtering process for the LDV raw data.

step. Spectrum analysis was then carried out using Fourier transformation in order to transform velocity data in the time domain into the frequency domain. Any indications of possible noise sources and estimation of the cut-off frequency was investigated at this point. Finally, the reduced data was filtered using the Fourth Order Low Pass Butterworth Filter.

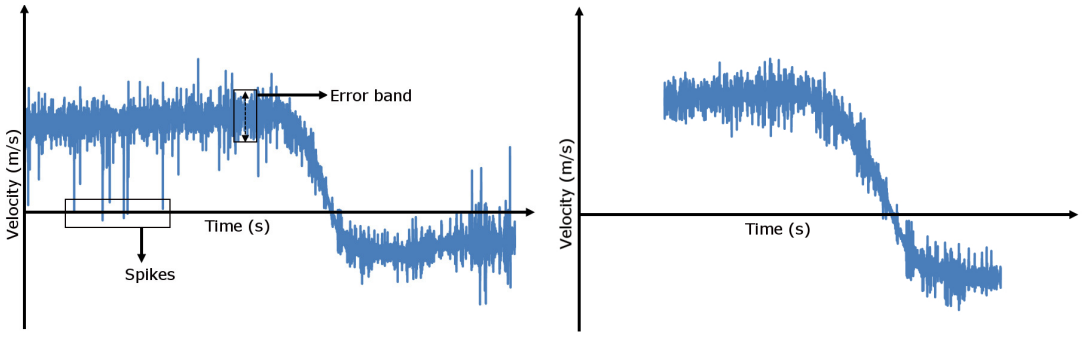

(a) Full raw data (b) Reduced raw data

Figure 3.13: Typical velocity-time raw data from LDV showing full raw data (a) and reduced data (b).

A single differentiation of the velocity-time history from the filtered LDV data was carried out in order to determine the acceleration-time history, from this one can determine the contact force. The accuracy of the acceleration history is obtainable by recording a large number of data during short duration impact events [215]. Statistically it is known that with larger sampling data, the degree of variability in the recorded data becomes less and therefore the larger sampling provides negligible effects when subject to linear interpolation. Subsequently, the entire filtering process would have negligible variations in the recorded velocity-time data and therefore the derivation of acceleration-time and force-time using the equation of motion is justifiable.

It is noteworthy to mention, that Birch and Jones [214] showed that the peak force derived from LDV data possessed strong similarity compared to the direct measurement from a load cell when filtered using the same cut-off frequency of 1000 Hz. Nevertheless, accurate determination of the peak forces are difficult to measure under dynamic conditions with high-magnitude and short duration loading, regardless of the type of devices being used, due to the presence of reflected stress waves and vibrations in the system that may contribure to a false peak. Therefore, this phenomenon provides some limitations to the investigation for determining the true peak force during an impact event. As the force-time history is dependent on the velocity-time raw data, the accuracy is determined with the size of the data set and the continuity between each data especially in an impact event. The impact set-up was modified using Polytetrafluoroethylene (PTFE) roller bearings to minimise the amount of lateral vibrations, limiting the loss of any data or large gaps in the time step between each data which may affect the slope of the velocity-time history, since the movement of the impactor/target normal to the lens has a significant effect on the frequency shift of the reflected beams.

Low velocity perforation testing

In order to assess the competitiveness of TPU, a further investigation was carried out to compare the TPU with AA 2024-T3 under perforation. This test was carried out to observe the impact behaviour of both specimens under projectile loading, as shown in Figure 3.14.

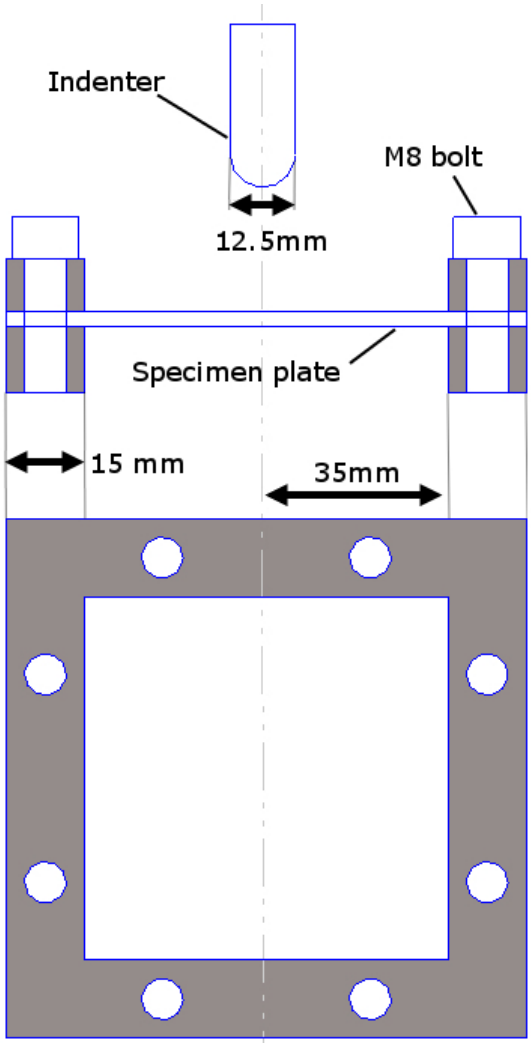

Figure 3.14: Schematic of the perforation test set-up.

The test specimens used for the impact perforation were based on flat plates (100 x 100 mm) with a square test area (70 x 70 mm), these were cut to size from the 150 x 150 mm samples. The thickness of the TPU sample was 2.9 mm with a density of 1150 kg/m^3 and for the AA 2043-T3 specimens a thickness of 1.2

mm with a density of 2750 kg/m^3 was used, giving the targets approximately the same mass per unit area for these two types. An axisymmetric indenter with a hemi-spherical nose shape (ϕ - 12.5 mm) was used for the investigation. Projectile impact tests with a mass of 3.44 kg were carried out with a height of 1.2 m (4.85 m/s), giving a constant impact energy of 40.5 J.

Split-Hopkinson pressure bar (SHPB) testing

In order to determine the strain-rate sensitivity of the syntactic TSPU and TPU materials, it is necessary to characterise these using high strain-rate compression testing. Tests were performed on a split-Hopkinson pressure bar (SHPB) apparatus at Nanjing University of Science and Technology, PR China. The SHPB tests are used for measuring the dynamic stress-strain response of the materials at strain rates that are usually associated with ballistic or blast loading conditions.

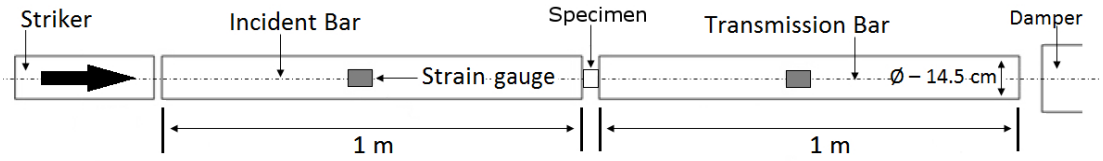

Figure 3.15: Schematic of the compression SHPB test set-up.

Figure 3.15 shows a schematic illustration of the SHPB test set-up. Solid aluminium (7A04 T6) pressure incident and transmission bars were used, both of which have a length of 1 m and a diameter of 14.5 mm. The cylindrical specimens used for these tests had a thickness-to-diameter ratio of 1:1, with 8, 6 and 4 mm thicknesses being used in accordance with the strain-rate requirements. A shorter specimen length was necessary in order to generate a uni-axial stress state during pulse transmission.

Furthermore, in order to obtain a homogenous deformation state, a thin layer of petroleum jelly was applied on both sides of the specimen and the end faces of the incident bar and the transmission bar to lubricate the contact surfaces.

A pulse-shaping technique was also employed to ensure a constant strain-rate, smoothing the stress pulse, eliminating the high frequency oscillations in the incident pulse and extending the pulse duration in order to achieve stress equilibrium [216].

A digital oscilloscope with a 50 x 10^6 s^{-1} sampling rate capacity was used, to collect the test data. A set of high precision strain gauges were used in addition to the signal conditioners and high speed digital oscilloscopes with high sensitivity and accuracy. The properties of the bar material are used to determine the sensitivity of the pressure bar such as the elastic wave impedance and the density [217].

The principle of the SHPB set up is based on two basic assumptions, that is the one-dimensional (1D) wave propagation theory and even stress assumption. The 1D assumption is that stress wave propagation in a uniform, homogeneous bar at each cross section always remains in a constant state; uniform stress is repeatedly assumed and the transmitted and reflected wave propagation in the specimen results in an equal stress distribution. In order to meet the two assumptions, the impact striker, incident bar and transmission bar must possess a higher Young's Modulus (E_Y) than the material being tested. This requirement is to ensure that the stress wave in these rods are within the elastic region. Secondly, it is necessary to ensure the specimens being tested are polished during processing to ensure a parallel top and bottom face, to ensure a uni-axial stress state during pulse transmission.

Figure 3.16 provides a schematic of the experimental load process. $\epsilon_I(t)$, $\epsilon_R(t)$ and $\epsilon_T(t)$, are the incident, reflected and transmitted strains measured from the strain gauges, respectively. U_1 and U_2 are the two contact faces of the bars on the specimens with a length, L_S.

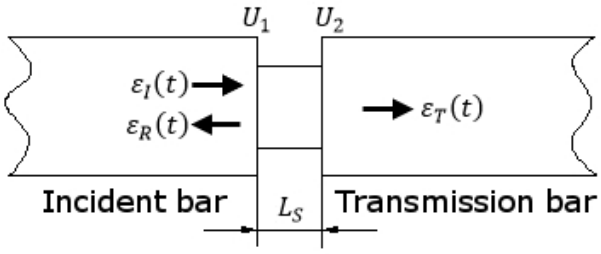

Figure 3.16: Schematic of the SHPB experimental load process.

According to the 1D wave propagation theory,

$$u_1 = \int C_0 \epsilon_1(t) dt \tag{3.7}$$

$$u_2 = \int C_0 \epsilon_2(t) dt \tag{3.8}$$

where u_1 and u_2 are the displacements of the top and bottom faces of the specimen and C_0 the wave velocity. Subsequently, the surface strain for the two of the specimens are given as,

$$\epsilon_1(t) = \epsilon_I(t) - \epsilon_R(t) \tag{3.9}$$

$$\epsilon_2(t) = \epsilon_T(t) \tag{3.10}$$

where, ϵ_I, ϵ_R and ϵ_T are the incident, reflected and transmitted strains, respectively. The mean strain (ϵ_m) of the specimens is then determined using the following equation,

$$\epsilon_m(t) = \frac{(u_1 - u_2)}{L_S} = \frac{C_0}{L_S} \int \big[(\epsilon_I(t) - \epsilon_R(t) - \epsilon_T(t))\big] dt \tag{3.11}$$

Similarly, by using the 1D elastic wave theory,

$$P_1(t) = E_Y A_B [\epsilon_I(t) + \epsilon_R(t)] \tag{3.12}$$

$$P_2(t) = E_Y A_B \epsilon_T(t) \tag{3.13}$$

where, P_1 and P_2 are the surface loads whilst A_B is given as the cross-sectional area of the bar. The mean stress (σ_m) can therefore be determined using the following equation,

$$\sigma_m(t) = \frac{(P_1(t) - P_2(t))}{A_s} = \frac{E_Y A_B}{A_S}\big[(\epsilon_I(t) - \epsilon_R(t) - \epsilon_T(t))\big] \tag{3.14}$$

where A_S is given as the cross-sectional area of the specimen. A summary of the mean stress, average strains and average strain rates are as follows:

$$\begin{cases} \epsilon_m = \frac{2C_0}{L_S}\int_0^t \epsilon_R(t)dt \\ \sigma_m(t) = \frac{E_Y A_B}{A_S}\epsilon_T(t) \\ \dot{\epsilon}_m = \frac{2C_0}{L_S}\epsilon_R(t) \end{cases} \tag{3.15}$$

The incident, reflected and transmitted waves are collected in this experiment. Therefore the formula for calculating the stress-strain curve is as follows:

$$\begin{cases} \epsilon_m = \frac{C_0}{L_S}\int_0^t (\epsilon_I(t) - \epsilon_R(t) - \epsilon_T(t))dt \\ \sigma_m(t) = \frac{EA_B}{A_S}(\epsilon_I(t) + \epsilon_R(t) + \epsilon_T(t))dt \\ \dot{\epsilon}_m = \frac{C_0}{L_S}(\epsilon_I(t) + \epsilon_R(t) - \epsilon_T(t))dt \end{cases} \tag{3.16}$$

With the use of the known 1D wave propagation theory, the incident wave and reflected signal is equal to the transmitted signal. In the handling of the wave form curve, the data of the first three waves are used in the processing formula, Equation (3.16), to obtain the materials' stress vs. strain or strain rate vs. strain traces.

This study employs Matlab data processing software using a PXI (PCI eXtensions for Instrumentation) platform. PXI is a modular instrumentation platform that is used for measurement and automation applications. The data process-

ing includes several steps as shown in Figure 3.17. The process effectively deals with the incident, reflected and transimitted waves forms, in which the signal is in the form of voltage and time. Matlab is used to convert the data into the required stress vs. strain and strain rate vs. strain curves. The code used for the conversion of the SHPB data can be found in Appendix B.

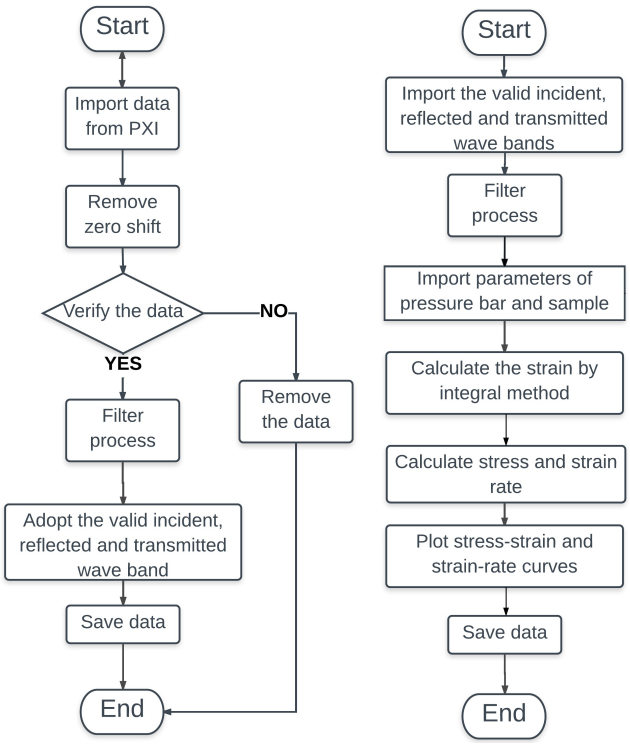

(a) Waveform (b) Stress-strain

Figure 3.17: Waveform (a) and stress-strain (b) curve extraction process flowchart.

3.2.3 Blast tests

The investigation into the structural response of TPU panels, subjected to uniform blast loading was investigated with the use of PE4 explosives, the properties of which are given in Table 3.5. The work was then extended to investigate the response of sandwich panels with AA 2024-T3 as the skins and TPU as the interlayer, with varying thicknesses. Impulsive loads were increased to yield Mode I

(large inelastic deformation), Mode II* (partial tearing along the boundary) and Mode II (tensile tearing around the full boundary) failure modes [21].

Table 3.5: Properties of PE4.

Velocity of Detonation	7500 m/s
Density	1.6 g/cm^3
Composition	88 % RDX
	11 % Wax Plasticiser
	1 % Pentaerythritol diolate

The blast tests were carried out on a ballistic pendulum at the University of Cape Town, South Africa. In preperation for testing, four 12 mm diameter holes were drilled into the specimens to facilitate their positioning on the rig. A limited number of tests were carried out on TPU samples with and without skins, Table 3.6 provides a description of the specimens tested under blast loading.

Table 3.6: Description of blast test specimens.

Series	Description
A	5 mm TPU core (no skins)
B	5 mm TPU core with 1.2 mm 2024-T3 skins Average thickness 7.75 mm
C	10 mm TPU core with 1.2 mm 2024-T3 skins Average thickness 12.50 mm
D	20 mm TPU core with 1.2 mm 2024-T3 skins Average thickness 22.60 mm
E, F	10, 20 mm TPU cores with CFRP tubes (NC) and 1.2 mm 2024-T3 skins Average thickness 12.97, 22.28 mm

The samples were bolted to the test set-up to provide a clamped boundary condition. The 150 x 150 mm panels were clamped between two steel frames, giving an exposed circular area with a diameter of 90 mm. Blast loading was applied by detonating a circular PE4 disk at a 90 mm stand-off distance (SOD). The PE4 plastic explosive was shaped into a cylindrical geometry, as described by Nurick *et al.* [218]. The charge was placed onto a 14 mm thick polystyrene foam pad that was centrally located on the circular exposed area. The electrical

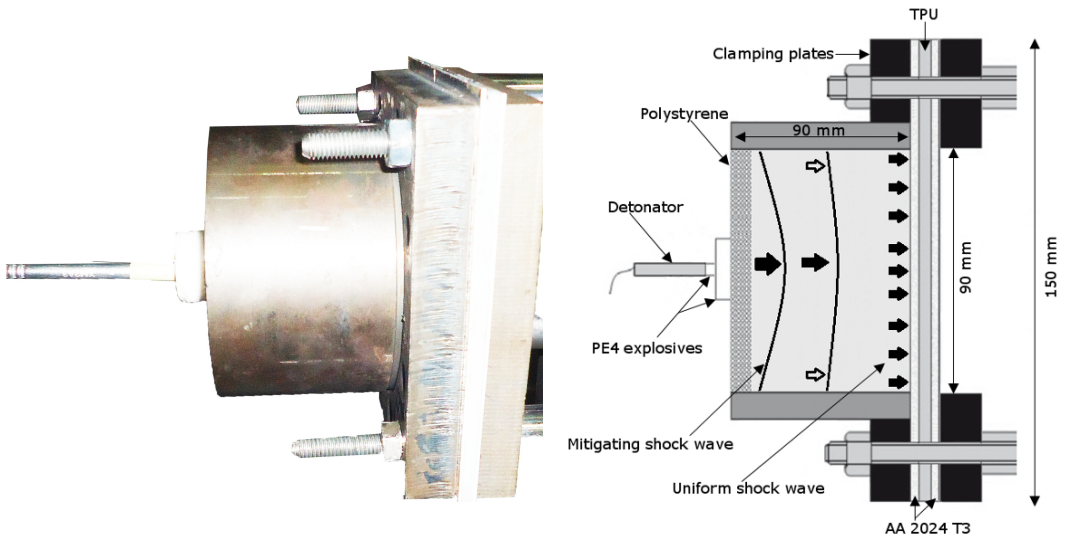

(a) Photograph (b) Schematic

Figure 3.18: Photograph and schematic of the air-blast test arrangement.

detonator was then attached to the center of the PE4 disk using one gram of additional explosive, known as a "leader". In order to direct the blast wave towards the sample, an open-ended transmission tube was bolted to the front clamping frame and the explosive was positioned at the open end, as shown in Figure 3.18.

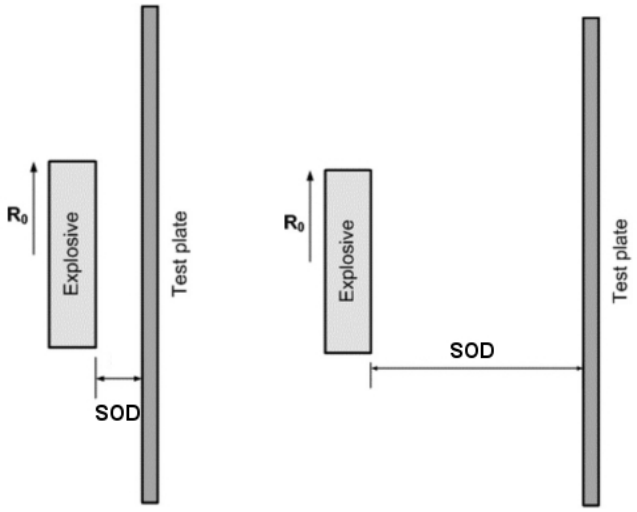

(a) $SOD < R_0$ (b) $SOD \geq R_0$

Figure 3.19: Diagram of explosive stand-off distance (SOD) and assumed loading conditions, i.e. uniform or localised loading [219].

Uniformity of the blast load on the target plate was assumed by employing the stand-off distance (SOD) greater than or equal to the radius (R_0) of the plate [219], as illustrated in Figure 3.19. In the case of a circular target, if the SOD is less than the radius of the target plate, the plate is subjected to localised loading. Whereas, if the SOD is larger than the radius of the target panels, then the blast load can be assumed to act uniformly [219].

Impulse generated from blast loading on the ballistic pendulum is calculated using the natural period of the system and results captured from the loading scenario. Figure 3.20 is a schematic representation of the ballistic pendulum and the associated geometry of the system. A laser displacement sensor (LDS) was connected to an oscilliscope, in order to calculate the displacement from the oscillations generated from the blast loading. The dashed lines indicate the position of the pendulum in maximum forward (blue) and backward (red) position due to a blast load. This generates a sine wave output for the oscilliscope reading, a typical example of which is shown in Figure 3.21.

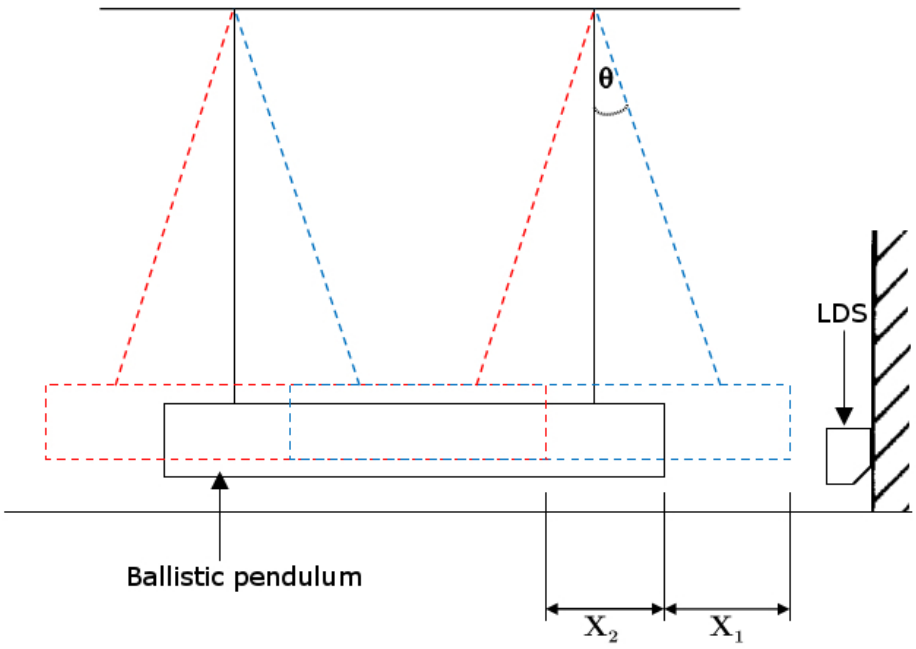

Figure 3.20: Schematic of the ballistic pendulum.

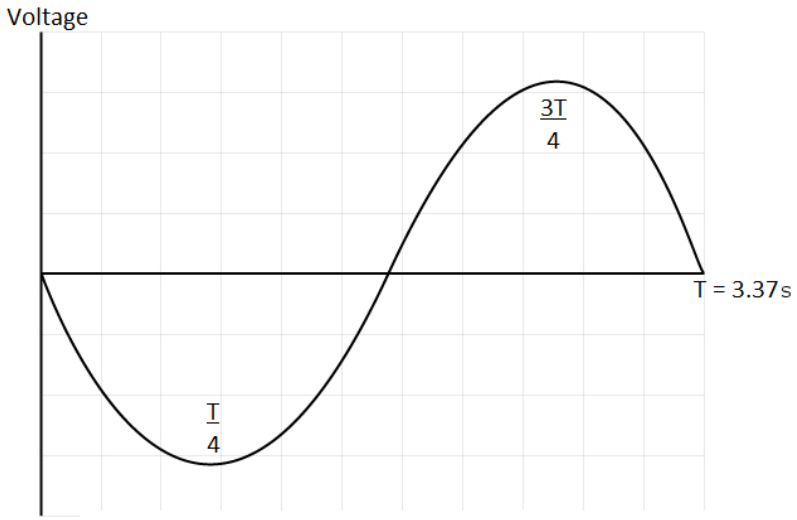

Figure 3.21: Sine wave output from oscilliscope.

The linearised equation of motion representing the ballistic pendulum is given by,

$$\ddot{X} + 2\beta\dot{X} + {\omega_n}^2 = 0 \tag{3.17}$$

where,

$$\beta = \frac{C}{2M} \tag{3.18}$$

$$\omega_n = \frac{2\pi}{T} \tag{3.19}$$

The constants C, M and T are defined as the viscous damping coefficient, total mass of the pendulum (including test rig, specimen and counterbalance masses) and the natural period of the pendulum, respectively.

The solution of Equation (3.17) is presented as,

$$X = \frac{e^{-\beta t}\dot{X}_0 sin(\omega_d t)}{\omega_d} \tag{3.20}$$

where $\dot{X}_0$ is the initial velocity of the pendulum, and

$$\omega_d = \sqrt{{\omega_n}^2 - \beta^2} \tag{3.21}$$

where ω_n is the natural frequency of the oscillation and ω_d actual frequency of the oscillation. By letting X_1 the maximum forward displacement of the pendulum at time $t = \frac{T}{4}$, and similarly X_2 the maximum backward displacement of the pendulum at time $t = \frac{3T}{4}$. Substituting X_1, X_2 and their corresponding time values into Equation (3.20) gives,

$$X_1 = \frac{\dot{X}_0 T e^{-\beta\frac{T}{4}}}{2\pi} \tag{3.22}$$

$$X_2 = -\frac{\dot{X}_0 T e^{-\beta\frac{3T}{4}}}{2\pi} \tag{3.23}$$

Using Equations (3.22) and (3.23), β can be solved for,

$$\beta = \frac{2}{T} ln\left(\frac{X_1}{X_2}\right) \tag{3.24}$$

Substituting Equations (3.24) into Equation (3.22), the initial pendulum velocity can be determined using the following equation,

$$\dot{X}_0 = \frac{2\pi}{T} X_1 e^{\beta\frac{T}{4}} \tag{3.25}$$

The impulse can therefore be found as,

$$I = M\dot{X}_0 \tag{3.26}$$

The natural period of the pendulum (T) was found by manually displacing the pendulum and releasing it in order to capture the time taken for a number of oscillations (typically 15), which was then averaged in order to establish the time taken for one oscillation.

3.3 Summary of Experimental Methodology

The details of the manufacturing of the specimens and experimental procedures for the characterisation of the material properties, i.e. quasi-static and dynamic tests, have been presented. The materials that are investigated include the TPU and TSPU, with modifications made to the TSPU using hollow glass microspheres (HGMs), leading to the development of a syntactic foam and from this a graded structure. Tests were also carried out on an aluminium alloy (AA) 2024-T3 for comparison against the TPU and also as applications of the skins on the TPU sandwich structure under blast loading. The mechanical properties of the materials were characterised using quasi-static tests, i.e. compression (TSPU and TPU) and tensile (TPU and AA 2024-T3). Dynamic tests consist of low velocity impact and perforation, split-Hopkinsons pressure bar (SHPB) and blast tests.

Chapter 4

Experimental Results and Discussion

This chapter presents the experimental results obtained and a discussion. Firstly, the mechanical response of the syntactic thermoset polyurethane (TSPU) and the thermoplastic polyurethane (TPU) under quasi-static loading conditions will be presented, with further observation made for reinforcing these materials with carbon fibre reinforced polymer (CFRP) tubes. Secondly, the dynamic response of the aforementioned materials (unreinforced/reinforced) under low velocity impact (LVI) will also be presented, with an extension to investigate the perforation resistance of TPU in comparison to an aluminium alloy (AA 2024-T3). Further investigations of the syntactic TSPU and TPU under high strain-rate loading conditions with the use of a split-Hopkinson pressure bar (SHPB). Finally, the blast response of the TPU in a sandwich structure configuration with the TPU as the core and AA 2024-T3 skins is also investigated and discussed.

4.1 Results and Discussion

4.1.1 Quasi-static compression results

This section covers the quasi-static experimental results obtained for the syntactic TSPU and TPU. Tests are also performed on carbon fibre reinforced polymer (CFRP) tubes with various chamfers to analyse the effect the chamfers have on the physical response of the crushing of the tubes and any improvements in energy absorption. Reinforcing the TSPU and TPU matrices with the CFRP tubes is also analysed.

Unreinforced syntactic TSPU

The energy absorption of the syntactic TSPU specimens (details can be found in Figure 3.2) loaded in quasi-static compression were calculated up to the onset of densification. Figure 4.1 presents the energy absorbed and energy absorbed per unit mass (SEA, E_s) for the TSPU samples with densities ranging from 617 to 1087 kg/m^3. Evidence presented in Figure 4.1 shows that SEA can be increased slightly throughout the various densities. The highest value was observed at 937 kg/m^3, for the syntactic foam M3.

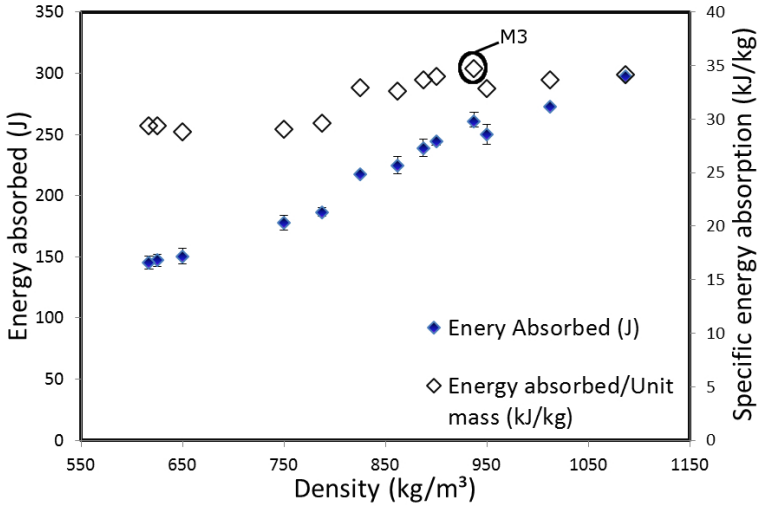

Figure 4.1: Energy absorbed and specific energy absorbed for TSPU (M0-M12).

Figure 4.2 shows typical stress-strain curves following the compression tests on the TSPU foams (M0, M3, M7 and M12), where it is evident that the plateau regions are extended slightly due to the collapsing of the microspheres inside the syntactic TSPU. The empty cells which are introduced by the hollow microspheres reduce the strength of the syntactic foam by weakening the matrix via the introduction of stress concentrations.

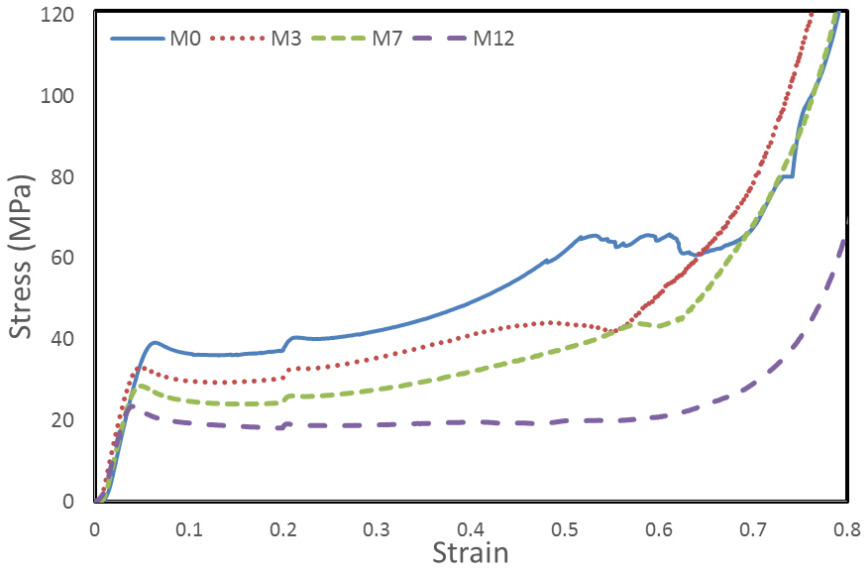

Figure 4.2: Stress-strain curves for TSPU M0, M3, M7 and M12 under quasi-static loading.

The deformation mechanisms are presented in Figure 4.3 for the non-syntactic TSPU M0, syntactic M12 and graded structure G1, where it can be seen that M0 exhibits a more ductile failure, whereas M12, which is dominated by shear bands, experiences a more brittle failure. The graded foam attempts to combine the characteristics of the individual foams, via an incrementally-graded thickness profile as described in Table 3.3. G1 demonstrates a more progressive failure mode which can be a benefit under dynamic loading, whereby the foremost layer offer both high energy absorption characteristics and dampening properties, whereas the rearmost layer offers a higher compressive stiffness.

(a) $\epsilon = 25\%$ (b) $\epsilon = 50\%$ (c) $\epsilon = 25\%$ (d) $\epsilon = 50\%$

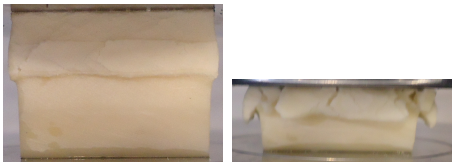

(e) $\epsilon = 25\%$ (f) $\epsilon = 50\%$

Figure 4.3: Photographs of the collapse mechanisms of M0 (a,b), M12 (c,d) and G1 (e,f) under quasi-static loading.

CFRP tubes with chamfers

Figure 4.4 provides a typical response of the CFRP tubes with various chamfers as shown in Figure 3.5. It is observed that no trigger provides a much higher peak response in comparison to the tubes with single/double triggers. The triggers in this instance provide a much more favourable progressive-like response, which is ideal for impact situations, where inertial effects are an important consideration.

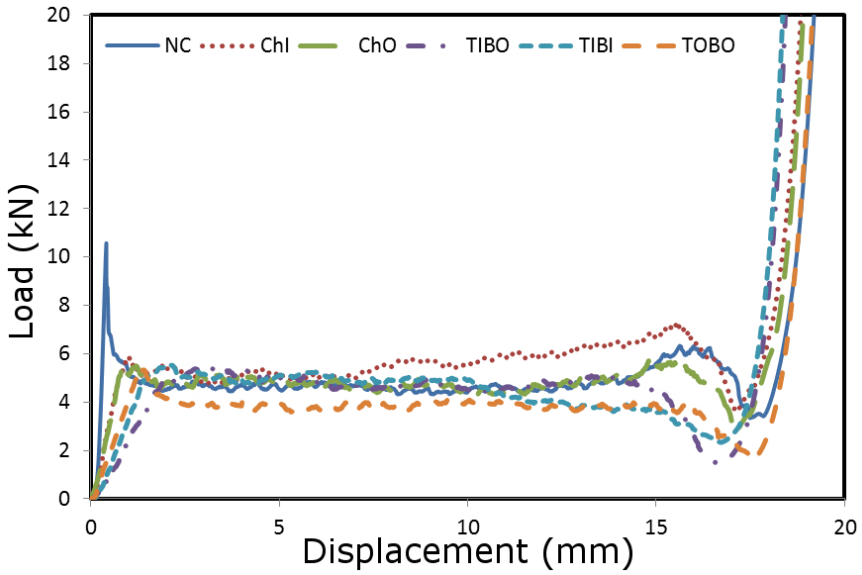

Figure 4.4: Quasi-static response of CFRP tubes with various chamfers.

Table 4.1 presents the peak stress and SEA (E_s) of CFRP tubes with 45° chamfers for single and double triggers with comparisons being made against no

trigger. It was shown that the highest SEA was given by a single trigger located on the inner diameter of the tube, i.e. ChI, with a percentage increase of 8.1% relative to the tube with no chamfers, i.e. NC.

Table 4.1: CFRP tubes under quasi-static compression with with various chamfers providing yield stress (σ_y) and specific energy absorption (E_s).

ID*	σ_y (MPa)	E_s (kJ/kg)
NC	1.68	91.0
ChI	0.92	98.7
ChO	0.87	84.6
TIBO	7.99	75.6
TIBI	0.793	76.4
TOBO	0.846	67.3

*ID; NC (No chamfer), ChI (45° Inner chamfer), ChO (45° Outer chamfer), T (Top), B (Bottom)

CFRP tube reinforced TSPU and TPU

With the introduction of CFRP tube reinforcements, one can observe that the stress-strain curves, displayed in Figure 4.5, clearly exhibit a significant improvement in the compressive strength of both TSPU and the TPU systems. For example, the stress-strain plot for the unreinforced TPU did not clearly indicate a yield point, the addition of tubes help in improving the stiffness of the TPU under quasi-static loading conditions by providing a higher peak stress.

Figure 4.6 presents the SEA and plateau stresses at 25 and 50 % for the unreinforced and reinforced syntactic TSPU foams under quasi-static loading conditions. The addition of CFRP tubes can significantly improve the energy absorbing characteristics of the TSPU and TPU under quasi-static loading conditions. The addition of a single tube (T1) increases the SEA of M0 by 21.5 %. The highest increase can be seen with M12T4 (T4 = four tubes), which has a SEA of 56.28 kJ/kg, providing an increase of 47.7 % relative to the unreinforced

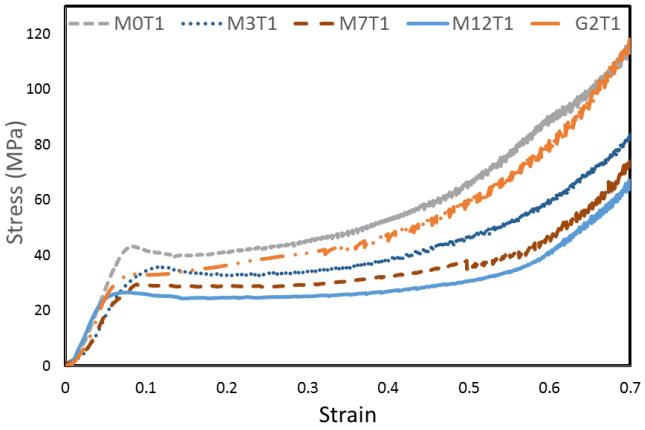

(a) One tube reinforced TSPU

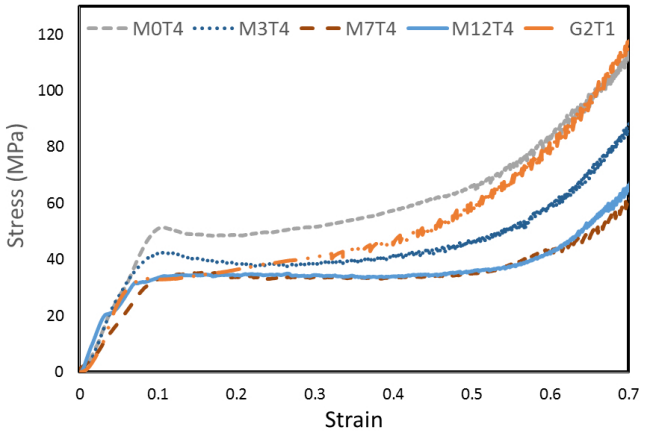

(b) Four tube reinforced TSPU

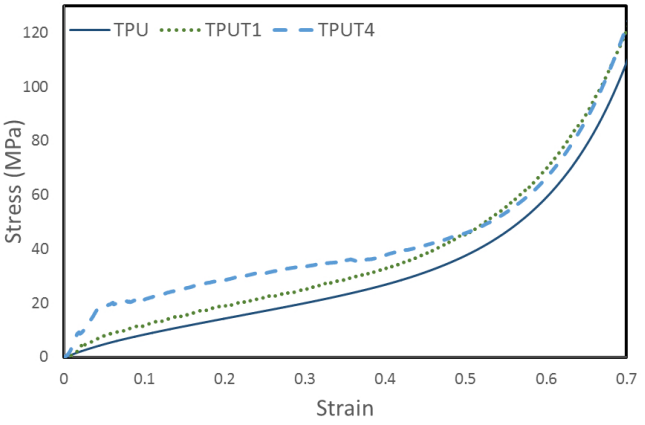

(c) Unreinforced and reinforced (One and four tubes) TPU

Figure 4.5: Quasi-static stress vs. strain curves for (a) 1 CFRP tube reinforced TSPUM0, M3, M7 and M12, (b) 4 CFRP tube reinforced TSPUM0, M3, M7 and M12 and (c) unreinforced and reinforced 1 and 4 tube TPU.

foam, M12. The plateau stress is an important consideration in the design of crash protective structures. Where the structure must absorb the kinetic energy of a moving object without reaching its densification strain, whilst ensuring that the transmitted stress never exceeds the plateau stress. It can be seen that in addition to enhancing the SEA, in all cases the reinforcements increase the plateau stress for all densities.

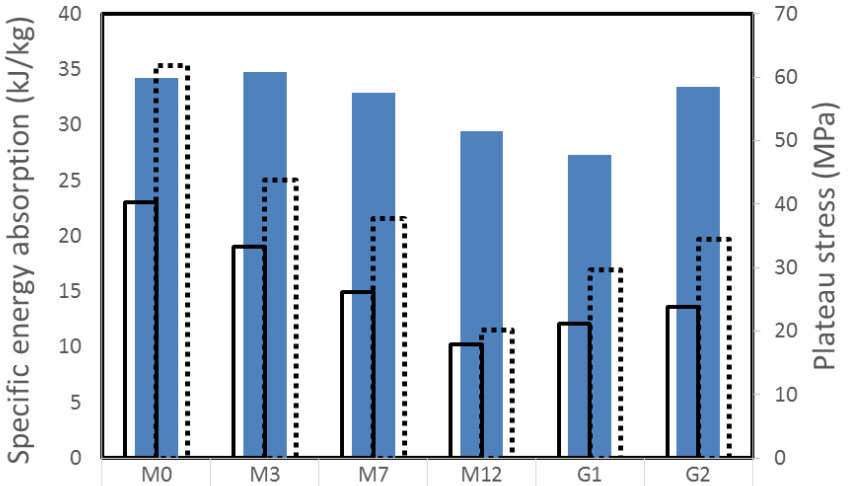

	M0	M3	M7	M12	G1	G2
SEA	34.19	34.73	32.92	29.42	27.27	33.41
25%	40.32	33.32	26.21	17.89	21.16	23.78
50%	61.83	43.76	37.74	20.12	29.72	34.48

(a) Unreinforced

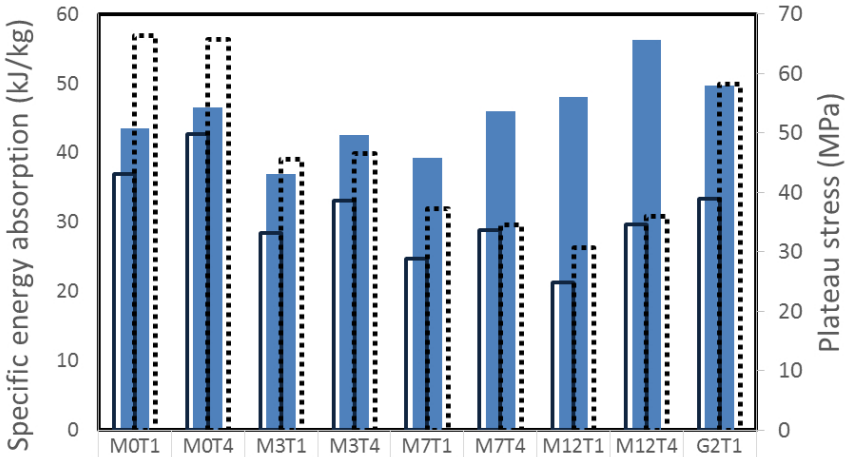

	M0T1	M0T4	M3T1	M3T4	M7T1	M7T4	M12T1	M12T4	G2T1
SEA	43.55	46.49	36.88	42.59	39.25	45.93	48.09	56.28	49.66
25%	43.03	49.81	33.23	38.55	28.92	33.64	24.84	34.61	38.92
50%	66.34	65.67	45.65	46.56	37.26	34.54	30.69	35.91	58.26

(b) Reinforced

Figure 4.6: SEA and plateau stresses at 25 and 50% for the unreinforced (a) and reinforced (b) syntactic TSPU under quasi-static loading.

In order to compare the specific performance of the syntactic foam under quasi-static loading conditions, a comparison of the syntactic foam has been made with a wide variety of materials, as shown in Figure 4.7. This plot considers the specific compressive strength (σ_c/ρ) and specific compressive stiffness (E_Y/ρ) as an indication of performance of the unreinforced and CFRP tube reinforced syntactic TSPU. M12, which has the lowest density, provides a much higher specific compressive stiffness than M0, with a percentage increase of 95 %, whilst the compressive strength is shown to have an increase by just 8.6 % on average. Nevertheless, the best performing reinforced foam, M12T4, is shown to provide a substantial increase, i.e. 65 %, in specific compressive strength with an average value of approximately 55 kPa/(kg/m^3). The specific compressive strength is also shown to be relatively competitive in relation to the honeycombs and metals. It should be noted that the composition and the density of the syntactic TSPU have a dominant effect on the specific mechanical properties of the CFRP reinforced foams.

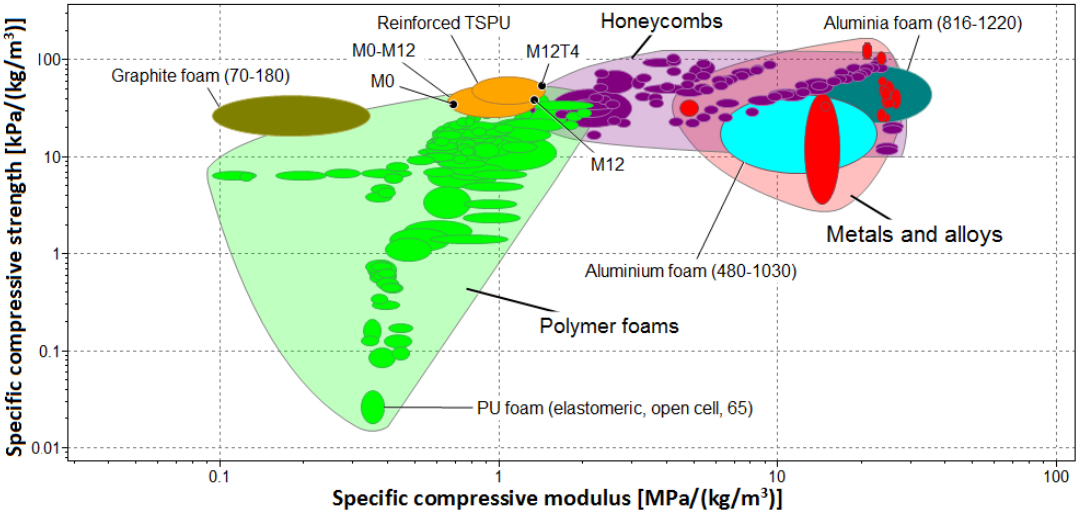

Figure 4.7: Ashby plot comparing the specific compressive properties of the unreinforced/reinforced non-syntactic TSPU M0 and syntactic TSPU. Material data from Ref. [104].

4.1.2 Quasi-static tensile results

As mentioned in Section 2.9.1, usually up to ten different types of experimental tests are necessary in order to measure key mechanical properties for anisotropic materials and isotropic material models are preferred by many engineers and designers to predict the mechanical behaviour of anisotropic materials, to save time and cost for experimental testing [183]. Nevertheless, in many TPUs, since the hard segments are immersed in a soft (rubbery) matrix [220] and occupy a significant volume of the matrix in some TPUs, they function as effective nanoscale fillers [113]. Therefore, it was necessary to determine whether the current TPU exhibited any form of anisotropic behaviour, by a series of tensile tests. These tests consider the mechanical properties in three different orientations, i.e. 0°, 45° and 90°.

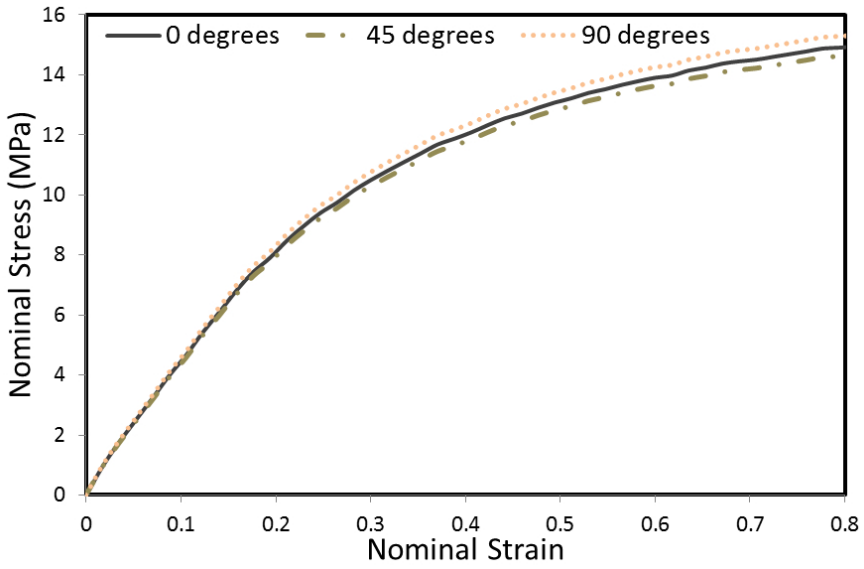

Figure 4.8: Stress-strain curves at three different orientations of 0°, 45° and 90°.

Figure 4.8 indicates that the TPU exhibits very little material anisotropy, with there being minor changes in the material behaviour at 0°, 45° and 90°. Based on this analysis, it is reasonable to assume the material is isotropic [68]. Furthermore, the effect of strain-rate on the failure strain was also tested, as

shown in Figure 4.9, where it is evident that the strain at failure decreases with increasing strain-rate, highlighting a distinct strain-rate sensitivity in the TPU.

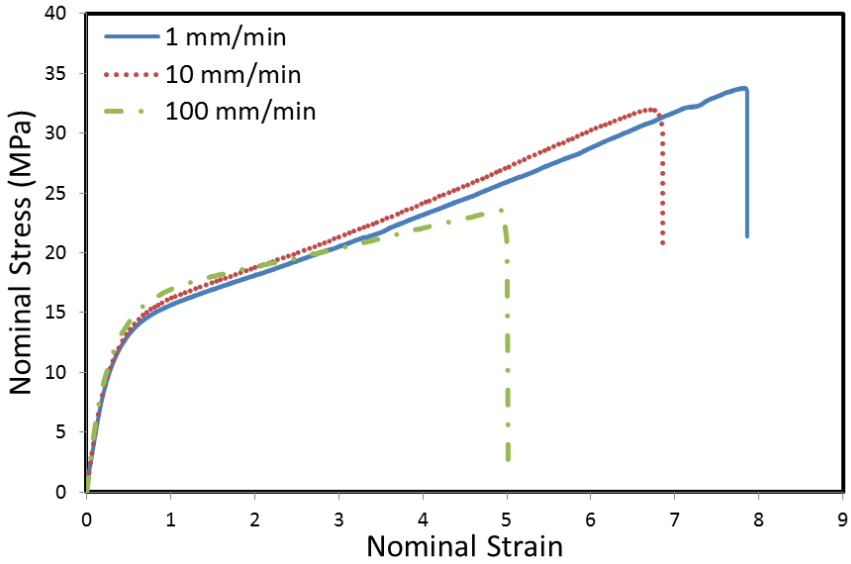

Figure 4.9: Nominal stress-strain curves for TPU (a) and failure strain (b) for increased strain-rates.

4.1.3 Low velocity impact (LVI) results

This section considers the dynamic responses of the structures. Low velocity impact (LVI) tests are carried out on the unreinforced specimens, i.e. TSPU and TPU. This is followed by impact tests carried out on the reinforced specimens with one and four tube arrangements. Dynamic perforation tests are also carried out on both TPU and Aluminium alloy (AA 2024-T3) with a similar mass per unit area.

Unreinforced syntactic TSPU and TPU

Before considering applications of syntactic TSPU and TPU as energy absorbers, it is necessary to investigate their dynamic behaviour. Ideally, a prolonged constant plateau stress level is required to provide the maximum area under the stress-strain curve. There are various parameters that are associated with rate-

sensitivity in cellular materials, i.e. solid material rate-sensitivity, pressure of the trapped air in the cells and micro-inertia effects [221]. The impact response, as depicted in Figure 4.10 for the ungraded TSPU, is shown to be inconsistent with the response observed under quasi-static loading, illustrating the materials sensitivity to an increase in strain-rate. The ungraded foams are characterised by the initial peak stress, although higher than the quasi-static tests, it is then followed by a significant drop in stress with some oscillations in the stress-strain trace. A reduction of this order can be described as complete failure in a large number of applications, indicating shattering fracture of the specimen. The oscillatory behaviour is most likely due to the dynamic effects in the load cell and drop-weight carriage, in addition to the instabilities in the fracture process.

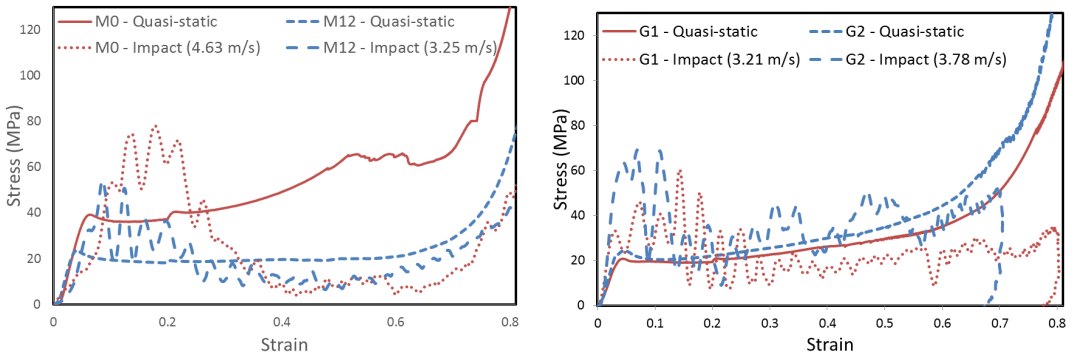

(a) M0 and M12 (b) G1 and G2

Figure 4.10: Quasi-static vs. dynamic stress-strain curves for (a) M0 and M12, (b) G1 and G2.

The graded foam, G1, which is based on a greater variation in densities, provides a more prolonged plateau region than G2, which is consistent with the results of the quasi-static tests. However, G2 exhibits higher plateau stresses, showing an increase of 83.6 % in stress at 50 % strain. Furthermore, the stiffness of both M0 and M12 were shown to be lower under dynamic loading than quasi-static conditions. However, the peak stresses show significant increases, highlighting the strain-rate sensitivity of the TSPU material. On the other hand, the graded foams (G1 and G2) provide a slightly higher stiffness under dynamic loading than

quasi-static loading, in addition to increased peak stresses. Figure 4.11 shows that the plateau stresses for M0 under impact are much lower than that of the quasi-static tests. A similar response was observed for M12 under impact. The plateau stresses for the graded foams however, indicate a significant improvement in comparison to the ungraded foams.

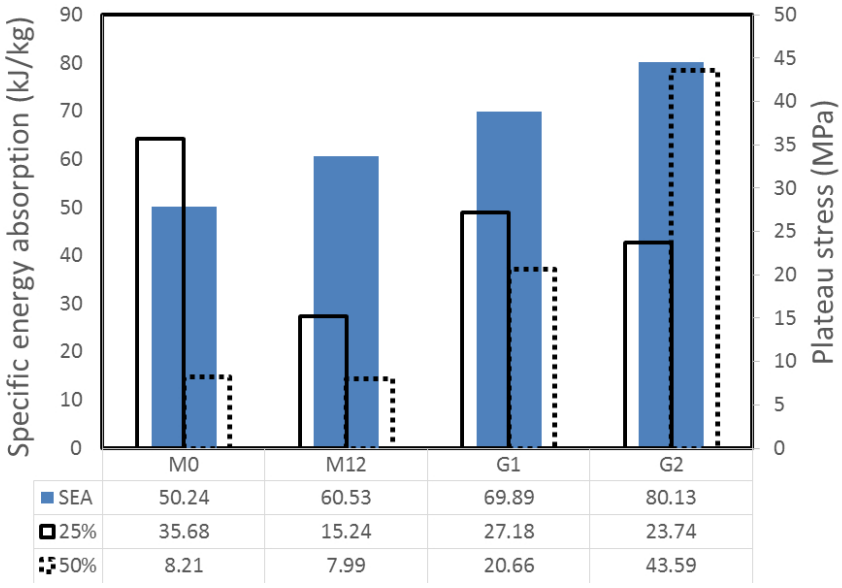

Figure 4.11: SEA and plateau stresses at 25 and 50% for the unreinforced TSPU M0, M12, G1 and G2 under dynamic loading

LVI tests were also carried out on the TPU specimens, with the results presented in Figure 4.12. Here, five impact velocities were tested. Figure (4.12a) shows three of those at strain-rates of 117, 174 and 207 s^{-1}. These experiments illustrate the strong rate dependence and features of the stress-strain behaviour of TPU. Under impact, materials experience large amounts of strain which is dependent upon the magnitude of the impact, temperature range and strain-rates. The nature of the stress-strain curve clearly shows the rate dependency of the TPU. The ratio of the dynamic to static initial peak stresses and plateau stress notably increase with increased impact energy, and present the TPU with increased SEA characteristics, as shown in Figure (4.12b). Furthermore, the underlying material structure of the TPU is also shown to undergo significant changes with the

increased impact energy, with significant deformations being observed from 735 to 1155 J (174 - 207 s^{-1}). The ability of TPUs in altering its microstructure and therefore its mechanical behaviour [113], presents TPU as an attractive polymeric material for such applications.

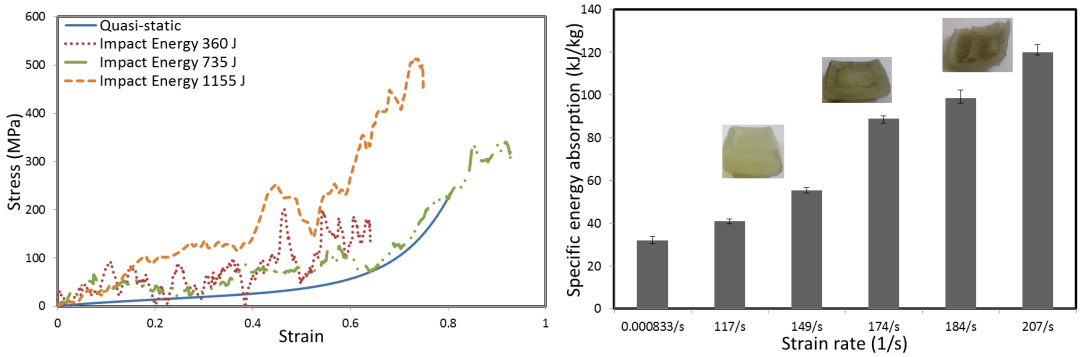

(a) Stress vs. strain

(b) Specific energy absorbed

Figure 4.12: Stress vs. strain (a) and SEA vs. strain-rates (b) for TPU under dynamic loading.

Reinforced syntactic TSPU and TPU

Figure 4.13a shows the impact responses of TPU and syntactic TSPU, with one tube reinforcement. As was the case for the unreinforced TSPU, the behaviour of the reinforced TSPU is characterised by an initial peak followed by a significant drop in the stress. The reinforced TPU under dynamic loading is much stiffer, in distinct contrast to the TPU without reinforcement as shown in Figure 4.12a. Furthermore, the reinforced TPU shows a progressive response with the stress increasing in three steps, making it ideal for dynamic applications by providing a steadily increasing energy absorption capacity.

A direct comparison was also made in relation to tubes with and without a chamfer (ChI) embedded in the graded TSPU specimen, G2. In addition to testing the samples with a low-high density (L-H) and high-low density (H-L) grading. The dynamic stress-strain traces are shown in Figure (4.13b). A single chamfer 45° on the inner diameter of the tubes were used to initiate crushing,

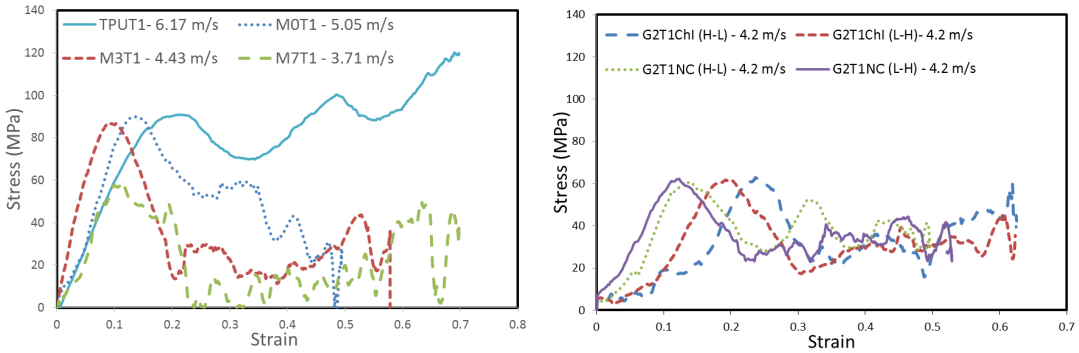

(a) Reinforced M0, M3, M7 and TPU

(b) Reinforced G2

Figure 4.13: Stress vs. strain traces for (a) reinforced TPUT1, TSPUM0T1, M3T1, M7T1 and (b) reinforced G2 with and without chamfered tubes.

to help facilitate failure at the chamfer tip and damage zone propagation in the axial direction of the tube without catastrophic failure. It is shown that the initial peak stress in chamfered tubes is delayed relative to the tubes without a chamfer. This is consistent with both H-L and L-H layups, with H-L providing a slightly more delayed peak stress response.

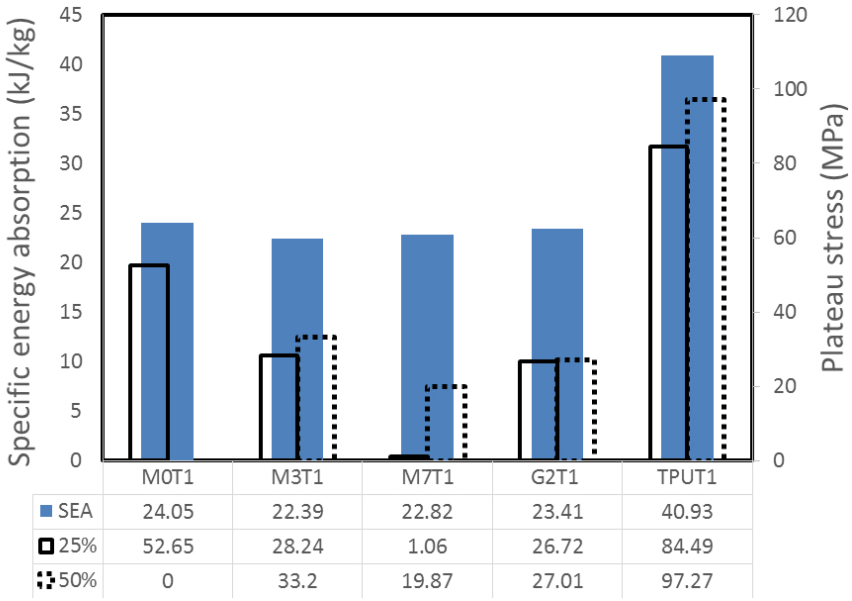

	M0T1	M3T1	M7T1	G2T1	TPUT1
SEA	24.05	22.39	22.82	23.41	40.93
25%	52.65	28.24	1.06	26.72	84.49
50%	0	33.2	19.87	27.01	97.27

Figure 4.14: SEA and plateau stresses at 25 and 50 % strain for the reinforced foams under dynamic loading.

The plateau stresses for the reinforced TSPU and TPU under dynamic loading are presented by Figure 4.14.The potential of the reinforced TPU under dy-

namic loading is further illustrated by the SEA values, with TPUT1 providing the highest SEA. Although the specific energy absorption is lower than that of the unreinforced 20 x 20 x 20 mm TPU samples, due to the limitations of the drop weight tower it is expected that the SEA values for the tube reinforced TPU could increase proportionally for higher impact energies, where more significant deformations of the reinforced TPU may be observed. Figure 4.15 illustrates the brittle nature of the TSPU sample and the enhanced integrity of the TPU under impact, where it can be seen that the latter retains most of its original shape, whilst the tubes in both cases fragment into small debris.

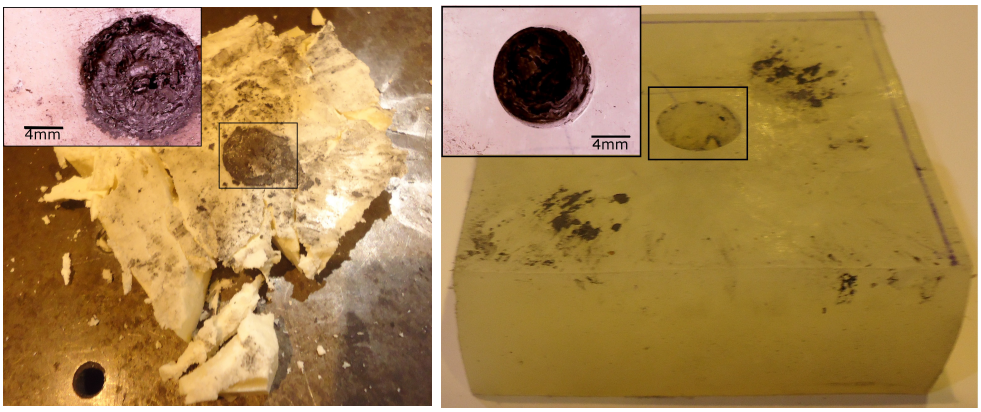

(a) M0 (b) TPU

Figure 4.15: Typical failure of reinforced (4.15a) TSPUM0 and (4.15b) TPU samples under dynamic compressive loading.

Perforation

A further comparison is made of the monolithic TPU against a lightweight monolithic AA 2024-T3 metallic plate to identify the differences between the perforation characteristics of these two materials. The TPU and AA 2024-T3 both have the same areal density of 3.3 kg/m^2, with thicknesses of 2.9 mm and 1.2 mm for the TPU and AA 2024-T3, respectively. From this the competitiveness of the TPU can be assessed, since aluminium alloys are widely used for structural applications, especially in the aerospace industry.

The AA 2024-T3 provides the highest peak load both in static and dynamic perforation, whereas TPU offers a more progressive energy absorption, as shown in Figure 4.16. The failure modes for both AA 2024-T3 and TPU are also shown in Figure 4.16. For the AA 2024-T3 a cap detaches at the tip of the projectile and the failure for the TPU is characterised by radial cracking and the formation of petals.

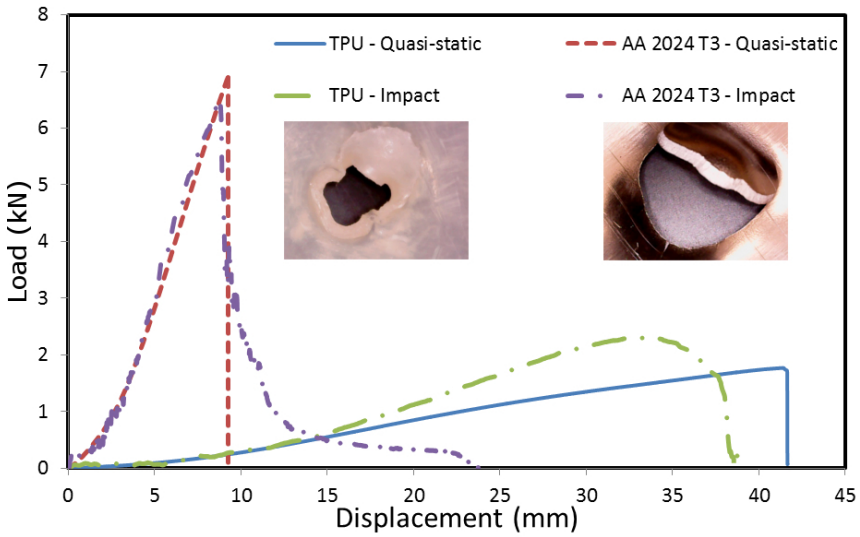

Figure 4.16: Quasi-static and dynamic perforation response of TPU and 2024-T3.

Table 4.2 highlights the durability of TPU in comparison to AA 2024-T3, where the energy absorbed under the same conditions is higher than that of AA 2024-T3. A key difference between the two materials is the strong strain-rate sensitivity of the TPU, which may explain the additional dissipation at higher velocities where the failure mode of the TPU involves large, localised plastic straining.

Table 4.2: Total energy absorbed, E_T, for TPU and AA 2024-T3 under quasi-static and dynamic perforation.

	TPU		AA 2024-T3	
	Static	Dynamic	Static	Dynamic
E_T (J)	36.33	41.71	26.35	36.65

4.1.4 Split-Hopkinsons pressure bar (SHPB) results

To assess the key strain-rate sensitivity of the TPU and TSPU at higher strain rates ($> 10^3$ s^{-1}), this section covers tests undertaken using the split-Hopkinsons pressure bar (SHPB) tests. From this the suitability of both samples can be assessed and applied as a basis for the sandwich panels, to be used for the blast experiments. Results will then be applied to the modelling parameters for the dynamic simulations.

TPU

The TPU samples were tested at several strain-rates, where Figure 4.17 shows plots of true stress versus true strain curves of different strain-rates, with the behaviour showing a strong rate dependence. The true stress-strain relationships highlight appreciable strain-rate effects in the response of the TPU polymer over six decades of strain-rates. The stress levels increase continuously with increasing strain-rate. There was no visible evidence of failure at strain-rates below 5000 s^{-1}. However, at a strain-rate of 7170 s^{-1}, fracture initiated on the impact face and large visible cracks are observed at 8316 s^{-1}, as illustrated by Figure 4.18.

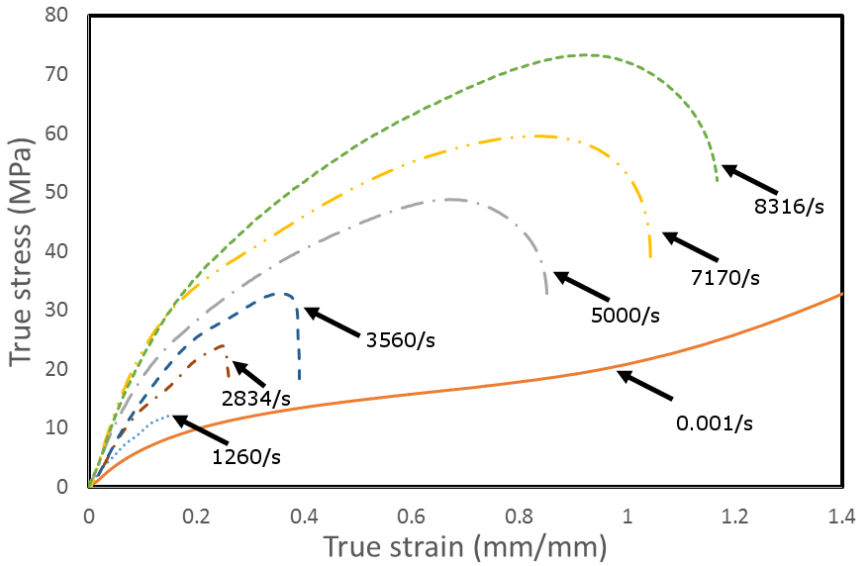

Figure 4.17: True stress vs. true strain for TPU at various strain-rates.

Overall, the shape tendency of the stress-strain curves remains similar under the higher strain-rate loadings, with an apparent strain hardening period after initial loading. Furthermore, it is evident that the strain energy release of the TPU increases with increased strain-rate, which could be a really useful strain-rate dependent behaviour under shock loading conditions. Access to such strain-rates enables precise characterisation of the strong dependence of the stress-strain behaviour for increased strain-rate loading.

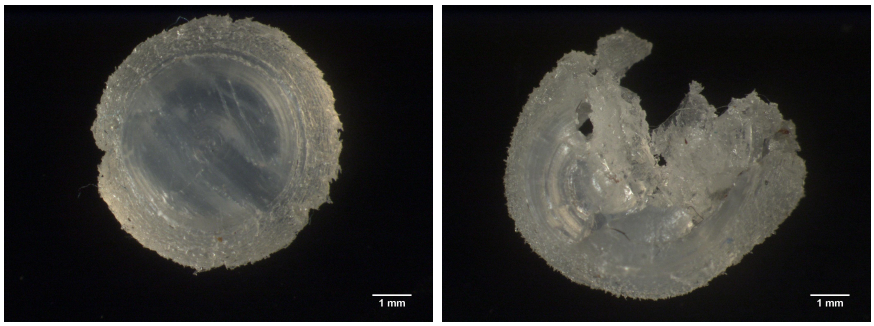

(a) 7170 s^{-1} (b) 8316 s^{-1}

Figure 4.18: Failure of TPU observed at strain-rates (a) 7170 and (b) 8316 s^{-1}.

TSPU

Additional SHPB tests were carried out on the TSPU samples, M0, M3, M7 and M12. Figures 4.19 shows plots of true stress versus true strain curves of different strain-rates. Some strain sensitivity was shown where the peak stress is of an order of magnitude greater than the quasi-static test, which suggests that micro-inertia has some effect on the constituent properties of the syntactic foams. Discrepancies however, are evident with TSPUM12 where the peak forces, although they are increasing with increased strain-rate, are lower than that of the quasi-static tests. Unlike the TPU samples which showed 'rebound' at similar strain-rates, the TSPU samples (M0, M3, M7 and M12) indicated either complete catastrophic failure, or visible macro-cracks in the samples.

A strain-rate sensitivity parameter, as reported by Balch *et al.* [222], is used

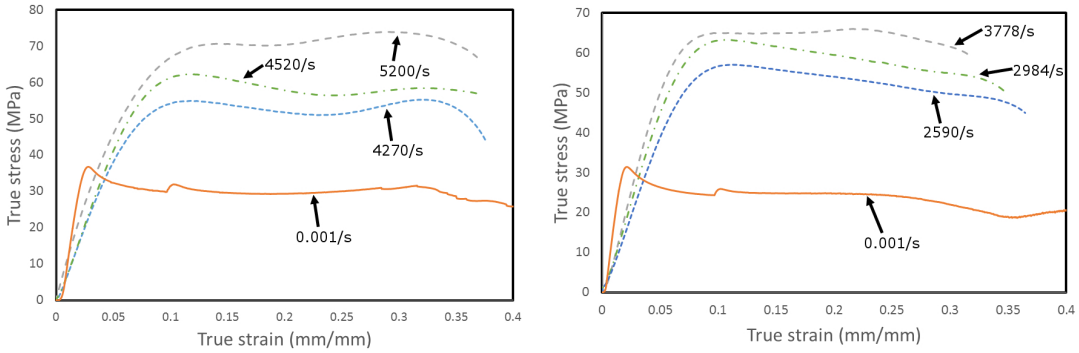

(a) TSPUM0

(b) TSPUM3

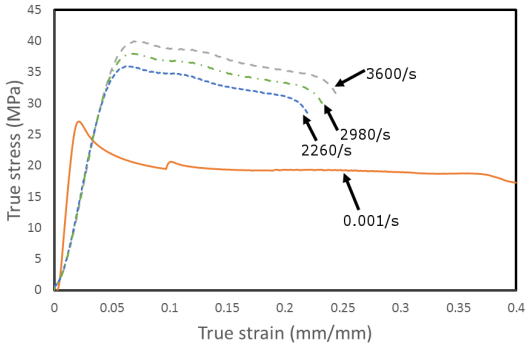

(c) TSPUM7

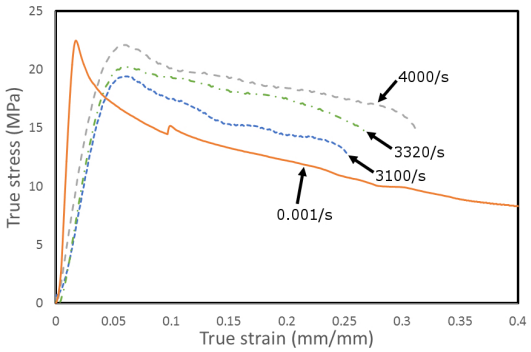

(d) TSPUM12

Figure 4.19: True stress vs. true strain for TSPUM0, M3, M7 and M12 at various strain-rates.

to evaluate the effect of strain-rate on the material at dynamic loading. The strain-rate sensitivity parameter, $\sum$, is calculated using Equation (4.1).

$$\sum = \frac{\sigma_d - \sigma_q}{\sigma^*} \left[\frac{1}{ln \frac{\dot{\epsilon}_d}{\dot{\epsilon}_q}} \right] \tag{4.1}$$

where σ is the stress, σ^* is the static stress at 5 % strain at a reference strain-rate of 10^{-3} s^{-1}, $\dot{\epsilon}$ is the strain-rate and d and q are subscripts that represent dynamic and quasi-static testing, respectively. Figure 4.20 shows that the sensitivity parameter is in the range of 0.0039-0.0980. It is clear that the strain-rate sensitivity of the syntactic foam is increased in reference to the TSPU without microspheres. However, the strain-rate sensitivity of the syntactic foams begins to diminish from samples M7 to M12, with M3 showing the highest values. This suggests that the microspheres embedded in the matrix do help enhance the prop-

erties of the materials up to a certain limit, where the glass microspheres which introduce stress concentrations begin to have an adverse effect on the structural integrity of the TSPU with higher volume fractions. Based on these tests results, it is indicative that these samples may not be suited for blast loading situations, unlike the TPU which presents higher versatility under such loads.

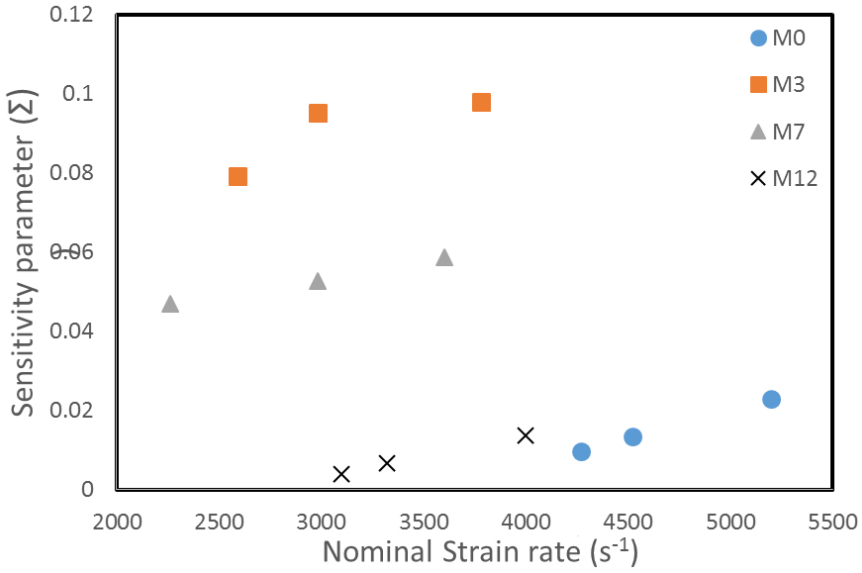

Figure 4.20: Plot of strain-rate sensitivity ($\sum$) versus strain-rate for samples TSPU M0, M3, M7 and M12.

4.1.5 Blast results

Table 4.3 shows the response of the specimens tested under blast loading, including impulse (Ns), and the residual mid-point deflection (mm) of the back face. The diameter of the explosives was increased from 20 to 30 mm due to the limitations for the charge height to diameter ratio [218]. That is, for a certain diameter, increasing the explosive mass results in an increase in height, which influences the impulse generated by the explosive. Therefore, the diameter of the explosive has to be adjusted accordingly to maintain increased impulse. The impulses generated by the 20 mm diameter explosives were in the range of 11.8 - 15.8 Ns and those for the 30 mm explosives in the range of 14.1 - 24.6 Ns.

Table 4.3 details the various failures observed in each of the samples, i.e. Mode I (large inelastic deformation), Mode II* (partial tearing around the boundary) and Mode II (tensile tearing around the full boundary).

Table 4.3: Charge mass and diameter, impulse, failure and back face deflection for the specimens. T - full tearing and PT - partial tearing around the boundary

ID	Charge mass (g)	Charge diameter (mm)	Impulse (Ns)	Failure mode	Back face mid-point deflection (mm)
A1	8	20	11.81	I	12.17
A2	9	20	12.43	I	13.80
A3	10	20	13.09	I	14.03
A4	11	20	13.87	I	14.10
A5	12	20	14.88	II*	PT
B1	11	20	13.95	I	13.44
B2	12	20	14.68	I	13.84
B3	13	20	15.81	I	15.14
B4	14	30	18.04	II	T
C1	9	30	14.35	I	13.15
C2	10	30	17.17	I	13.57
C3	11	30	18.44	II*	PT
D1	9	30	14.13	I	5.24
D2	11	30	18.40	I	12.24
D3	13	30	23.74	I	15.33
D4	15	30	24.65	II*	PT
E1	13	20	15.62	D	11.19
F1	14	30	22.24	D	16.49

For the TPU specimens without skins, an increased deflection was observed with increasing mass of explosive, until partial tearing was observed with 12 grams of PE4. Figure 4.21 illustrates the failed sample of the TPU with the skins (C3), whereas Figure 4.22 shows the failed A5 sample under blast without AA 2024-T3 skins, both showing a partial tearing (mode II*) failure mode. It should be noted that post-mortem removal of the skins revealed that the TPU had a very good recovery. The stress-wave propagation through the multi-layered material and the rebound of the TPU core caused the adhesive to fail, whilst the AA 2024-T3 skins continued to deform plastically without rebound.

Table 4.4: Comparison of various specimens subject to uniform blast loading with comparisons made against areal density (kg/m^2), approximate material cost (GBP/kg), SOD (mm) and resistance to impulse (Ns) prior to failure.

Specimen	Areal density (kg/m^2)	Material cost (GBP/kg)	SOD (mm)	Impulse (Ns)
TPU (A4)	5.75	2.62 - 3.19	90	13.87
AA/TPU (B3)	12.32	2.72 - 3.29	90	15.81
CF/PEI [53]	12.41	26.3 - 29.2	90	14.00
GF/PEI [53]	8.60	17.1 - 24.1	90	7.93
Stitched panels[1] [76]	4.91	45.48 - 48.64	90	9.93
Mild steel [219]	14.61	0.41 - 0.42	50-100	17.94-25.36

[1] Three-dimensional woven S-glass/epoxy skins and a crosslinked PVC core

As mentioned in Section 2.2, a materials' low failure strain is one of the limiting factors in their performance [52]. An example of which can be seen in the work undertaken by Yahya *et al.* [53], where it is observed that the TPU, used in this study, outperforms most of the T300 carbon fiber-reinforced poly-ether-imide (CF/PEI) panels. One of the CF/PEI panels tested by Yahya *et al.* [53] had an average thickness of 8.22 mm and a density of 1510 kg/m^3, providing a much higher mass per unit area than that of the TPU panels (without skins), which has a density of 1150 kg/m^3. Yet complete failure, i.e. matrix cracking, delamination, fibre buckling and fibre fracture, was observed following the test with just 8 grams of PE4 for the CF/PEI panels. This is particulary critical in blast loadings, due to the high strain-rate impulsive loadings that are involved. Therefore, the search in finding a material which possess higher strain to failure property would be expected to perform better in blast and impact loadings [52].

The TPU without skins, with a 5 mm thickness, was able to withstand up to 11 grams of PE4 explosive, with failure occurring at 12 grams, illustrating the versatility and toughness of TPU. Further tests were carried out on sandwich panels with cores having various thicknesses. Increases in the resistance of impulse was seen with the addition of AA 2024-T3 skins, relative to the plain TPU, however further increases were observed in relation to core thickness, where increases of

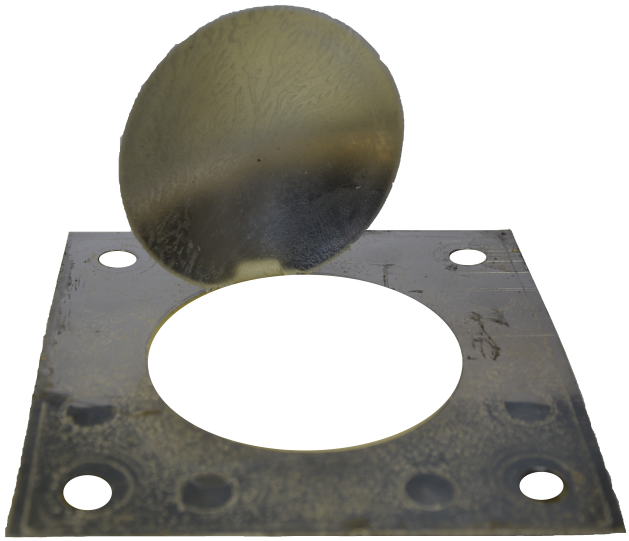

Figure 4.21: Back face tearing failure of AA/TPU/AA (C3).

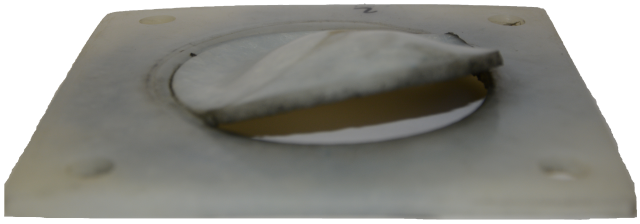

Figure 4.22: Partial tearing failure of TPU (A5) without skins.

6.3, 15.4 and 59.5 % are observed for core thicknesses of 5, 10 and 20 mm, respectively. Table 4.4 provides a brief comparison of various panels tested by previous studies on the ballistic pendulum, indicating average areal density (kg/m^2), approximate material cost (GBP/kg) and resistance to impulse (Ns) prior to failure. In comparison, TPU alone is a relatively low cost and lightweight alternative with promising results for blast mitigation.

An investigation of the use of CFRP tube reinforcements for the TPU, shows that the tubes reinforcements, contrary to the impact tests, had very little influence on the tests under blast loading. In some cases the tubes simply do not have enough time to respond due to the debonding of the back face, which could

be a consequence of the adhesive used. Although, some localised damage on the tubes was observed for the thicker reinforced samples, i.e. E1, as illustrated by Figure 4.23. Nevertheless, it is apparent that the introduction of CFRP tubes for the TPU under these types of loadings was not as effective, which may be due to the debonding of the skins.

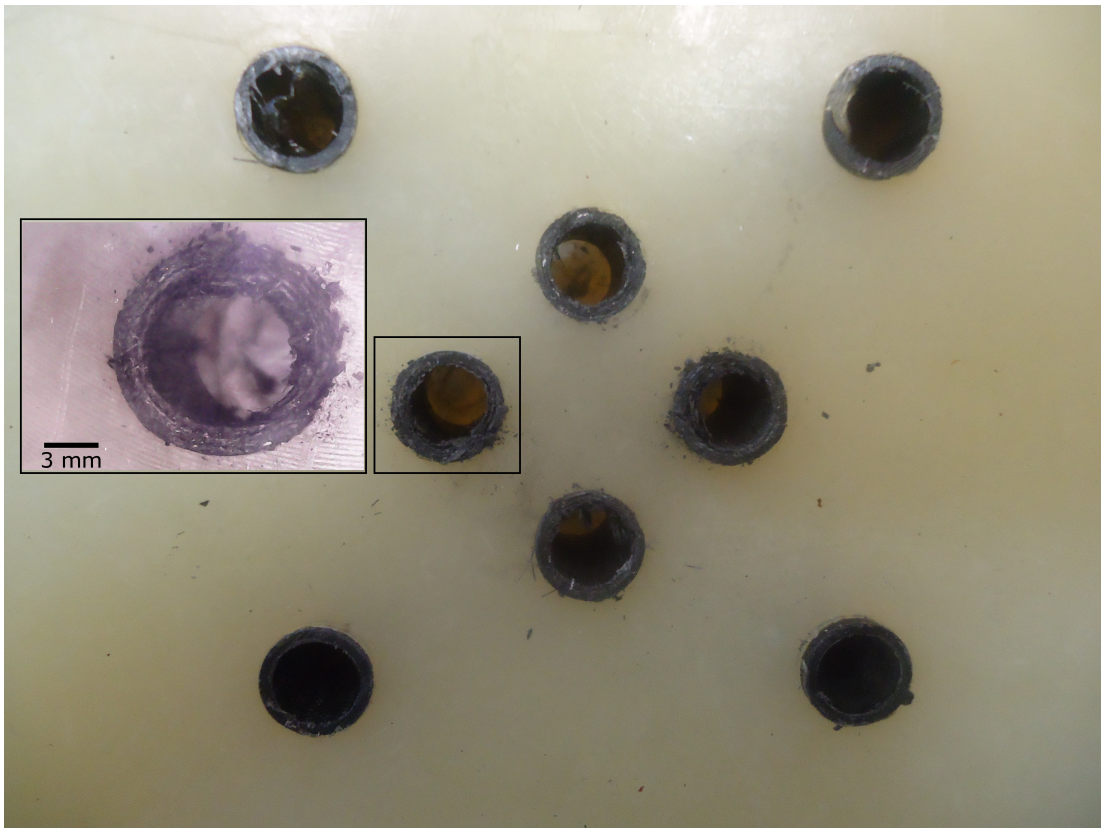

Figure 4.23: Localised failure of CFRP tubes for sample E1 (22.24 Ns).

4.2 Summary of Experimental Results

Quasi-static and dynamic experimental investigations on TPU and TSPU have been presented in this chapter. The modification of TSPU with hollow glass microspheres (HGMs) has also been investigated, where it is shown that decreasing the density of the syntactic foam with HGMs leads to some increase in specific energy absorption (SEA) under quasi-static loading, with the highest value shown for M3. The load bearing capacity of the CFRP tube reinforced syntactic TSPU foams was increased significantly relative to the unreinforced syntactic TSPU, where SEA increases as high as 48 % (56.28 kJ/kg) were noted. In addition to this, the specific compressive strength (σ_c/ρ) increased by 65 % reaching 55 kPa/(kg/m^3).

The post-yield behaviour under dynamic loading was reduced for the pure TSPU (no glass microspheres), which experienced stain-hardening under quasi-static loading, whereas under dynamic loading it exhibited a significant drop in the plateau stress. This behaviour was consistent with the syntactic foams (with glass microspheres). Improvements in the plateau levels were made by introducing a graded structure, since it resulted in a more progressive response and a relatively constant stress level under dynamic loading. Furthermore, the specific energy absorption characteristics of TPU under dynamic loading was shown to increase with increasing impact energy, making them an attractive prospect to structural impact applications. The incorporation of CFRP tubes into the TPU greatly improved their properties and presents the reinforced TPU with greater energy absorbing characteristics under impact loading conditions. The competitiveness of TPU was also assessed against a widely used aluminium alloy (AA) 2024-T3 where the TPU offered greater energy absorption under low velocity perforation tests.

TPU exhibited a strain-rate sensitivity under high strain-rate loading, as es-

tablished by a series of split-Hopkinsons pressure bar (SHPB) tests, indicating significant strain energy potential under high strain-rate loading. The TSPU on the other hand, showed some strain-rate sensitivity up to a limit, where the sensitivity parameter ($\sum$), indicated a significant drop with higher volume fraction of microspheres. The overall response of the TSPU was negative under such loading where catastrophic failure highlighted by a significant drop in stress was observed. Based on these experiments, the TPU was chosen to form the basis of the core for the sandwich structure.

The results of an investigation on the response of thermoplastic polyurethane (TPU) sandwich panels subjected to blast loading has also been reported.The TPU under blast loading was also shown to withstand relatively high PE4 explosive masses (up to 11 grams), providing a lightweight and low cost alternative to various other materials reported in the literature. The addition of AA 2024-T3 skins as a basis of a sandwich construction provided additional resistance to impulsive loads. Increases in the blast resistance relative to the plain 5 mm TPU of 14.0, 23.8 and 71.2 % were observed with the addition of AA 2024-T3 skins and increases in the core thicknesses of 5, 10 and 20 mm, respectively.

Chapter 5

Finite Element (FE) Modelling and Results

This chapter presents the development of FE models and constitiutive relationships for the energy absorbing structures. The Finite Element (FE) theory and methods were used to numerically model the response of the structures presented in Chapters 3 and 4 under quasi-static and dynamic loads using the finite element package ABAQUS (version 6.14). The numerical data were compared to corresponding experimental data in order to validate the finite element models. ABAQUS was used to create, run and visualise both the static and dynamic models. The quasi-static analysis were conducted using Abaqus/Standard, while the dynamic analyses were conducted using Abaqus/Explicit.

5.1 Time Integration

5.1.1 Abaqus/Standard

Abaqus/Standard is a general-purpose finite-element analysis software that is applicable in solving a wide variety of linear and nonlinear problems involving the static, dynamic, thermal, and electrical response of components. This method employs an implicit integration scheme, i.e. solving a system of equations implicitly at each solution increment.

5.1.2 Abaqus/Explicit

Abaqus/Explicit is a special-purpose analysis package that uses an explicit dynamic finite element formulation.This method is suitable for solving high-speed dynamic events that require a number of small increments in obtaining a high-resolution solution. If the event has a short duration, the solution could be obtained relatively efficiently. Contact conditions and other extremely discontinuous events are readily formulated in the explicit method and can be enforced on a node-by-node basis without iteration. The nodal accelerations can be adjusted to balance the external and internal forces during contact. Abaqus/Explicit marches a solution forward through time in small time increments without solving a coupled system of equations at each increment or even forming a global stiffness matrix.Therefore, this method was used to model the impact and blast problems carried out in this study.

5.2 Constitutive Relationships

This section covers the constitutive relationships that are implemented for the modelling of TPU, TSPU, AA 2024-T3 and CFRP tube; the material parameters for these are also provided.

5.2.1 Elasto-plastic

Elasticity

For materials that exhibit a linear elastic material behaviour, the total stress is defined from the total elastic strain as,

$$\sigma = D^{el}\epsilon^{el} \tag{5.1}$$

where σ is the total stress, D^{el} is the fourth order elasticity tensor and ϵ^{el} is the total elastic strain.

For isotropic linear elasticity, the stress-strain relation is given by,

$$\begin{Bmatrix} \epsilon_{11} \\ \epsilon_{22} \\ \epsilon_{33} \\ \gamma_{12} \\ \gamma_{13} \\ \gamma_{23} \end{Bmatrix} = \begin{bmatrix} 1/E_Y & -\nu/E_Y & -\nu/E_Y & 0 & 0 & 0 \\ -\nu/E_Y & 1/E_Y & -\nu/E_Y & 0 & 0 & 0 \\ -\nu/E_Y & -\nu/E_Y & 1/E_Y & 0 & 0 & 0 \\ 0 & 0 & 0 & 1/G & 0 & 0 \\ 0 & 0 & 0 & 0 & 1/G & 0 \\ 0 & 0 & 0 & 0 & 0 & 1/G \end{bmatrix} \begin{Bmatrix} \sigma_{11} \\ \sigma_{22} \\ \sigma_{33} \\ \sigma_{12} \\ \sigma_{13} \\ \sigma_{23} \end{Bmatrix} \tag{5.2}$$

where the elastic properties are defined by the Young's modulus, E_Y, and the Poisson's ratio, ν, of the material. The shear modulus, G, can be expressed in terms of E_Y and ν as,

$$G = \frac{E_Y}{2(1+\nu)} \tag{5.3}$$

To ensure stability in the model, the material properties must fall within certain limits. The stability criterion requires that $E_Y > 0$, $G > 9$ and $-1 > \nu > 0.5$.

Plasticity

Beyond the elastic region of a material, i.e. the yield point, plastic behaviour begins to occur resulting in permanent deformation of the material. Isotropic materials have yield surfaces that increase in size uniformly in all directions, such that as plastic strain occurs, the yield stress increases in all of the stress directions. Here, the TPU was developed using a classical plasticity model, based on a von Mises yield surface for an isotropic yield. To determine the values of isotropic hardening, the yield stress, σ_y, is given as a tabular function of the plastic strain. The classical plasticity models are useful when rate-dependent effects are important, which will be discussed in Section 5.2.1. The decomposition of the total increment of strain can be expressed as,

$$d\epsilon = d\epsilon^{el} + d\epsilon^{pl} \tag{5.4}$$

Failure criteria

Generally material degradation due to fracture, crack propagation and coalescence of micro-cracks or voids in material elements are the key reasons for failure in material. Here, a ductile damage criterion for both quasi-static and dynamic cases was used to model the TPU. The equivalent fracture strain was used as a measure of failure to predict the onset of damage. The equivalent plastic strain at the beginning of damage, $\bar{\epsilon}_D^{pl}$, is a function of the stress triaxiality, η, and strain-rate, $\dot{\bar{\epsilon}}^{pl}$.

$$\eta = -\frac{p}{\sigma_v} \tag{5.5}$$

where σ_v is the von Mises equivalent stress and p is the pressure stress which is defined as,

$$p = \frac{1}{3}(\sigma_{11} + \sigma_{22} + \sigma_{33}) \tag{5.6}$$

Failure associated with this ductile criterion activates once the following condition is satisfied,

$$\omega_D = \int \frac{d\bar{\epsilon}^{pl}}{\bar{\epsilon}^{pl}_D(\eta, \dot{\bar{\epsilon}}^{pl})} = 1 \tag{5.7}$$

where ω_D is a state variable that increases with plastic deformation. During the analysis, the incremental increase in ω_D at each increment is calculated as,

$$\Delta\omega_D = \int \frac{d\bar{\epsilon}^{pl}}{\bar{\epsilon}^{pl}_D(\eta, \dot{\bar{\epsilon}}^{pl})} \geq 0 \tag{5.8}$$

The inclusion of fracture energy in the material parameters, enables the user to control damage development that is associated with ductile deformation, in terms of the energy required for failure development, i.e.

$$\sigma = (1 - D)\bar{\sigma} \tag{5.9}$$

where D is a damage variable and $\bar{\sigma}$ the yield stress at a non-zero plastic strain-rate.

Rate dependency

The TPU was modelled as an isotropic elasto-plastic material that exhibits rate-dependency utilising the Cowper-Symonds power law [223]. The total strain rate can be decomposed into an elastic component, $\dot{\epsilon}^{el}$, and a plastic component, $\dot{\epsilon}^{pl}$. Generally, plastic flow stress σ_{pl} of a material can be expressed as,

$$\sigma_{pl} = f(\epsilon_{pl}) \cdot R(\dot{\epsilon}) \tag{5.10}$$

where f is the quasi-static stress-strain behaviour imported into ABAQUS from

the true stress-strain curves, whereas R represents the ratio of the yield stress at any strain-rate to the static yield stress and $\dot{\epsilon}$ represents the strain-rate.

In order to incorporate strain-rates effects in the TPU, a Cowper-Symonds model is used as follows,

$$\dot{\epsilon}_{pl} = a(R-1)^b \tag{5.11}$$

The following power-law relationship for higher strain rates to the static yield stress is given as,

$$\sigma_s = \sigma_0 \left[1 + \left(\frac{\dot{\epsilon}_{pl}}{a}\right)\right]^{1/b} \tag{5.12}$$

Here, $\dot{\epsilon}_{pl}$ is the corresponding strain-rate whereas, σ_s and σ_0 represents the yield stress at higher strain-rates and static yield stress, respectively. a and b are material parameters, which can be determined from the SHPB tests as discussed in Section 4.1.4 by a regression procedure [224]. Subsequently, the coefficients for the Cowper Symonds parameters, a and b, were determined to be 971 and 0.98, respectively. The material properties for the TPU are given in Table 5.1, and the isotropic hardening data for the TPU polymer are given in Table 5.2.

Table 5.1: Material properties and parameters for TPU used in the finite element modelling.

Properties	Value
Young's modulus, E_Y (MPa)	158
Poisson's ratio, ν	0.4
Density, ρ (kg/m^3)	1150
Strain-rate(s $^{-1}$)	0.001
Fracture strain for ductile damage	2.9
Stress triaxiality	0.33

Table 5.2: Isotropic hardening data for TPU.

Yield stress (MPa)	11.05	25.92	45.36	119.02	265.26	295.43	390.17
Plastic strain	0	0.36	0.76	1.42	1.90	2.18	2.97

5.2.2 Johnson-Cook

The aluminium alloy used for the skins, namely AA 2024-T3, was modelled using the Johnson-Cook constitutive model [225] with rate-dependent hardening model and corresponding damage law as,

$$\bar{\sigma} = [A + B(\bar{\epsilon}_{pl})^n]\left[1 + C\ln\left(\frac{\dot{\bar{\epsilon}}_{pl}}{\dot{\epsilon}_0}\right)\right] \tag{5.13}$$

where $\bar{\sigma}$ is the equivalent stress, $\bar{\epsilon}_{pl}$ is the equivalent plastic strain, n is a strain hardening index, $\dot{\bar{\epsilon}}_{pl}$ is the equivalent plastic strain-rate and $\dot{\epsilon}_0$ is the reference strain-rate. Temperatures were not taken into consideration in this study. A, B, C and M are materials constants. These material parameters [226], together with elastic properties used to model the AA 2024-T3, are provided in Table 5.3. Parameters A and B have been obtained from the tensile stress-strain relationship obtained in this study.

Table 5.3: Johnson-Cook parameters and the assumed elastic properties for AA 2024-T3 [226].

ρ (kg/m^3)	E_Y (GPa)	ν	A (MPa)	B (MPa)	n	C	m	$\dot{\bar{\epsilon}}_0$
2740	73.09	0.33	349	426	0.73	0.0083	1	0.001

The Johnson-Cook damage law [225] is widely used to provide a simple mathematical relation which describes the effects of stress triaxiality, strain-rate and temperature on the equivalent strain to ductile fracture. The failure of the alloy was modelled as,

$$\epsilon_f = \left[D_1 + D_2 exp\left(D_3\frac{P}{\bar{\sigma}}\right)\right]\left[1 + D_4\ln\left(\frac{\dot{\bar{\epsilon}}}{\dot{\epsilon}_0}\right)\right] \tag{5.14}$$

Table 5.4: Damage constants for the AA 2024-T3 [226].

D1	D2	D3	D4
0.130	0.130	-1.500	0.011

where ϵ_f is the equivalent strain to fracture at the current conditions of strain-rate, temperature, pressure and equivalent stress, P is a pressure stress, $D1 - D4$ are four non-dimensional material constants and are listed in Table 5.4.

5.2.3 Crushable foam

All the phenomenological responses of a material need to be selected when considering material models. ABAQUS contains material models implemented for crushable foams based on Deshpande and Fleck's work [227]. The Crushable foam with Isotropic Hardening (CIH), is an authentic representation of the simplified version of Deshpande and Fleck's model. Crushable Foam with Volumetric Hardening (CVH) is also available inside ABAQUS, which accounts for the brittle response in tension and the high strain energy capacity of foams in compression [183].

CIH assumes an isotropic yield surface, as well as isotropic hardening with control of the flow potential through the plastic Poisson's ratio. The CVH material model, assumes a null plastic Poisson's ratio, which means that there is no control over the flow, although there are some parameters through which one is able to shape the initial yield surface to control the numerical limitations i.e. convergence problems [183]. The CVH material model implemented is written in Equations 5.15 and 5.16.

$$f = [\sigma_v^2 + \alpha^2(\sigma_m - \sigma_0^2)] - \left[1 + \left(\frac{\alpha}{3}\right)^2\right]\sigma_y^2 \leq 0 \tag{5.15}$$

$$\sigma_v = \sqrt{\frac{3}{2}S_{ij}S_{ij}} \qquad and \qquad \sigma_m = -\frac{\sigma_{kk}}{3} \tag{5.16}$$

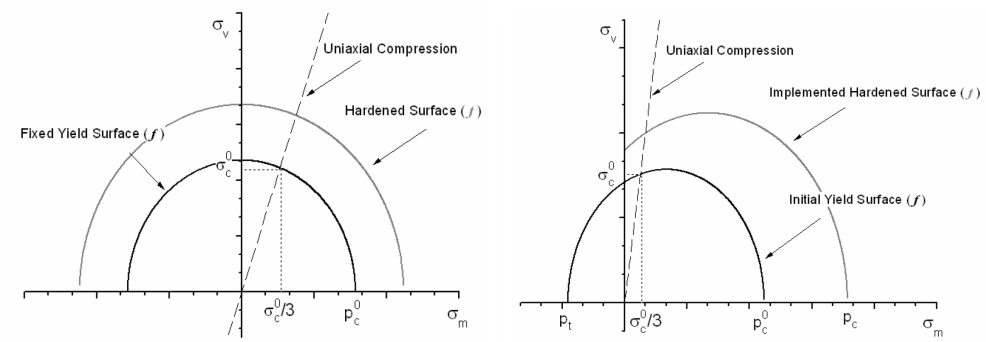

(a) CIH model (isotropic hardening) (b) CVH model (volumetric hardening)

Figure 5.1: Initial yield surface (a) CIH (b) CVH [183].

where, σ_v is the von Mises equivalent stress, σ_m is the mean stress; σ_0, α and σ_y are parameters that can be identified experimentally; S_{ij} is the second invariant stress deviator tensor.

Figure 5.1a, shows the yield surface for the CIH model, which evolves uniformly on all loading paths. Figure 5.1b, illustrates the initial yield surface and a new generic yield surface, for the CVH material model. p_t represents the negative hydrostatic tension yield stress, p_c represents the positive hydrostatic compressive yield stress, superscript "zero" indicates the yield initial value and σ_c^0 represents the uni-axial compression yield stress. From Figure 5.1b, for negative mean stress values, the surface does not yield and the material can be assumed to be perfectly plastic [183]. Therefore, the surface does not evolve at the left side of the invariant stress plane (σ_v vs. σ_m). Although, when the mean stress values are positive, i.e. compressive loadings occur, the surface normally evolves at the right side of the invariant stress plane [183].

To identify the materials yield stress σ_y one can use the data from uni-axial tests. σ_0 is the translational value of the yield stress in the mean stress axis (value at the abscissa coordinate). The parameter α can be defined by the following equations:

$$\alpha = \frac{3k}{\sqrt{(3k_t + k)(3 - k)}} \tag{5.17}$$

$$k = \frac{\sigma_c^0}{p_c^0} \tag{5.18}$$

$$k_t = \frac{p_t}{p_c^0} \tag{5.19}$$

This shows that the parameter α is dependent upon k and k_t, which are the parameters that are to be calibrated within ABAQUS along with the hardening curve. For the elastic phase the material is considered to be isotropic, therefore, the usual elastic Poisson's ratio and Young's modulus are required. In the plastic regime, the CVH model assumes a null plastic Poisson's ratio (υ_{pl}), which locks the control over the flow potential. A control over the shape of the yield surfaces through the ratio k and k_t are offered instead. An initial isotropic yield surface can be defined in the CVH model by setting σ_0 equal to "0" and k_t equal to "1" [183].

Additionaly, a yield surface needs to be defined and an adequate hardening curve needs to be established for an accurate simulation of the mechanical behaviour of the foam. The hardening curve can be established by defining the logarithmic plastic strain versus the respective stress from the experimental uniaxial tests [183]. In comparison the definition of the hardening curve for the CVH model is more complex and is dictated by the stretching of the yield surface in the mean stress axis by the increase of the current hydrostatic yield stress in compression, p_c. As the strain exceeds ϵ_y, volumetric compaction occurs and p_c expands whilst p_t remains constant, this is described in Equation 5.20. For isotropic hardening, Equation 5.21 can be used to define the yield stress.

$$P_c(\epsilon_{vol}^{pl}) = \frac{\sigma_y(\epsilon_{vol}^{pl})[\sigma_y(\epsilon_{vol}^{pl})(\frac{1}{\alpha^2} + \frac{1}{9}) + \frac{p_t}{3}]}{p_t + \left[\frac{\sigma_y(\epsilon_{vol}^{pl})}{3}\right]} \tag{5.20}$$

$$P_c = \frac{\sigma_c\sqrt{1 + (\frac{\alpha}{3})^2}}{\alpha} \tag{5.21}$$

Although the pseudo-plastic crushing behaviour of a foam is related to the underlying microscopic deformation mechanics, the macroscopic plastic behaviour can still be described by a yield surface and hardening rule. Due to limitations of experimental data and those that are required for the CVH model, simulation of the syntactic TSPU was modelled using the CIH model. For isotropic hardening, the shape factor, α, can be calculated using Equation 5.22, where k is defined by Equation 5.18. In the absence of hydrostatic data, the yield stress ratio, k, can also be defined with the use of the plastic Poisson's ratio, ν_p, as defined by Equation 5.23.

$$\alpha = \frac{3k}{\sqrt{9 - k^2}} \tag{5.22}$$

$$k = \sqrt{3(1 - 2\nu_p)} \tag{5.23}$$

$$k = \sqrt{3(1 - 2\upsilon_p)} \tag{5.24}$$

The plastic strain, ϵ_{vol}^{plas} is given by,

$$\epsilon_{vol}^{plas} = \epsilon_{vol} - \epsilon_{vol}^{el} \tag{5.25}$$

where, ϵ_{vol} is the volumetric strain and ϵ_{vol}^{el} is the elastic strain. The elastic strain was taken as the strain at the yield stress of the structure. The material parameters for TSPU M0, M3, M7 and M12 are presented in Table 5.5. The

values for ν and ν_p are assumed through an iterative process in the model.

Table 5.5: Material properties for the crushable foam model (TSPUM0, M3, M7 and M12).

Material property	TSPU specimens			
	M0	M3	M7	M12
Elastic Modulus, E (MPa)	737.77	741.72	749.70	817.29
Poissons ratio, υ	0.3	0.25	0.2	0.15
Density, kg/m^3	1087	937.5	825	617
Compression yield stress ratio, k	1.449	1.500	1.549	1.732
Plastic Poissons ratio, υ_p	0.3	0.25	0.2	0.15

5.2.4 Modified 3D Hashin's failure criteria

ABAQUS (Standard/Explicit) consists of interfaces that enables one to implement general constitutive equations. In ABAQUS/Standard the user-defined material model is implemented in user subroutine UMAT and for ABAQUS/-Explicit the subroutine VUMAT is used. These subroutines are used when none of the existing material models that are included in the ABAQUS material library is capable of accurately representing the behaviour of the material to be modelled. This benefits the user as it makes it possible to define a desired constitutive model(s). A UMAT or VUMAT can be coded with programs such as FORTRAN or C. The keyword *DEPVAR is used to define the number of internal state variables for a user-defined material; all variables must be defined and initialised properly and enough storage space needs to be assigined for state variables with the *DEPVAR option.

A VUMAT subroutine that describes the constitutive response and failure model of a composite can been implemented with the use of the mathematical formulas. An Orthotropic elastic material model is usually used to describe the macroscopic constitutive response of an undamaged composite. Failure in a 3-D woven composite can be modeled with the use of a quadratic stress-based criteria [228]; these are a generalisation of the failure criteria proposed by Hashin [187]

for a unidirectional composite. However, it can be used to simulate the overall numerical response of the CFRP tube in a cylindrical co-ordinate system, i.e. r, θ and z. The four main fiber failure conditions are described as follows:

(a) Tensile fibre failure ($\sigma_{zz} > 0$),

$$\text{If } \left(\frac{\sigma_{zz}}{X_{zt}}\right)^2 + \left(\frac{\sigma_{zr}}{S_{zr}}\right)^2 + \left(\frac{\sigma_{z\theta}}{S_{z\theta}}\right)^2 = 1, \text{ then } d_{ft} = 1 \tag{5.26}$$

(b) Compressive fibre failure ($\sigma_{zz} < 0$),

$$\text{If } \frac{|\sigma_{zz}|}{X_{zc}} = 1, d_{fc} = 1, \text{ then } d_{fc} = 1 \tag{5.27}$$

(c) Tensile matrix failure ($\sigma_{rr} + \sigma_{\theta\theta}$),

$$\text{If } \frac{(\sigma_{rr} + \sigma_{\theta\theta})^2}{X_{rt}^2} + \frac{\sigma_{r\theta} - \sigma_{rr}\sigma_{\theta\theta}}{X_{r\theta}^2} + \frac{\sigma_z^2 + \sigma_{z\theta}^2}{X_{\theta r}} = 1, \text{ then } d_{mt} = 1 \tag{5.28}$$

(d) Compressive matrix failure ($\sigma_{rr} + \sigma_{\theta\theta} < 0$),

$$\text{If } \left[\left(\frac{X_{rc}}{2S_{r\theta}}\right)^2 - 1\right]\frac{\sigma_{rr} + \sigma_{\theta\theta}}{X_{rc}^2} + \frac{(\sigma_{rr} + \sigma_{\theta\theta})^2}{4S_{r\theta}^2} + \frac{\sigma_{r\theta}^2 - \sigma_{rr}\sigma_{\theta\theta}}{X_{r\theta}^2} + \frac{\sigma_{zr}^2 + \sigma_{z\theta}}{X_{rz}^2} = 1, \text{ then } d_{mc} = 1 \tag{5.29}$$

where X_{zt}, X_{zc}, X_{rt}, X_{rc}, S_{zr}, $S_{z\theta}$ and $S_{r\theta}$ are the strength components and d_{ft}, d_{fc}, d_{mt} and d_{mc} are damage variables that are associated with the four failure modes.

In order for one to take into account the through-the-thickness effects of the CFRP tube, the 3D material response needs to be considered, with the following stress-strain relations:

$$\sigma = C(d) \cdot \epsilon \tag{5.30}$$

i.e.

$$\begin{bmatrix} \sigma_{zz} \\ \sigma_{rr} \\ \sigma_{\theta\theta} \\ \sigma_{zr} \\ \sigma_{r\theta} \\ \sigma_{z\theta} \end{bmatrix} = \begin{bmatrix} C_{zz} & C_{zr} & C_{z\theta} & 0 & 0 & 0 \\ C_{rz} & C_{rr} & C_{r\theta} & 0 & 0 & 0 \\ C_{\theta z} & C_{\theta r} & C_{\theta\theta} & 0 & 0 & 0 \\ 0 & 0 & 0 & C_{44} & 0 & 0 \\ 0 & 0 & 0 & 0 & C_{55} & 0 \\ 0 & 0 & 0 & 0 & 0 & C_{66} \end{bmatrix} \begin{vmatrix} \epsilon_{zz} \\ \epsilon_{rr} \\ \epsilon_{\theta\theta} \\ \epsilon_{zr} \\ \epsilon_{r\theta} \\ \epsilon_{z\theta} \end{vmatrix} \tag{5.31}$$

where,

$$\begin{aligned} C_{zz} &= (1-d_f)E_{Yz}(1-\nu_{r\theta}\nu_{\theta r})\Gamma, \\ C_{rr} &= (1-d_f)(1-d_m)E_{Yr}(1-\nu_{z\theta}\nu_{\theta z})\Gamma, \\ C_{\theta\theta} &= (1-d_f)(1-d_m)E_{Y\theta}(1-\nu_{zr}\nu_{rz})\Gamma, \\ C_{zr} = C_{rz} &= (1-d_f)(1-d_m)E_{Yz}(\nu_{rz}+\nu_{\theta r}\nu_{r\theta})\Gamma, \\ C_{r\theta} = C_{\theta r} &= (1-d_f)(1-d_m)E_{Yr}(\nu_{\theta z}+\nu_{zr}\nu_{\theta z})\Gamma, \\ C_{\theta z} = C_{z\theta} &= (1-d_f)(1-d_m)E_{Yz}(\nu_{\theta z}+\nu_{rz}\nu_{\theta r})\Gamma, \\ C_{44} &= (1-d_f)(1-s_{mt}d_{mt})E_{Y1}(1-s_{mc}d_{mc})G_{zr}, \\ C_{55} &= (1-d_f)(1-s_{mt}d_{mt})E_{Y1}(1-s_{mc}d_{mc})G_{r\theta}, \\ C_{66} &= (1-d_f)(1-s_{mt}d_{mt})E_{Y1}(1-s_{mc}d_{mc})G_{z\theta}, \end{aligned} \tag{5.32}$$

where E_{Yz}, E_{Yr} and $E_{Y\theta}$ are the Young's moduli in the z, r and θ directions, respectively. G_{ij} is the shear modulus in the i-j plane and ν_{ij} (i,j = z, r, θ) is the Poisson's ratio for the transverse strain in the j-direction. s_{mt} and s_{mc} are terms that are introduced in order to control the reduction in shear stiffness resulting from tensile and compressive failure in the matrix, given as $s_{mt} = 0.9$ and $s_{mc} = 0.5$ [181].

Γ is defined as,

$$\Gamma = 1/(1 - \nu_{zr}\nu_{rz} - \nu_{r\theta}\nu_{\theta r} - \nu_{z\theta}\nu_{\theta z} - 2\nu_{rz}\nu_{\theta r}\nu_{r\theta}) \tag{5.33}$$

d_f and d_m are defined as,

$$d_f = 1 - (1 - d_{ft})(1 - d_{fc}) \tag{5.34}$$

$$d_m = 1 - (1 - d_{mt})(1 - d_{mc}) \tag{5.35}$$

The Young's moduli, shear moduli, Poisson's ratios and strengths of the CFRP composite are provided in Table 5.6. The Poisson's ratios as defined in Equation 5.36 need to be satisfied in order to ensure symmetry in the stiffness matrix,

$$\frac{\nu_{12}}{E_{Y1}} = \frac{\nu_{23}}{E_{Y2}}, \frac{\nu_{23}}{E_{Y2}} = \frac{\nu_{32}}{E_{Y3}}, \frac{\nu_{13}}{E_{Y1}} = \frac{\nu_{31}}{E_{Y3}} \tag{5.36}$$

Table 5.6: Summary of elasticity properties and the damage initiation data for the CFRP [229].

E_{Y1} (GPa)	E_{Y2} (GPa)	E_{Y3} (GPa)	ν_{12}	ν_{13}	ν_{23}
70	70	10	0.1	0.3	0.3
X_T (MPa)	X_C (MPa)	Y_T (MPa)	Y_C (MPa)	S_L (MPa)	S_T (MPa)
600	570	600	570	280	280
G_{12} (GPa)	G_{13} (GPa)	G_{23} (GPa)	$G_{ft} = G_{mt}$ (J/m^2)	$G_{fc} = G_{mc}$ (J/m^2)	
8.6	8.6	8.6	42700	44970	

5.3 Finite Element (FE) Modelling

This section will cover the FE modelling of quasi-static, LVI and blast simulations. With the use of material characterisation from experimental tests, one can use these characteristic to accurately simulate the progressive deformation with the implentation of the constitutive models as described in Section 5.2. Failure is simulated by the deletion of elements when a certain criteria is met. If a mesh is too coarse then the deletion of one element will remove a larger volume of the material; which leads to a unrealistic representation of practical applications.

5.3.1 Quasi-static modelling

TSPU and TPU

Quasi-static compression modelling was carried out for both the TPU and syntactic TSPU (graded and ungraded). The standard compression model for the TPU and TSPU is shown in Figure 5.2, in both cases the material was assumed to be isotropic. The TPU model uses the elasto-plastic constitutive model as described in Section 5.2.1, whereas the TSPU makes use of the crushable foam constitutive model as described in Section 5.2.3. A crushable foam model based on Deshpande and Fleck's work [227] was used for modelling the specimens. More specifically a Crushable foam with Isotropic Hardening (CIH) was used to define the strain hardening behaviour. The yield stress ratio, k, can be defined from the plastic Poisson's ratio, as shown in Equation 5.24, if hydrostatic data is not available [230]. In regards to the the graded structure, the finite element model was sectioned into four parts as shown in Figure 5.3, using the validated input parameters as established by the simulations carried out on the ungraded TSPU foams, i.e. M0, M3, M7 and M12.

Figure 5.2 illustrates the FE Model of the quasi-static simulation of both the TPU and TSPU, indicating mesh, boundary and loading conditions. The

dimensions of the specimens are identical to that of the the specimens used in the experiments with the height = 20 mm, length = 20 mm and width = 20 mm. The size of the mesh was set to 1 mm for the specimen. Additionally, 8-noded linear brick elements (C3D8R), with reduced integration and hourglass control, was used.

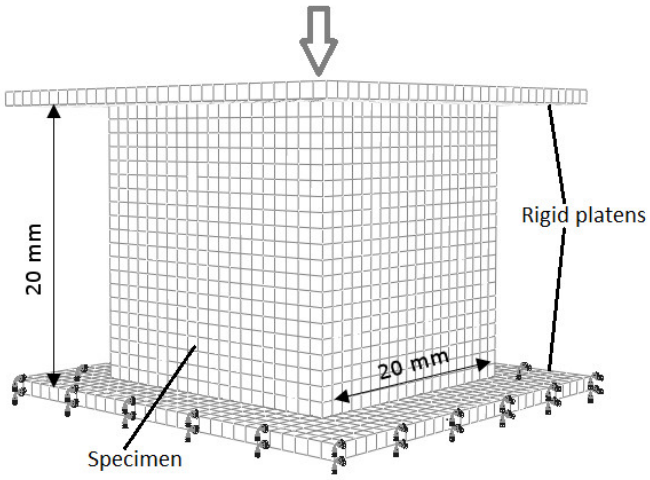

Figure 5.2: Compression model used for the TSPU and TPU validation in ABAQUS.

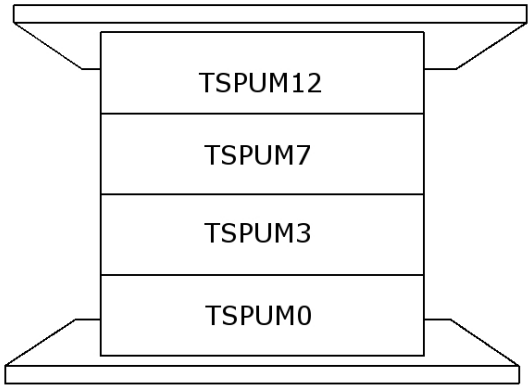

Figure 5.3: Compression model used for the graded TSPU in ABAQUS.

Further modelling was carried out on the TPU for validation purposes. These simulations were to be validated against the tensile tests using a tensile model, as shown in Figure 5.4.

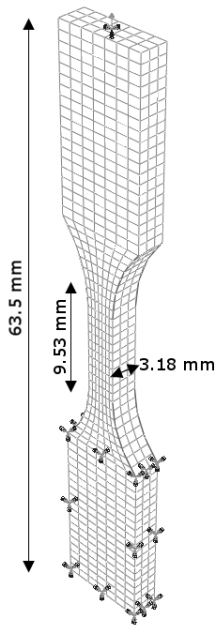

Figure 5.4: Tensile model used for TPU validation in ABAQUS.

CFRP tube

Due to the complex behaviour of composite materials, modelling the failure can be somewhat difficult due to the variation of fibres and matrices. ABAQUS enables the implementation of a 2D Hashin criteria, however since this only allows shell elements to be modelled it may not be very accurate. Therefore, a 3D modified Hashin criteria can be implemented for accuracy. The modelling will cover both aspects and a comparison between the accuracies will be highlighted. For the modelling of the 3D modified Hashin criteria a VUMAT subroutine [208] will be used as described in Section 5.2.4, whereas the 2D Hashin criteria will be implemented using the constitutive model available within ABAQUS.

Figure 5.5 shows the FE model used for the tube model within ABAQUS. The boundary conditions for the top platen are $U_x = U_y = UR_x = UR_y = 0; U_y \neq 0$. The peripheral edge of the panel is fixed, i.e. $U_x = U_y = U_z = 0$. The meshing consists of an C3D8R elements, which are eight-noded, linear hexahedral elements with reduced integration and hourglass control.

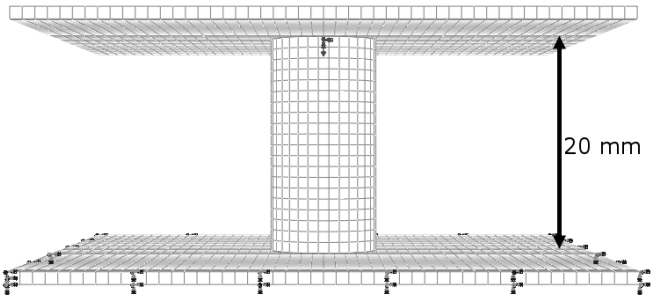

Figure 5.5: Loading and boundary conditions adopted in the finite element tube model.

5.4 Dynamic Modelling

Dynamic modelling was carried out on the TPU under LVI perforation with comparisons made against the AA 2024-T3. These simulations are carried out to provide validation to the constitutive models implemented for the TPU and AA 2024-T3, which can then be used for the blast loading conditions as part of a sandwich layup.

5.4.1 Low velocity perforation

For the LVI perforation model a fully clamped model was used for the perforation simulations of TPU and AA 2024-T3 using ABAQUS/Explicit. Although the panels are symmetric in nature, the expected output is asymmetric, therefore a full model was required. Figure 5.6 illustrates the geometric, boundary and loading conditions for the TPU sample. A similar model was adopted for the AA 2024-T3 sample, the only difference being the thickness of the plate, which was reduced from 2.9 mm to 1.2 mm. The hemi-spherical projectile has a mass of 3.4 kg, which is assumed to be a rigid body. The boundary conditions for the projectile are $U_x = U_y = UR_x = UR_y = 0; U_y \neq 0$. The peripheral edge of the panel is fixed i.e. $U_x = U_y = U_z = 0$. The meshing consists of an C3D8R elements, which are eight-noded, linear hexahedral elements with reduced integration and hourglass control.

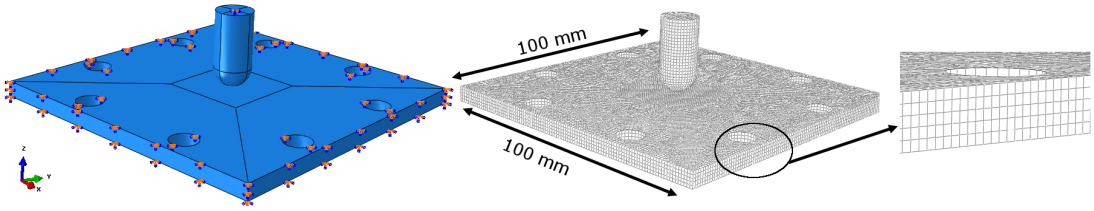

Figure 5.6: Geometry, mesh, boundary and loading conditions of the TPU perforation sample.

5.4.2 Blast modelling

As described in Section 2.2, the actual pressure-time loading associated with an explosion, is a complex decaying pressure oscillation that may require simplification for analysis involving blast loads to structures. Therefore, the simulation of the blast impulse on the panels was implemented using a triangular pressure pulse [195]. The time in this instance is identified once the intensity of the pressure pulse provided negligible contribution to the deformation of the panels. The pressure in this case was assumed to increase linearly up to the peak over a period of 180 µs and return back to zero [76].

The calculation time can be reduced by using the inherent symmetry of the problem. Therefore, only one quarter of the panel was modelled with appropriate boundary conditions applied along the planes of symmetry. The mesh, dimensions, loading (uniform) and boundary conditions are shown in Figure 5.7, for the panels with and without AA 2024-T3 skins. In all cases C3D8R elements, linear hexahedral elements with reduced integration and hourglass control. Mesh sensitivity studies were carried out to determine a 1 mm global element size, which demonstrated sufficient accuracy of the numerical results and mesh convergence rate. The pressure in this case was assumed to increase linearly up to the peak and return back to zero. The total time duration for the the simulations were taken as 1 ms, to allow any oscillations of the Lagrangian model to subside sufficiently.

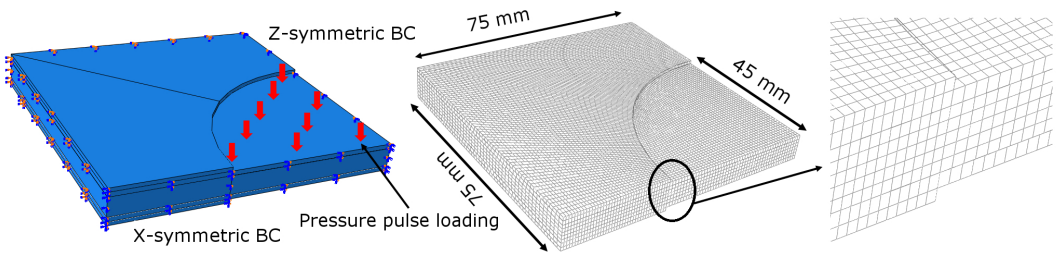

Figure 5.7: Dimensions, loading, boundary conditions and mesh generation of quarter model sandwich panel.

Modelling interaction

The interaction between elements of each layer is fundamental to the accuracy of the model. A general contact algorithm was used to define contact between the surfaces AA 2024-T3 skin and the TPU core. The general contact algorithm enables the use of element-based surfaces to model surface erosion during analyses - elements would be removed if the elements were to fail and interior faces that have been exposed to the blast pressure pulse would be activated. An element surface was created for the TPU and included in the general contact interaction. In order to maintain computational efficiency, elements in the vicinity of the blast load were only included in the element surface. Figure 5.8 illustrates a typical example of an eroding solid.

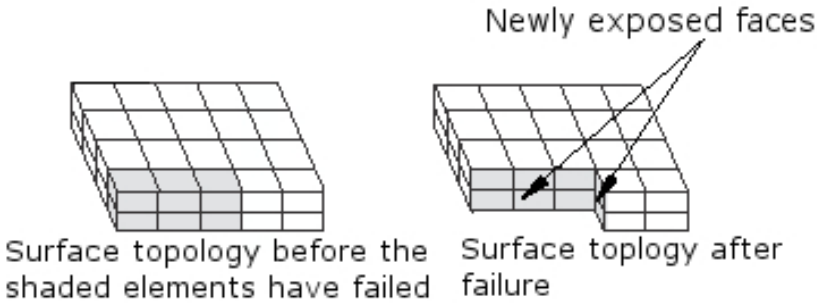

Figure 5.8: Toplogy of an eroding contact surface.

5.5 Finite Element Modelling Results and Discussion

To ensure the FE results are accurate, it is important to validate them against experimental results obtained in Chapter 4. Numerical solutions cover the individual syntactic foams which are used for the graded structure under quasi-static loading conditions. The CFRP tubes is modelled using a user defined 3D modifed hashin criteria with comparisons made against the in-built 2D Hashin constitutive model available in ABAQUS. Numerical results for the TPU under quasi-static compression and tension are also presented for validation purposes in order to simulate the perforation tests for the TPU and AA 2024-T3. Finally the TPU and AA 2024-T3, once validated, are used for the blast simulations of the sandwich panels.

5.5.1 Quasi-static simulation results

This section presents the quasi-static numerical results for the TSPU, TPU and CFRP. Firstly, the individual syntactic TSPU foams are presented followed by the graded foam, which has been layered to include the individual foams. A comparison between the CFRP tube using a 2D Hashin criteria available in ABAQUS and a user defined subroutine VUMAT for the modified 3D Hashin criteria. Finally, the TPU is modelled in uni-axial compression and tension for validation purposes in order to simulate the dynamic simulations, i.e. perforation and blast.

Thermosetting polyurethane (TSPU)

The simulation of a uni-axial compression test for TSPU M0, M3, M7 and M12 are shown in Figures 5.9 and the simulation output using the material parameters for the aforementioned foams as a basis for the graded foam simulations, i.e. G1 and G2, are also shown. These plots show the stress vs. strain traces

of the experimental and numerical response of the syntactic TSPU (graded and ungraded). The predicted stress-strain curves have a similar form to the experimental curve, where there is a steep rise in the elastic region followed by a stress plateau, which continues until the onset of densification.

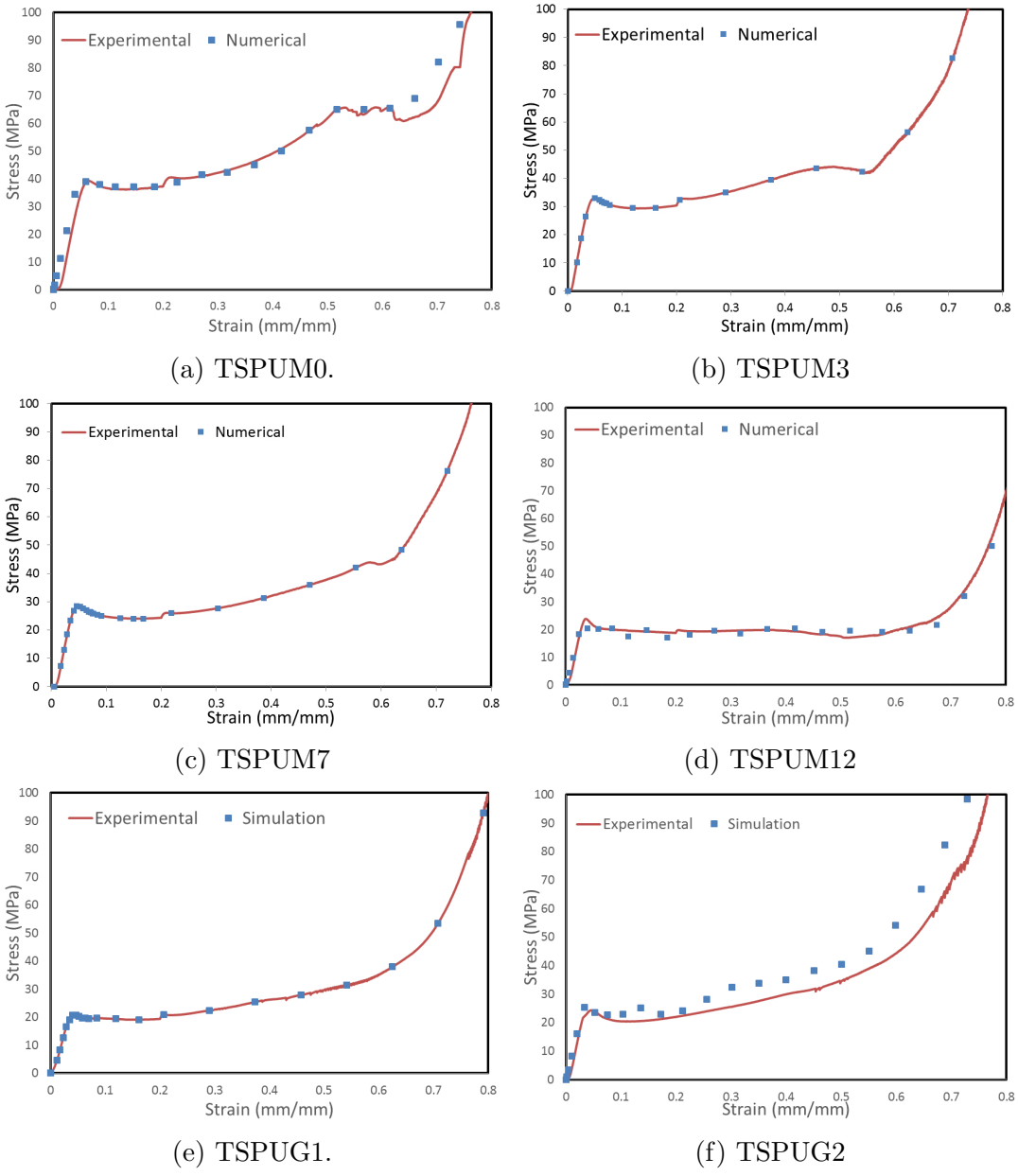

(a) TSPUM0.

(b) TSPUM3

(c) TSPUM7

(d) TSPUM12

(e) TSPUG1.

(f) TSPUG2

Figure 5.9: Stress vs. strain comparsion of the experimental and numerical of the TSPU M0, M3, M7, M12, G1 and G2 specimens.

Figure 5.10 shows the experimental and numerical deformation response of the graded foam (TSPUG1), which combines the responses of the individual

foams, i.e. M0, M3, M7 and M12, with similarities shown in the deformation response. The weaker and more brittle foam, i.e. TSPU M12, is the first to show deformation followed shortly by M7 and M3. This behaviour is consistent with the experimental work, whereby G1 demonstrates a more progressive failure mode with the foremost layer offering higher dampening properties, whereas the rearmost layer offers a higher compressive stiffness.

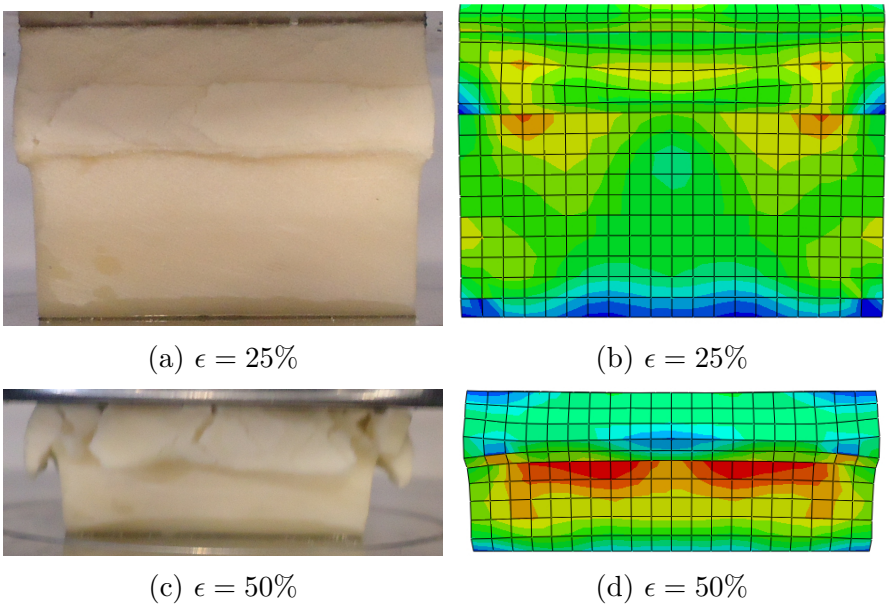

(a) $\epsilon = 25\%$ (b) $\epsilon = 25\%$

(c) $\epsilon = 50\%$ (d) $\epsilon = 50\%$

Figure 5.10: Experimental and numerical response of TSPUG1 under quasi-static loads at 25 and 50% strain (ϵ).

The FE models have captured the intial stiffness and peak load sufficiently. In all cases the plateau regions indicate a very good correlation where the strain-hardening and softening regions are sufficiently captured using the CIH model. A comparison between the experimental and numerical results is provided in Table 5.7, indicating negligible differences in plateau stresses (25 and 50 %) and the specific energy absorptions (SEA), whilst discrepancies were shown in the predicted plateau stress for G2. Similarly, the SEA values are below 5 % for all foams except for the G2 sample, which shows a difference of 6.87 %.

Table 5.7: Comparison of experimental and simulation results for the syntactic TSPU specimens (M0, M3, M7, M12, G1 and G2).

	Stress (MPa) $\epsilon = 25\%$	Stress (MPa) $\epsilon = 50\%$	SEA (kJ/kg)
		TSPUM0	
Exp	40.32	61.83	34.19
Sim	40.38	62.50	35.62
Difference (%)	0.15	1.08	4.10 %
		TSPUM3	
Exp	33.32	43.76	34.73
Sim	33.32	43.67	33.64
Difference (%)	0	-0.2	3.19 %
		TSPUM7	
Exp	26.21	37.74	32.92
Sim	26.22	37.74	34.21
Difference (%)	0.03	0	3.84 %
		TSPUM12	
Exp	17.89	20.12	29.42
Sim	19.35	19.52	30.50
Difference (%)	8.16	-2.98	3.61 %
		TSPUG1	
Exp	21.16	29.72	27.27
Sim	21.27	29.13	28.50 %
Difference (%)	0.52	-1.99	4.41 %
		TSPUG2	
Exp	23.78	34.48	33.41
Sim	28.23	40.46	35.79
Difference (%)	18.71	17.34	6.87 %

CFRP tube

Simulations were carried out on the CFRP tube utilising a 2D and 3D Hashin criteria with 2D shell and 3D solid elements, respectively. Figure 5.11 and 5.12 illustrates the deformation mechanisms experienced in the FE modelling simulation for both the 3D modified Hashin criteria and 2D Hashin criteria. Both models show the occurrence of element deletion, where the element deletion condition is satisfied at all of the section points of an element. In addition to this both models show a splaying mode.

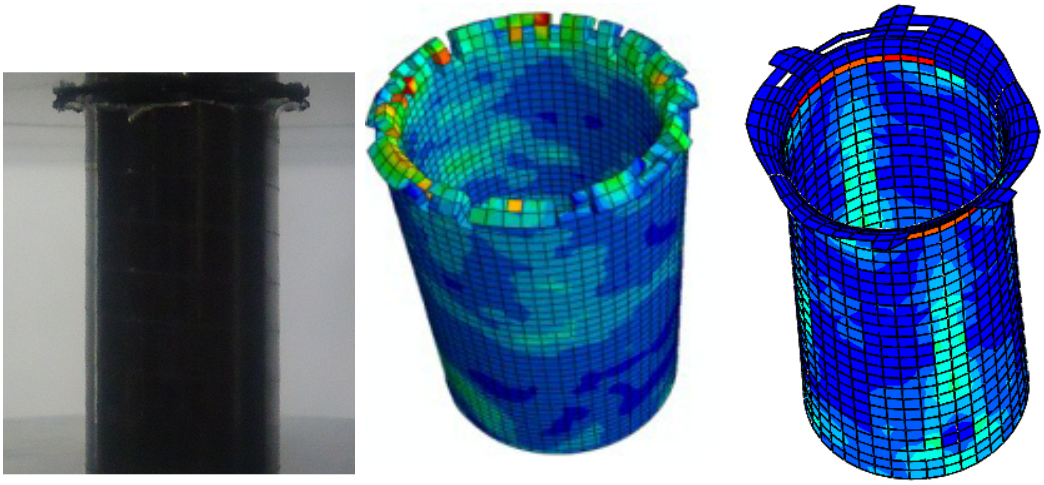

(a) Experimental (b) 3D solid (c) 2D shell

Figure 5.11: Experimental (Exp) vs. numerical (Sim) blast response.

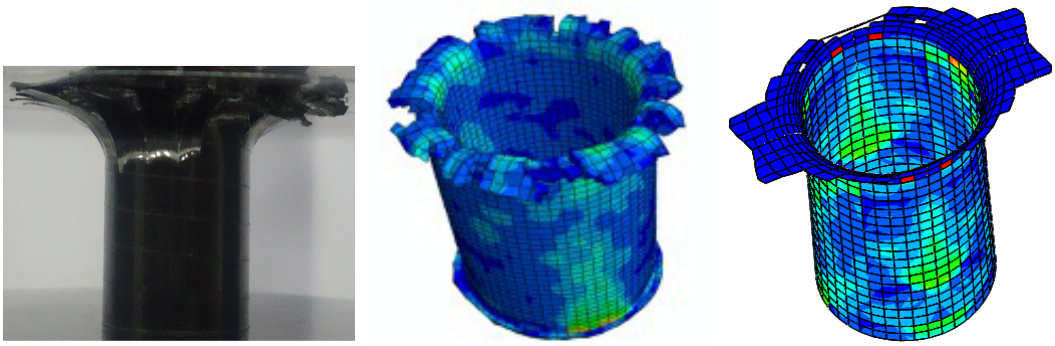

(a) Experimental (b) 3D solid (c) 2D shell

Figure 5.12: Experimental (Exp) vs. numerical (Sim) blast response.

There is also a clear distinction shown in the load displacement output, where higher fluctuations are observed with the 2D shell elements, as shown in Figure 5.13. The peak load response and plateau regions using the 3D element show a very good correlation unlike the 2D shell element model, which shows a significantly lower peak stress and a higher plateau response. The 3D elements present only minor errors of 3.72 and 3.92 % at 25 and 50 % plateau stresses, respectively.

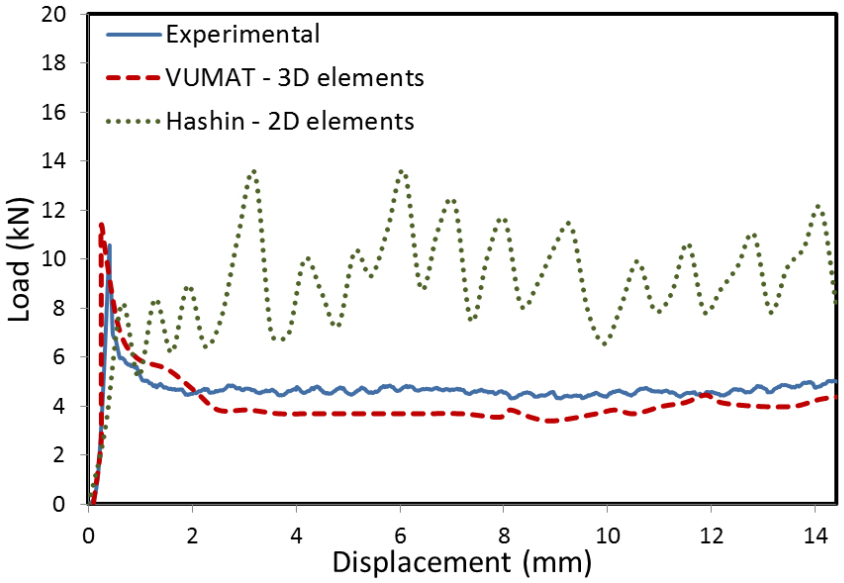

Figure 5.13: Load-displacement traces for experimental and numerical quasi-static compresion of CFRP tube, with comparisons between using the VUMAT subroutine and 2-D Hashin criteria.

Thermoplastic polyurethane (TPU)

Validation of the mechanical properties of the TPU in compressive and tensile loading were carried out prior to the dynamic perforation and blast simulations. Figure 5.14, which shows the load and displacement output, indicating good correlation for the TPU in compressive (5.14a) and tensile (5.14b) loading conditions within ABAQUS with negligible variations in the yield and plastic flow characteristics. The predicted fracture behaviour under tensile loading is consistent with the experimental work, where fracture initiated at a similar displacement, indicating that the elasto-plastic constitutive model is sufficient for the TPU material. With the validation of these material properties, these can then be used for parametric studies, in this case they will be applied to the low velocity perforation and the blast loading model.

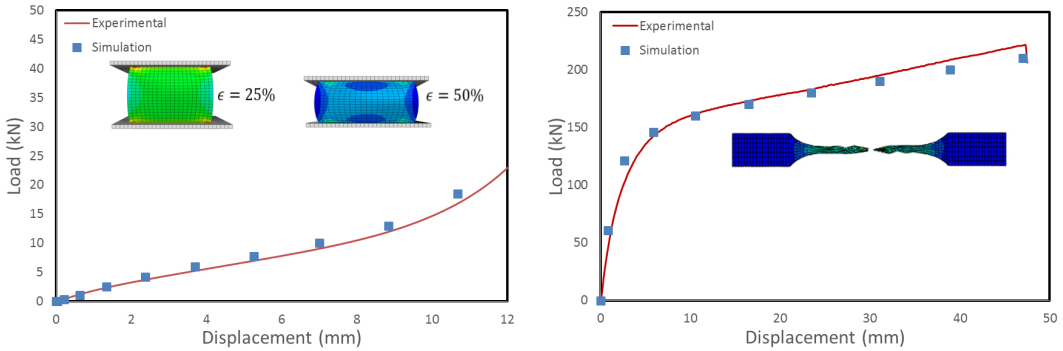

(a) Compression (b) Tensile

Figure 5.14: Experiment and numerical comparison of load vs. displacement for compression (a) and tensile models (b).

5.5.2 Dynamic simulation results

This section presents the dynamic numerical results for the TPU. Firstly, the perforation test carried out on the TPU and AA 2024-T3 are shown, which form the basis for validation to be used in the blast simulations. The blast simulations show the response of the plain TPU and sandwich TPU with AA 2024-T3 skins.

Low velocity perforation

The competiveness of TPU was assessed against an aluminium alloy (AA 2024-T3) under low velocity impact loading using a hemispherical nosed projectile. The fracture modes and deformation of both the TPU and AA 2024-T3 are now considered. The back face view of these materials, as shown in Figures 5.15 and 5.16, illustrate the final state of permanent deformation after low velocity perforation. The fractures developed during perforation are shown. For the TPU, according to phenomenological observations of the fracture after perforation tests, two main mechanisms can be observed in this study, i.e. ductile fracture due to nucleation, growth, and coalescence of voids as well as shear fracture due to shear band localisation. On the other hand, the numerical response of the AA 2024-T3 is characterised by a cap detachment at the tip of the projectile, as was the case for the experimental work.

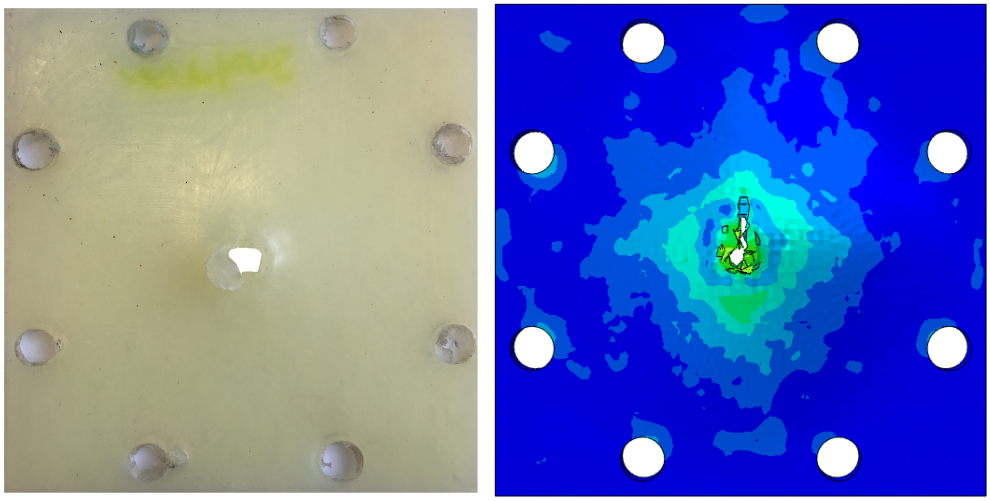

(a) Experimental (b) Numerical

Figure 5.15: Back face view of the penetrated TPU panel (a) experimental (b) numerical.

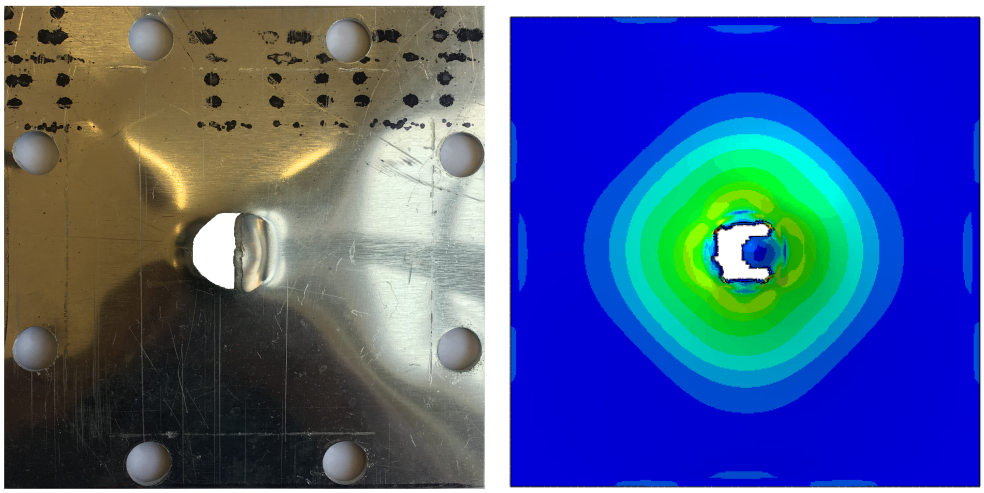

(a) Experimental (b) Numerical

Figure 5.16: Back face view of the penetrated AA 2024-T3 panel (a) experimental (b) numerical.

Figures 5.17 and 5.18 show the experimental and load-displacement traces for the TPU and AA 2024-T3 materials, respectively. An examination of the former figure for the TPU, indicates that the force has steadily increases to 2.5 kN, after which the sample fails, resulting in a sudden drop once the panel has been perforated. The peak force associated with fracture of the AA 2024-T3 skin is significantly higher (by a factor of approximately three) followed by rapidly

decreasing force values as the projectile perforates the panel. From a comparison of the experimental and predicted curves it is clear that the model captures all of the major features of the experimental load-displacement traces and are in good agreement, indicating that the constitutive models used for the simulations are both practical and reliable.

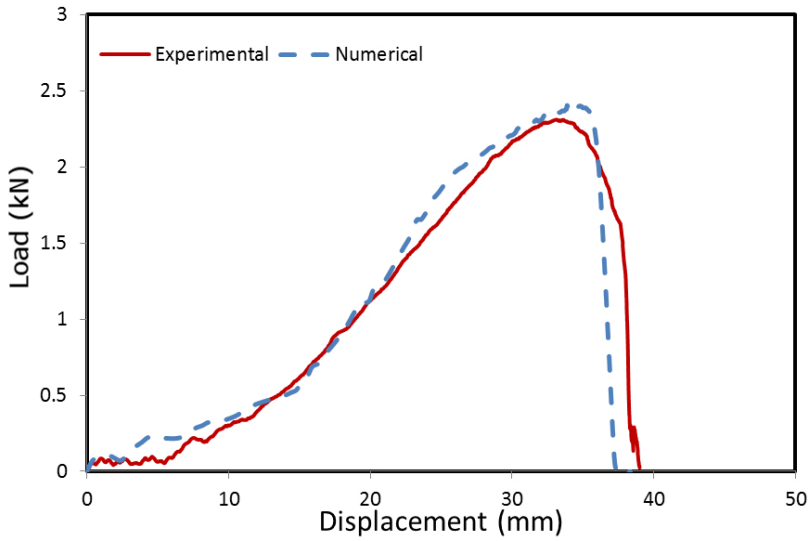

Figure 5.17: Back face view of the penetrated AA 2024-T3 panel (a) experimental (b) numerical.

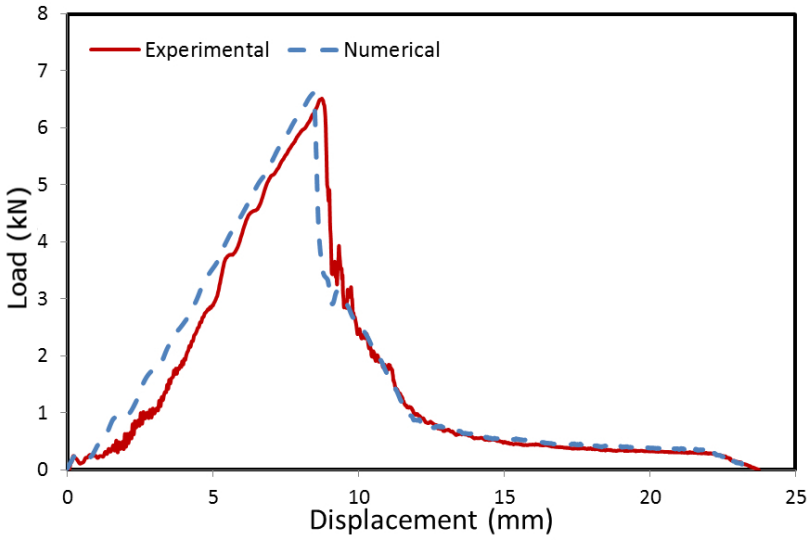

Figure 5.18: Load-displacement traces for experimental and numerical perforation of AA 2024-T3.

Blast simulation results and discussion

The blast simulations which were carried out using validated materials parameters for TPU and AA 2024-T3 were simulated using a simplified pressure pulse loading. The numerically predicted cross-section responses of the various panels following blast loading conditions, as shown in Figures 5.19 and 5.20, prove to be reasonably accurate. The deformation profiles indicate a very good correlation for the core of the TPU without skins as well as the TPU with AA 2024-T3 skins. The seperation of the TPU core and AA 2024-T3 skins (Figure 5.20) are consistent in all cases, where some rebound of the TPU was observed for the simulations, as was the case for the experiments.

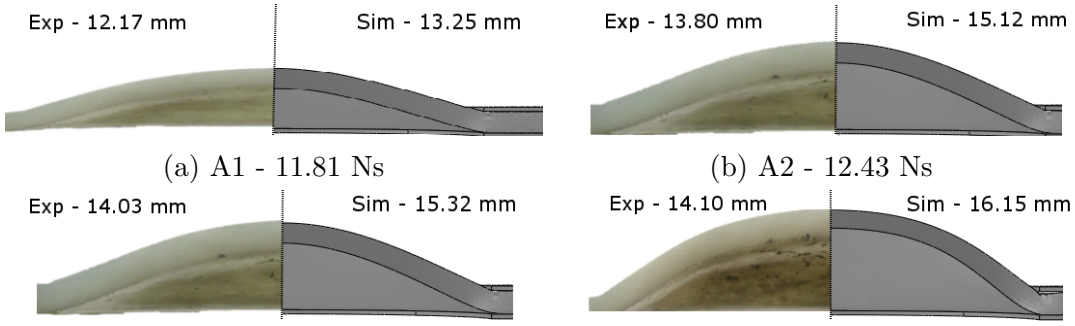

(a) A1 - 11.81 Ns (b) A2 - 12.43 Ns

(c) A3 - 13.09 Ns (d) A4 - 13.87 Ns

Figure 5.19: Experimental (Exp) vs. numerical (Sim) blast response.

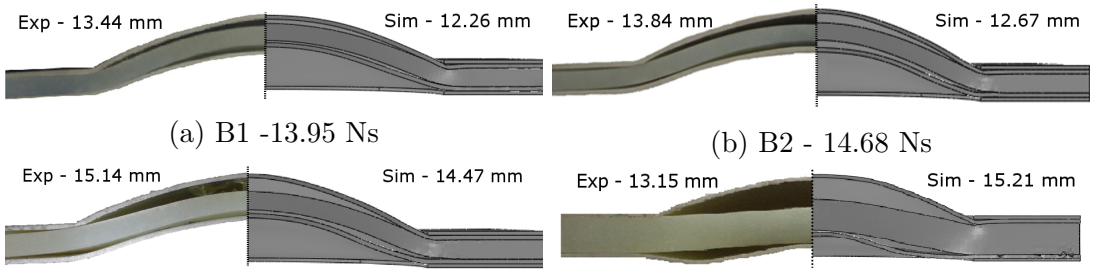

(a) B1 -13.95 Ns (b) B2 - 14.68 Ns

(c) B3 - 15.81 Ns (d) C1 - 14.35 Ns

Figure 5.20: Experimental (Exp) vs. numerical (Sim) blast response.

A more quantitative representation of the mid-point displacement is also presented, where small variations are observed for the mid-point displacements between the experimental and numerical responses of the panels; the differences

in midpoint deflections range from 4.5-14.5 %. Figure 5.21 shows the numerical response of specimen C3 (Figure 4.21). Here the impulse applied was increased in accordance with the experimentally recorded impulse to establish the tearing failure of the back face. It should be noted that in order to acheive this failure mode, a full model was necessary to allow for the asymmetric response of the back face.

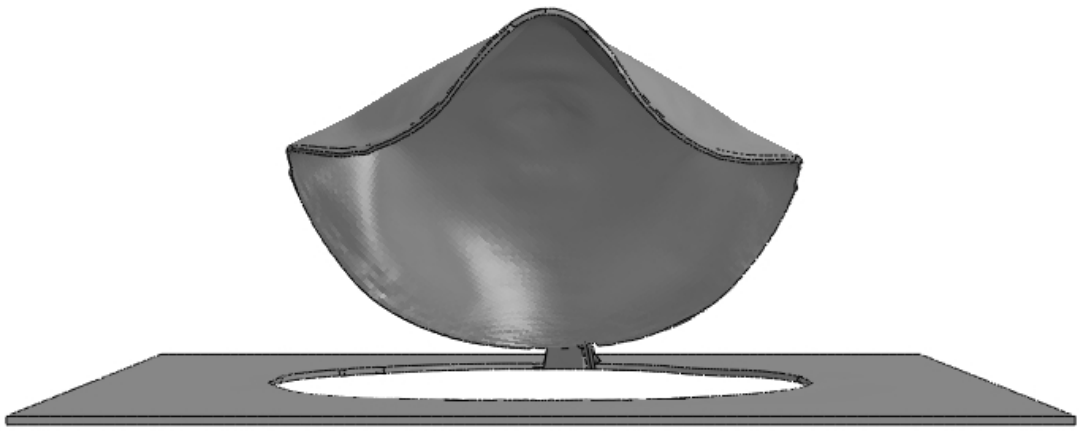

Figure 5.21: Numerical blast response of the back face tearing failure of specimen C3 (18.44 Ns) .

5.6 Summary of Finite Element Modelling

The construction of FE models and constitiutive relationships for the energy absorbing structures has been presented in this Chapter. Firstly, the constitutive models of the individual components has been presented, including elasto-plastic for the TPU, crushable foam for the TSPU, 2D and a user defined 3D Hashin's failure criteria for the CFRP tube, and a Johnson-Cook model for the aluminium alloy (AA) 2024-T3. Subsequently, the geometry, mesh generation, interaction, boundary and loading conditions for the FE models are also presented.

Numerical investigations of TSPU, CFRP tube and TPU have been presented. The numerical data are compared to corresponding experimental data in order to validate the finite element models, with good correlations. The individual syntactic TSPU foams showed excellent correlation which were then used for the graded foam, again with sufficiently accurate correlations.

The FE predictions for the TPU have been summarised and analysed to show the response of the TPU under dynamic perforation and blast loading. The models for the sandwich TPU with AA 2024-T3 were capable of predicting the deformation profiles and mid-point displacements of the sandwich panels, with small variations, ranging from 4.5-14.5%.

Chapter 6

Conclusions and Recommendations for Future Work

In this final chapter, a brief summary of the work carried out is present followed by conclusions of the major findings of the research work. From this, recommendations for future work are given.

6.1 General Summary

Sandwich structures have become increasing popular over many decades due to their energy absorbing capabilities for many structural applications. With the polyurethane (PU) industry rapidly expanding and the versatility of this material, this material was chosen to form the basis of the core material.

Syntactic foams are a type of composite material synthesised by filling a matrix, i.e. polymer, ceramic or metallic with hollow particles. The primary aim was to increase the energy absorbing capacity per unit mass of thermoset polyurethane (TSPU) using hollow glass microspheres (HGMs). This led to the development of a graded structure whereby, the aim was to introduce a more progressive response under dynamic loading conditions - reducing inertial effects. Carbon fibre reinforced polymer (CFRP) tube reinforcements are used for both the TSPU and thermoplastic polyurethane (TPU) to improve the specific energy absorption (SEA). Furthermore, split-Hopkinsons pressure bar (SHPB) tests are also carried out to observe the behaviour of the TSPU and TPU under high strain-rate loading ($> 10^3$ s^{-1}).

Further study is carried out to investigate the TPU under high-intensity impulse loading, i.e. air blast. Here, the structural response of the TPU panels, subjected to uniform loading is investigated using a ballistic pendulum. Work is extended to investigate the response of sandwich panels with aluminium alloy (AA 2024-T3) skins and the TPU as the core.

Using the experimental data, i.e. quasi-static and high strain rate characterisation, a number of simulations were carried out with the use of the commercial software ABAQUS. Finite element models are developed to simulate the quasi-static and dynamic response of the specimens. A crushable foam model is developed to model the overall response of the specimens, this was then validated against the experimental results. A vectorised user material subroutine (VU-

MAT) code using a modified 3D Hashin failure criteria, was also implemented to simulate the quasi-static crushing of the CFRP tube, with comparisons against using a 2D Hashin criteria. Finally, blast simulations are carried out by converting the explosive loading regime applied to the panels to a simplified pressure pulse loading, with comparisons made against experimental work.

6.2 Conclusions of Experimental and Numerical Work

The load bearing capacity of the CFRP tube reinforced syntactic TSPU foams was increased significantly relative to the unreinforced syntactic TSPU, where SEA increases as high as 48 % (56.28 kJ/kg) were noted. In addition, specific compressive strength (σ_c/ρ) increased by 65 % reaching 55 kPa/(kg/m^3). However, the post-yield behaviour under dynamic loading was reduced. The pure TSPU (no glass microspheres), for example, experienced stain-hardening under quasi-static loading, whereas under dynamic loading it exhibited a significant drop in the plateau stress. This behaviour was consistent with the syntactic foams (with glass microspheres).

Improvements in the plateau levels were made by introducing a graded structure, since it resulted in a more progressive response and a relatively constant stress level under dynamic loading. Furthermore, the SEA characteristics of TPU under dynamic loading was shown to increase with increasing impact energy, making them an attractive prospect to structural impact applications. The incorporation of CFRP tubes into the TPU greatly improved their properties and presents the reinforced TPU with greater energy absorbing characteristics under impact loading conditions. An additional study was carried out, where it is shown that the TPU offers a greater perforation resistance than aluminium alloy (AA) 2024-T3, with a similar mass per unit area, despite the yield strength of the AA

2024-T3 being an order of magnitude larger than that of TPU, illustrating the competitiveness and versatility of TPU under various loading conditions.

The numerical simulations of the quasi-static loading of the syntactic TSPU (graded and ungraded) indicated an excellent correlation using the crushable foam model. Using the individual material parameters of the syntactic TSPU, this was then applied to a graded structure with a similar type of deformation response under quasi-static loading. Furthermore, the CFRP tube response under similar loading was shown to be more accurate using a VUMAT rather than the in-built 2D Hashin criteria within ABAQUS.

The results of an investigation on the response of thermoplastic polyurethane (TPU) sandwich panels subjected to blast loading has been reported. TPU exhibited a strain-rate sensitivity under high strain-rate loading, as established by a series of SHPB tests, indicating significant strain energy potential under high strain-rate loading. The TSPU on the other hand, again showed a brittle response and was deemed not suitable for blast loading. The TPU under blast loading was also shown to withstand relatively high PE4 explosive masses (up to 11 grams), providing a lightweight and low cost alternative to various other materials. The addition of AA 2024-T3 skins as a basis of a sandwich construction provided additional resistance to impulsive loads. Increases in the blast resistance relative to the monolithic 5 mm TPU of 14.0, 23.8 and 71.2 % were observed with the addition of the skins and increases in the core thicknesses of 5, 10 and 20 mm, respectively.

A further study was carried out to simulate uniform blast loading on the TPU panels, where a Cowper-Symonds strain-rate hardening model was adopted for the TPU based on SHPB test data. Using a simplified pressure pulse loading, the simulated deformation profile response were shown to have very good correlation to the experimental data, with small variations in mid-point deflections. In order to achieve partial tearing failure of the back face of a panel, the numerical impulse

was increased relative to the experimentally recorded impulse to match the failure experienced in the experimental study.

6.3 Recommendations for Future Work

Future work on the syntactic foams, could include modifications of the size, wall thickness and/or type of microspheres. Further optimisation in the specific mechanical characteristics and improvements in the impact response can be made with further variations in the distribution of the microspheres in the form of a functionally graded foam.

Furthermore, this research exemplifies the versatility and toughness of TPU, with TPU offering a relatively high blast resistance at a fraction of the cost versus other materials. Since the ratio of hard and soft domains can be adjusted there is clearly scope for future work using this material. The presence of a multi-phase microstructure for TPUs, can show different extents of phase separation, offering new possibilities on tuning the polymeric matrix properties. This enables introduction of fillers, such as the incorporation of nano-material within the TPU matrix, and may form the basis for future work. In the case of dynamic loading scenarios, with the research undertaken in this study, it is recommended that the TPU is used as a base material for future designs of structures subject to severe dynamic loading conditions.

References

[1] Ceresana. Market Intelligence. Consulting. www.ceresana.com.

[2] J. Yi, M. C. Boyce, G. F. Lee, and E. Balizer. Large deformation rate-dependent stress-strain behaviour of polyurea and polyurethanes. *Polymer*, 47:319–329, 2006.

[3] V. M. R. Barros, A. L. Rosa, Màrcio M. Beloti, and Gilberto Chierice. In *vivo* biocompatibility of three different chemical compositions of *Ricinus communis* polyurethane. *Journal of Biomedical Materials Research*, 67:235–239, 2003.

[4] G. Wegner, M. Brandt, L. Duda, J. Hofmann, B. Klesczewski, D. Koch, R. J. Kumpf, H. Orzesek, H. G. Pirkl, C. Six, C. Steinlein, and M. Weisbeck. Trends in industrial catalysis in the polyurethane industry. *Journal of Oleo Science*, 221:303–335, 2001.

[5] W. K. Sakamoto, S. Shibatta-Kagesawa, D. H. F. Kanda, S. H. Fernandes, E. Longo, and G. O. Chierice. Piezoelectric effect in composite polyurethane ferroelectric ceramics. *Physica Status Solidi (a)*, 172:265–271, 1999.

[6] World Health Organisation. www.who.int/gho/road$_$safety/mortality/en/.

[7] Department for Transport. www.gov.uk/government/publications/annual-road-fatalities/history.

[8] S. Abrate. *Impact Engineering of Composite Structures.* SpringerWien, New York, 2011.

[9] R. Olsson. Mass criterion for wave controlled impact response of composite plates. *Composites: Part A*, 31:879–887, 2000.

[10] Fedral Aviation Administration. `www.faasafety.gov/`.

[11] R. A. Dolbeer, S. E. Wright, J. Weller, and M. J. Begier. Wildlife strikes to civil aircraft in the United States 1990-2013. FAA National Wildlife Strike Database, Serial Report Number 20, July, 2014.

[12] S. Heimbs. Computational methods for bird strike simulations: a review. *Computers and Structures*, 89:2093–2112, 2011.

[13] S. Heimbs, S. Lang, and H. Havar. Rim release analysis: impact of aircraft wheel flange fragment on wing flap mechanism. *In: Structures Under Shock and Impact XII, N. Jones, C. A. Brebbia, WIT Press*, 2012.

[14] S. Heimbs. Energy absorption in aircraft structures. Presented at the first International Workshop on Hydraulic Equipment and Support Systems for Mining, 2012.

[15] P. D. Smith and J. G. Hetherington. *Blast and Ballistic Loading of Structures.* Butterworth Heinemann, Oxford, 1994.

[16] G. K. Schleyer. Predicting the effects of blast loading arising from a pressure vessel failure: a review. *Proceedings of the Institution of Mechanical Engineers*, 218:181–190, 2004.

[17] M. C. Simmons and G. K. Schleyer. Pulse pressure loading of aircraft structural panels. *Thin Walled Structures*, 44:496 506, 2006.

[18] P. W. Cooper. *Explosives Engineering.* Wiley-VCH, New York, 1996.

[19] United States Department of State - office of the coordinator for counterterrorism. Country Reports on Terrorism, 2015.

[20] W. Fairbairn. An Account of the Construction of the Britannia and Conway Tubular Bridges, John Weale, London, 1849.

[21] G. N. Nurick, G. S. Langdon, Y. Chi, and N. Jacob. Behaviour of sandwich panels subjected to intense air blast - Part 1: Experiments. *Composite Structures*, 91:443–441, 2009.

[22] M. I. Idris, T. Vodenitcharova, and M. Hoffman. Mechanical behaviour and energy absorption of closed-cell aluminium foam panels in uniaxial compression. *Materials Science and Engineering A*, 517:37–45, 2009.

[23] M. Z. Hassan and W. J. Cantwell. The influence of core properties on the perforation resistance of sandwich structures - an experimental study. *Composites: Part B*, 43:3231–3238, 2012.

[24] C. Qi, S. Yang, L. J. Yang, Z. Y. Wei, and Z. H. Lu. Blast resistance and multi-objective optimization of aluminum foam-cored sandwich panels. *Composite Structures*, 105:45–57, 2013.

[25] A. Jung, E. Lach, and S. Diebels. New hybrid foam materials for impact protection. *International Journal of Impact Engineering*, 64:30–38, 2014.

[26] T. Boonkong, Y. O. Shen, Z. Guan, and W. J. Cantwell. The low velocity impact response of curvilinear-core sandwich structures. *International Journal of Impact Engineering*, 93:28–38, 2016.

[27] M. Smith, W. J. Cantwell, Z. Guan, S. Tsopanos, M. D. Theobald, G. N. Nurick, and G. S. Langdon. The quasi-static and blast response of steel lattice structures. *Journal of Sandwich Structures and Materials*, 13:479–501, 2010.

[28] G. S. Langdon, W. J. Cantwell, Z. W. Guan, and G. N. Nurick. The response of polymeric composite structures to air-blast: a state-of-the-art. *International Materials Reviews*, 59:159–177, 2014.

[29] V. S. Deshpande and N. A. Fleck. Multi-axial yield behaviour of polymer foams. *Acta Materialia*, 49:1859–1866, 2001.

[30] H. Hamada and S. Ramakrishna. Effect of Fiber Material on the Energy Absorption Behaviour of Thermoplastic Composite Tubes. *Journal of Thermoplasic Composite materials*, 9:259–279, 1996.

[31] D. Hull. Unified approach to progressive crushing of fibre reinforced composite tubes. *Composite Science and Technology*, 40:377–421, 1991.

[32] D. Hull. Energy absorbing composite structures. *Science and Technology Review*, 3:23–30, 1988.

[33] S. Ramakrishna and D. Hull. Energy Absorbing Capability of Epoxy Composite Tubes with Knitted Carbon Fiber Fabric Reinforcement. *Composites Science and Technology*, 49:349–356, 1993.

[34] F. Tarlochan, A.M.S. Hamouda, E. Mahdi, and B.B. Sahari. Composite sandwich structures for crashworthiness applications. *Journal of Materials Design and Applications*, 221:121–130, 2007.

[35] P. D. Bois, C. C. Chou, B. B. Fileta, T. B. Khalil, A. I. King, H. F. Mahmood, H. J. Mertz, and J. Wismans. Vehicle crashworthiness and occupant protection, Automotive Applications Committee American Iron and Steel Institute Southfield, Michigan, 2004.

[36] R. Feynman. The Feynman Lectures on Physics Vol I. Addison Wesley. ISBN 978-0-201-02115-8, 1970.

[37] L. J. Gibson and M. F. Ashby. *Cellular solids: structure and properties*. Cambridge University Press, 2nd edition, 1997.

[38] F. Laurin and A. J. Vizzini. Energy absorption of sandwich panels with composite-reinforced foam core. *Journal of Sandwich Structures and Materials*, 7:113–132, 2005.

[39] J. Banhart. Manufacture, characterisation and application of cellular metals and metal foams. *Progress in Materials Science*, 46:559–632, 2001.

[40] M. S. Found, A. M. Robinson, and J. J. Carruthers. The influence of FRP inserts on the energy absorption of a foam-cored sandwich panel. *Composite Structures*, 38, 1997.

[41] B. Jiang, F. Zhu, X. Jin, L. Cao, and K. H. Yang. Computational modelling of the crushing behaviour of SKYDEX material using homogenized material laws. *Composite Structures*, 106:306–316, 2013.

[42] Q. M. Li, I. Magkiriadis, and J. J. Harrigan. Compressive strain at the onset of densification of cellular solids. *Journal of Cellular Plastics*, 42:371–392, 2006.

[43] F. Ashby, A. Evans, L. Gibson, J. Hutchinson, and H. Wadley. *Metal Foams: A Design Guide*. Butterworth-Heinemann, Oxford, UK, 2000.

[44] M. A. Meyers. Dynamic behavior of materials,Wiley, New York, 1994.

[45] A. Altunc, J. Kim, Al-Haik, and M. R. Taha. Reliability-based design of blast-resistant composite laminates incorporating carbon nanotubes. *Composite Structures*, 93:2042–2048, 2011.

[46] Headquarters Departments of the US Army TM5-1300. Structures to resist the effects of accidental explosions, November 1990.

[47] B. Hopkinson. A method of measuring the pressure produced in the detonation of high explosives or by the impact of bullets. *Proceedings of the Royal Society A: Mathematical, Physical and Engineering Sciences*, 89:411–413, 1914.

[48] G. Gary and D. Mohr. Modified kolsky formulas for and increased measurement duration of SHPB systems. *Experimental Mechanics*, 53:713–717, 2013.

[49] J. Harding, E. O. Wood, and J. D. Campbell. Tensile testing of materials at impact rate of strain. *Mechanical Engineering Science*, 2:88–96, 1960.

[50] J. Duffy, J. D. Campbell, and R. H. Hawley. On the use of a torsional split hopkinson bar to study rate effects in 1100-0 aluminium. *Applied Mechanics*, 38:83–91, 1960.

[51] J. Park and H. J. Choi. Experiments and numerical analyses of HB400 and aluminum foam sandwich structure under landmine explosion. *Composite Structures*, 134:726–739, 2015.

[52] S.N. Raman, T. Ngo, and P. Mendis. A Review on the Use of Polymeric Coatings for Retrofitting of Structural Elements against Blast Effects. *Electronic Journal of Structural Engineering*, 11:464–477, 2011.

[53] M. Y. Yahya. *The blast response of fibre reinforced composites and sandwich structures*. PhD thesis, Department of Engineering, University of Liverpool, 2008.

[54] S. Guruprasad and A. Mukherjeed. Layered Sacrifical claddings under blast loading Part I- Analytical studies. *International Journal of Impact Engineering*, 24:957–973, 2000.

[55] S. Guruprasad and A. Mukherjeed. Layered sacrificial claddings under blast loading Part II- Experimental studies. *International Journal of Impact Engineering*, 24:975–984, 2000.

[56] A. G. Hanssen, L. Enstock, and M. Langseth. Close-range blast loading of aluminium foam panels. *International Journal of Impact Engineering*, 27:593–618, 2002.

[57] K. Friedrich and A. A. Almajid. Manufacturing aspects of advanced polymer composites for automotive applications. *Applied Composite Materials*, 20:107–128, 2013.

[58] A. K. Noor, W. S.Burton, and C. W. Bert. Computational models for sandwich panels and shells. *Applied Mechanics Reviews*, 49:155–199, 1996.

[59] P. M. Schubel, J-J. Luo, and I. M. Daniel. Low velocity impact behavior of composite sandwich panels. *Composites Part A: Applied Science and Manufacturing*, 36:1389–1396, 2005.

[60] I. M. Daniel P. M. Schubel, J-J. Luo. Impact and post impact behavior of composite sandwich panels. *Composites Part A: Applied Science and Manufacturing*, 38:1051–1057, 2007.

[61] M.V. Hosur, A. A. Mohammed, S. Zainuddin, and S. Jeelani. Processing of nanoclay filled sandwich composites and their response to low-velocity impact loading. *Composite Structures*, 82:101–116, 2008.

[62] W. J. Cantwell, H. Kiratisaevee, and M. A. Hazizan. Impact loading of lightweight structures. *International Journal of Impact Engineering*, 35:61–63, 2008.

[63] F. Xia and X. Wu. Work on impact properties of foam sandwich composites with different structure. *Journal of Sandwich Structures and Materials*, 12:47–62, 2010.

[64] J. Zhou, Z. Guan, and W. J. Cantwell. The impact response of graded foam sandwich structures. *Composite Structures*, 97:370–377, 2013.

[65] A. K. J. Al-Shamary AND R. Karakuzu AND O. Okan Özdemir. Low-velocity impact response of sandwich composites with different foam core configurations. *Journal of Sandwich Structures and Material*, 18:754768, 2016.

[66] W. Hou, F. Zhu, G. LU, and D-N. Fang. Ballistic impact experiments of metallic sandwich panels with aluminium foam core. *International Journal of Impact Engineering*, 37:1045–1055, 2010.

[67] N. A. Rahman, S. Abdullah, W. F. H. Zamri, M. F. Abdullah, M. Z. Omar, and Z. Sajuri. Ballistic Limit of High-Strength Steel and Al7075-T6 Multi-Layered Plates Under 7.62-mm Armour Piercing Projectile Impact. *Latin Americal Journal of Solids and Structures*, 13:1658–1676, 2016.

[68] M. Xu, G. Huang, S. Feng, X. Qin, G. J. McShane, and W. J. Stronge. Perforation resistance of aluminum/polyethylene sandwich structure. *Materials and Design*, 100:92–101, 2016.

[69] A. A. Nia, H. Ranjbarzadeh, and M. Kazemii. An Empirical Study on Ballistic Resistance of Sandwich Targets with Aluminum Facesheets and Composite Core. *Latin Americal Journal of Solids and Structures*, 14:1085–1105, 2017.

[70] G. S. Langdon, W. J. Cantwell, and G. N. Nurick. The blast response of novel thermoplastic-based fibre-metal laminates - some preliminary results and observations. *Composites Science and Technology*, 65:861–872, 2005.

[71] Y. A. Bahei-El-Din and G. J. Dvorak. Behavior of sandwich plates reinforced with polyurethane/polyurea interlayers under blast loads. *Journal of Sandwich Structures and Materials*, 9:261–281, 2007.

[72] E. Wang, N. Gardner, and A. Shukla. The blast resistance of sandwich composites with stepwise graded cores. *International Journal of Solids and Structures*, 46:3492–3502, 2009.

[73] M. Z. Hassan, Z. W. Guan, W. J. Cantwell, G. S. Langdon, and G. N. Langdon. The influence of core density on the blast resistance of foam-based sandwich structures. *International Journal of Impact Engineering*, 50:9–16, 2012.

[74] M. S. H. Fatt, Y. Gao, and D. Sirivolu. Foam-core, curved composite sandwich panels under blast. *Journal of Sandwich Structures and Materials*, 15:261–291, 2013.

[75] J. Sousa-Matrins, D. Kakogiannis, F. Coghe, B. Reymen, and F. Teixeira-Dias. Behaviour of sandwich structures with cork compound cores subjected to blast waves. *Engineering Structures*, 46:140–146, 2013.

[76] Z. W. Guan, A. Aktas, P. Potluri, W.J. Cantwell, G. Langdon, and G.N. Nurick. The blast resistance of stitched sandwich panels. *International Journal of Impact Engineering*, 65:137–145, 2014.

[77] M. Altenaiji, Z. W. Guan, W. J. Cantwell, Y. Zhao, and G. K. Schleyer. Characterisation of aluminium matrix syntacic foams under drop weight impact. *Materials and Design*, 59:296–302, 2014.

[78] V. Leisis P. Griskevicius, D. Zeleniakiene and M. Ostrowski. Experimental and numerical study of impact energy absorption of safety important honeycomb core sandwich structures. *Material Science*, 16:119–123, 2010.

[79] L. Torre and J. Kenny. Impact testing and simulation of composite sandwich structures for civil transportation. *Composite Structures*, 50:257–267, 2000.

[80] L. Karger, J. Baaran, and J. Tebmer. Rapid simulation of impacts on composite sandwich panels inducing barely visible damage composite structures. *Composite Structures*, 79:527–534, 2007.

[81] H. Su, S. M. Asce, J. Mcconnel, and A. M. Asce. Influences of Material Properties on Energy Absorption of Composite Sandwich Panels under Blast Loads. *Journal of Composites for Construction*, 16:464–477, 2012.

[82] G. Zhou, M. Hill, and M. Langseth. Investigation of parameters governing the damage and energy absorption characteristics of honeycomb sandwich panels. *Journal of Sandwich Structures and Materials*, 9:309–342, 2007.

[83] L. B. Vogelesang and A. Vlot. Development of fibre metal laminates for advanced aerospace structures. *Journal of Materials Processing Technology*, 103:1–5, 2000.

[84] P. Compston and W. J. Cantwell. Impact perforation resistance and fracture mechanisms of a thermoplastic based fiber-metal laminate. *Journal of Material Science Letters*, 20:597–599, 2001.

[85] G. R. Villanueva and W. J. Cantwell. The high velocity impact response of composite and FML-reinforced sandwich structures. *Composites Science Technology*, 64:35–54, 2004.

[86] G. S. Langdon, S. L. Lemanski, G. N. Nurick, M. C. Simmons, W. J. Cantwell, and G. K. Schleyer. Behaviour of fibre-metal laminates subjected to localised blast loading: Part I - Experimental observations. *International Journal of Impact Engineering*, 34:1202–1222, 2007.

[87] G. S. Langdon, S. L. Lemanski, G. N. Nurick, M. C. Simmons, W. J. Cantwell, and G. K. Schleyer. Failure characterisation of blast-loaded fibre-metal laminate panels based on aluminium and glass-fibre reinforced polypropylene. *Composites Science Technology*, 67:1385–1405, 2007.

[88] S. L. Lemanski, G. N. Nurick, G. S. Langdon, M. C. Simmons, W. J. Cantwell, and G. K. Schleyer. Behaviour of fibre metal laminates subjected to localised blast loading - Part II: Quantitative analysis. *International Journal of Impact Engineering*, 34:1223–1245, 2007.

[89] T. P. Vo, Z. W. Guan, W. J. Cantwell, and G. K. Schleyer. Modelling of the low-impulse blast behaviour of fibre-metal laminates subjected to localised blast loading. *International Journal of Impact Engineering*, 34:1202–1222, 2013.

[90] G. R. Villanueva. *Processing and Characterisation of the Mechanical Porperties of Novel Fibre-Metal Laminates*. PhD thesis, Department of Engineering, University of Liverpool, 2002.

[91] H. J. Fleisher. Design and explosive testing of a blast resistant luggage-container. *Structures under Shock and Impact Conference*, 1996.

[92] G. S. Langdon, W. J. Cantwell, and G. N. Nurick. The response of fibre metal laminate panels subjected to uniformly distributed blast loading. *European Journal of Mechanicals A/Solids*, 27:107–115, 2008.

[93] G. V. Reyes and W. J. Cantwell. The mechanical properties of fibre-metal laminates based on glass fibre reinforced polypropylene. *Composites Science and Technology*, 60:1085–1094, 2000.

[94] K. Mimura T. Umeda and T. Morisaka. Study of energy absorption efficiency for a few thin-walled tubes in axial crushing. *Journal of Solid Mechanics and Materials Engineering*, 4:875–890, 2010.

[95] X. F. Tao and Y. Y. Zhao. Compressive behavior of al matrix syntactic foams toughened with al particles. *Scripta Materialia*, 61:461–464, 2009.

[96] S. Ochelski, P. Kiczko, and A. Static. Axial crush performance of unfilled and foam-filled composite tubes. *Bulletin of the Polish Academy of Sciences: Technical Sciences*, 60:31–35, 2012.

[97] R. A. Alia, W. J. Cantwell, G. S. Langdon, S. C. K. Yuen, and G. N. Nurick. The energy-absorbing characteristics of composite tube-reinforced foam structures. *Composites: Part B*, 61:127–135, 2014.

[98] M. Y. M Zuhri, Z. W. Guan, and W. J. Cantwell. The mechanical properties of natual fibre based honeycomb core materials. *Composites: Part B*, 58:1–9, 2014.

[99] F. Coghe B. Reymen J. S. Martins, D. Kakogiannis and F. Teixeira-Dias. Behaviour of sandwich structures with cork compound cores subjected to blast waves. *Engineering Structures*, 46:140–146, 2013.

[100] F. Zhu, G. Lu, D. Ruan, and Z. Wang. Plastic deformation, failure and energy absorption of sandwich structures with metallic cellular cores. *International Journal of Protective Structures*, 1:507–541, 2010.

[101] H. P. Degischer and B. Kriszt. *Handbook of Cellular Metals: Production, Processing, Applications*. Weinheim:Wiley-VCH, 2002.

[102] V. S. Deshpande and N. A. Fleck. Energy absorption of an egg-box material. *Journal of the Mechanics and Physics of Solids.*, 51:187–208, 2003.

[103] I. Mohagheghian, G. McShane, and W. Stronge. Impact perforation of monolithic polyethylene plates: Projectile nose shape dependence. *International Journal of Impact Engineering*, 80:162–176, 2015.

[104] CES EduPack. Cambridge UK: Granta design limited, 2016.

[105] O. Bayer. Das Di-Isocyanat-Polyadditionsverfahren (Polyurethane). *Angewandte Chemie*, 59:252–272, 1947.

[106] C. Hepburn. *Polyurethane Elastomers*. Elsevier, London, New York, 1991.

[107] G. Oertel and L. Abele. *Polyurethane Handbook: Chemistry, Raw Materials, Processing, Application, Properties*. Hanser/Gardner, Munich, New York, Cincinnati, 2nd edition, 1994.

[108] F. Gao. *Advances in Polymer Nanocomposites: Types and Applications*. Woodhead Publishing, 2012.

[109] H. Ousji, B. Belkassem, M. A. Louar, B. Reymen, J. Martino, D. Lecompte, L. Ply, and J. Vantommea. Air-blast response of sacrificial cladding using low density foams: Experimental and analytical approach. *International Journal ofMechanical Sciences*, 128-129:459–474, 2017.

[110] M. V. Uspenskaya, N. V. Sitrotinkin, S. V. Yatsenko, and I. V. Masik. Formulations based on hollow glass spheres and polyurethane foams. *Russian Journal of Applied Chemistry*, 78:830–833, 2005.

[111] C. M. Roland, C. M. Twigg, Y. Vu, and P. H. Mott. High Strain rate mechanical behaviour of polyurea. *Polymer*, 48:574–578, 2007.

[112] S. S. Sarva, S. Deschanel, M. C. Boyce, and W. Chen. Stress-Strain Behaviour of a Polyurea and a Polyurethane from Low to High Strain Rates. *Polymer*, 48:2208–2213, 2007.

[113] J. Yi, M. C. Boyce, G. F. Lee, and E. Balizer. Rate-Dependent Stress-Strain Behaviour of Polyurea and Polyurethanes. *Polymer*, 47:319–329, 2006.

[114] S. Cruz and J. Viana. Structure-Properties Relationships in Thermoplastic Polyurethane Elastomer Nanocomposites: Interactions between Poly-

mer Phases and Nanofillers. *Macromolecular Materials and Engineering*, 300:1153–1162, 2015.

[115] T. Sui, N. Baimpas, P. I. Dolbnya, C. Prisacariu, and M. A. Korsunsky. Multiple-length-scale deformation analysis in a thermoplastic polyurethane. *Nature Communications*, 6:1–9, 2015.

[116] C. B. Wang and S. L. Cooper. Morphology and properties of segmented polyether polyurethaneureas. *Macromolecules*, 16:775–786, 1983.

[117] B. X. Fu, B. S. Hsiao, S. Pagola, P. Stephens, H. White, M. Rafailovich, J. Sokolov, P. T. Mather, H. G. Jeon, S. Phillips, J. Lichtenhan, and J. Schwab. Structural development of polyurethane containing polyhedral oligomeric silsesquioxanes (POSS) molecules. *Polymers*, 42:599–611, 2015.

[118] I. S. Fahim, W. Mamdouh, and H. A. G. Salem. A nanoscale investigation of mechanical, thermal stability and electrical conductivity properties of reinforced thermoplastic polyurethane/graphene nanocomposite. *American Journal of Nanoscience and Nanotechnology*, 1:31–40, 2013.

[119] Y. A. Bahei-El-Din and G. J. Dvorak. Enhancement of blast resistance of sandwich plates. *Composites Part B: Engineering*, 39:120–127, 2008.

[120] TPU Thermoplastic Polyurethane. `/www.plastichem.co.za/products/plastics/item/36-tpu-desmopan`.

[121] P. H. Mott, M. C. Roland, and R. D. Corsaro. Acoustic and dynamic mechanical properties of a polyurethane rubber. *The Journal of the Acoustical Society of America*, 111:1782–1790, 2002.

[122] V. V. Budov. Hollow glass microspheres. *Glass and Ceramics*, 51:230–235, 1994.

[123] I. D. Simonov-Emel'yanov and L.B. Kandyrin. Collection of Analytical and Problematic Tasks in the course on Principles of the creation of Composite materials, KIKhM, Moscow, 1999.

[124] A. A. Berlin and F. A. Shutov. Reinforced Gas-expanded Plastics, Khimiya, Moscow, 1980.

[125] V. Yakushin, L. Bel'kova, and I. Sevastyanova. Properties of rigid polyurethane foams filled with glass microspheres. *Mechanics of Composite Materials*, 48:579–586, 2012.

[126] J. Ferreira, C. Capela, and J. Costa. A study of the mechanical behaviour of fibre reinforced hollow microspheres hybrid composites. *Composites Part A: Applied Science and Manufacturing*, 41:345–352, 2010.

[127] H. S. Kim and H. H. Oh. Manufacturing and impact behaviour of syntactic foam. *Journal of Applied Polymer Science*, 76:1324–1328, 2001.

[128] E. Barber, J. Nelson, and W. Beck. Improving properties in rigid urethane foams using glass bubbles. *Journal of Celluar Plastics*, 13:383–387, 1977.

[129] J. A. Hagarman, J. P. Cunnion, and B. W. Sands. Formulation and physical properties of polyurethane foam incorporating hollow microspheres. *Journal of Celluar Plastics*, 21:406–408, 1985.

[130] I. V. Masik, N. V. Sirotinkin, S. V. Yatsenko, and S. V. Vakulenko. Effect of glass microspheres on the properties of rigid polyurethane foams. *Plasticheskie Massy*, 30:41–46, 2002.

[131] X. C. Bian, J. H. Tang, and Z. M. Li. Flame retardancy of hollow glass microsphere/rigid polyurethane foams in the presence of expandable graphite. *Journal of Applied Polymer Science*, 109:1935–1943, 2008.

[132] F. Wang, Q. Tang, X. Duan, J. Liang, N. Wang, H. Liu, and H. Liu. Effect of modified sepiolite nanofibers and hollow glass microspheres on performance of rigid polyurethane foams composite materials. *Nanoscience and Nanotechnology Letters*, 6:524–531, 2014.

[133] A. Pellegrino, V. L. Tagarielli, R. Gerlach, and N. Petrinic. The mechanical response of a syntactic polyurethane foam at low and high rates of strain. *International Journal of Impact Engineering*, 75:214–221, 2015.

[134] D. Luong, V. C. Shunmugasamy, O. Strbik, and N. Gupta. High Strain Rate Compressive Behavior of Polyurethane Resin and Polyurethane/Al_2O_3 Hollow Sphere Syntactic Foams. *Journal of Composites*, 2014:1–10, 2014.

[135] M. S. Attia, S. A. Meguid, and H. Nouraei. Nonlinear finite element analysis of the crush behaviour of functionally graded foam-filled columns. *Finite Elements in Analysis and Design.*, 61:50–59, 2011.

[136] Y. Hangai, N. Kubota, T. Utsunomiya, H. Kawahima, O. Kuwazuru, and N. Yoshikawa. Drop weight impact behaviour of functionally graded aluminium foam consisting of A1050 and A6061 aluminium alloys. *Materials Science and Engineering A*, 639:597–603, 2015.

[137] C. Y. Huang and Y. L. Chen. Design and impact resistant analysis of functionally graded $Al_2 - ZrO_2$ ceramic composite. *Materials and Design*, 91:294–305, 2016.

[138] A. H. Brothers and D. C. Dunand. Mechanical properties of a density-graded replicated aluminum foam. *Materials Science and Engineering A*, 489:439–443, 2008.

[139] N. Gupta and W. Ricci. Comparison of compressive properties of layered syntactic foams having gradient in microballoon volume fraction and wall thickness. *Materials Science and Engineering: A*, 427:331–342, 2006.

[140] N. Gupta, S. K. Gupta, and B. J. Mueller. Analysis of a functionally graded particulate composite under flexural loading conditions. *Materials Science and Engineering: A*, 485:439–447, 2008.

[141] A. G. Mamalis, K. N. Spentzas, N. G. Pantelelis, D. E. Manolakos, and M. B. Ioannidis. A new hybrid concept for sandwich structures. *Composite Structures*, 83:335–340, 2008.

[142] J. A. Newman. Frontiers in Head and Neck Trauma: Clinical and Biomechanical, IOS Press Inc., Burke, Virginia, 1998.

[143] F. A. DiLorenzo. Power and Bodily Injury, SAE 760014, Automotive Engineering Congress and Exposition, Detroit, 1976, 1976.

[144] J. A. Newman. International Conference on the Biomechanics of Impact (IRCOBI), Zurich, Switzerland, 1986.

[145] L. Cui, S. Kiernan, and M. Gilchrist. Designing the energy absorption capacity of functionally graded foam materials. *Materials Science and Engineering: A*, 507:215–225, 2009.

[146] Lamborghini, Technical specifications of Aventador LP 700-4, Automobili Lamborghini, 2014. `http://www.lamborghini.com/en/models/aventador-lp-700-4/technical-specifications/`.

[147] N. Jones. Structural Impact, Cambridge UK, Cambridge University Press, 2nd edition, 1997.

[148] G. L. Farley. Effect of specimen geometry on the energy absorption capability of composite materials. *Journal of Composite Materials*, 20:390–400, 1986.

[149] D. W. Schmusser and I. E. Wickliffe. Impact energy absorption of continuous fibre composite tubes. *Engineering Materials and Technology*, 109:72–77, 1987.

[150] S.R. Guillow, G. Lu, and R.H. Grzebieta. Quasi-static axial compression of thin-walled circular aluminium tubes. *International Journal of Mechanical Sciences*, 43:2103–2123, 2001.

[151] S. S. Hsu and N. Jones. Quasi-static and dynamic axial crushing of thin-walled circular stainless steel, mild steel and aluminium alloy tubes. *International Journal of Crashworthiness*, 9:195–217, 1983.

[152] F. Schneider and N. Jones. Impact of thin-walled high-strength steel structural sections. *Proceedings of the institution of Mechanical Engineers, Part D*, 218:131–158, 2004.

[153] A. G. Olabi, E. Morris, and M. S. J. Hashmi. Metallic tube type energy absorbers: a synopsis. *Thin-Walled Structures*, 45:706–726, 2007.

[154] S. C. K. Yuen and G. N. Nurick. The energy-absorbing characteristics of tubular structures with geometric and material modifications: an overview. *Applied Mechanics Reviews*, 61:1–15, 2008.

[155] D. Karagiozova and M. Alves. Dynamic elastic-plastic buckling of structural elements: a review. *Applied Mechanics Reviews*, 61:1–15, 2008.

[156] P. H. Thornton. Energy Absorption in Composite Structures. *Journal of Composite Materials*, 13:247–262, 1979.

[157] P. H. Thornton and J. Edwards. Energy Absorption in Composite Tubes. *Journal of Composite Materials*, 16:521–545, 1982.

[158] P. H. Thornton, J. J. Harwood, and P. Beardmore. Fiber-reinforced plastic composites for energy absorption purposes. *Composites Science and Technology*, 24:275–298, 1985.

[159] G. L. Farley. Energy absorption of composite materials. *Composite Materials*, 17:267–279, 1983.

[160] K. R. F. Andrews, G. L. England, and E. Ghani. Classification of the axial collapse of cylindrical tubes under quasi-static loading. *International Journal of Mechanical Sciences*, 25:687–696, 1983.

[161] H. Hamada, J.C. Coppola, D. Hull, Z. Maekawa, and H. Sato. Comparison of energy absorption of carbon/epoxy and carbon/PEEK composite tubes. *Composites*, 23:245–252, 1992.

[162] S. R. Reid. Plastic deformation mechanisms in axially compressed metal tubes used as impact energy absorbers. *International Journal of Mechanical Sciences*, 35:1035–1052, 1993.

[163] C.H. Chiu, C.K. Lu, and C.M. Wu. Crushing characteristics of 3-D braided composite square tubes. *Journal of Composite Materials*, 31:2309–2327, 1997.

[164] D.D. Dubey and A.J. Vizzini. Energy absorption of composite plates and tubes. *Journal of Composite Materials*, 32:158–176, 1998.

[165] G. C. Jacob, J. F. Fellers, S. Simunovic, and J. M. Starbuck. Energy absorption in polymer composites for automotive crashworhiness. *Journal of Composite Materials*, 36:813–849, 2002.

[166] A.G. Mamalis, Y.B. Yuan, and G.L. Viegelahn. Collapse of thin-wall composite sections subjected to high speed axial loading. *International Journal of Vehicle Design*, 13:564–579, 1992.

[167] G. L. Farley and R. M. Jones. Energy-absorption capability of composite tubes and beams, National Aeronautics and Space Administration, Langley Research Center Hampton, Virginia. 1989.

[168] G. L. Farley and R. M. Jones. Crushing Characteristics of Continuous Fiber-Reinforced Composite Tubes. *Composite Materials*, 26:37–50, 1992.

[169] H. W. Song, Z. M. Xie, X. W. Du, and G. F. Zhao. Axial impact behaviour and energy absorption efficiency of composite wrapped metal tubes. *International Journal of Impact Engineering*, 24:385–401, 2000.

[170] H-W Song Z-M Xie, Z-M Wan and X-W Du. An Analysis of Impact Energy Absorption of Glass-Epoxy Tubes, 1998.

[171] H. Hamada and S. Ramakrishna. Energy Absorption Characteristics of Crash Worthy Structural Composite Materials. *Key Engineering Materials*, 9:259–279, 1998.

[172] A. G. Mamalis, D. E. Manolakos, and G. L. Viegelahn. Crashworth Behaviour of Thin-Walled Tubes of Fiberglass Composite Material Subjected to Axial Loading. *Composite Materials*, 24:72–91, 1990.

[173] H. W. Song, X. W. Du, and G. F. Zhao. Energy Absorption Behavior of Double-Chamfer Triggered Glass/Epoxy Circular Tubes. *Journal of Composite Materials*, 36:2183–2198, 2002.

[174] I. J. McGregor, D. J. Meadows, C.E. Scott, and A. D. Seeds. In: N. Jones, T. Wierzbicki, editors of structural crashworthiness and failure: impact performance of aluminum structures, Elsevier Applied Science, 1993.

[175] P. Buchan and J. Chen. Blast resistance of FRP composites and polymer strengthened concrete and masonary structures - A state-of-the-art review. *Composites Part B: Engineering*, 38:509–522, 2007.

[176] Md Fuad Shah Koslan, Ahmad Mujahid A hmad Zaidi, Mohd Zaid Othman, Shohaimi Abdullah, and Suresh Thanakodi. The effect of mesh sizing toward deformation result in computational dynamic simulation for blast loading application. *Moden Applied Science*, 7:23–29, 2013.

[177] M. I. Okereke, A. I. Akpoyomare, and M. S. Bingley. Virtual tesiting of advanced composites, cellular materials and biomaterials: A review. *Composites: Part B*, 60:637–662, 2014.

[178] D. Bonorchis and G. N. Nurick. The influence of boundary conditions on the loading of rectangular plates subjected to localised blast loading importance in numerical simulations. *International Journal of Impact Engineering*, 36:40–52, 2009.

[179] D. Ambrosini, B. Luccioni, G. Nurick, G. Langdon, and N. Jacob. The effect of confinement and stand-off distance in blast tests. *Mechanica Computacional*, XXVII:343–362, 2009.

[180] AUTODYN-2D and 3D. v6.1 user documentation. Horsham, United Kingdom: Century Dynamics Incorporated, 2005.

[181] ABAQUS 6.14. *Analysis User's Manual*. Warrington, Chesire, Dassault Systems Simulia Corporation, 2014.

[182] LS-DYNA. *User's Manual*. Livermore, California, Livermore Software Technology Corporation, 2007.

[183] V. Tita and M. F. C. Junior. Numerical simulation of anisotropic polymeric foams. *Latin American Journal of Solids and Structures*, 1:1–21, 2012.

[184] L. Gong, S. Kyriakides, and W.-Y. Jang. Compressive response of open-cell foams. Part I: Morphology and elastic properties. *Solids and Structures*, 42:1355–1379, 2004.

[185] W. Yan, E. Durif, Y. Yamada, and C. Wen. Crushing simulation of foam-filled aluminium tubes, materials transactions. *Materials Transactions*, 48:1901–1906, 2007.

[186] S. W. Tsai and E. M. Wu. A general theory of strength for anisotropic materials. *Journal of Composite Materials*, 5:58–80, 1971.

[187] Z. Hashin. Failure criteria for uni-directional fibre composites. *Applied Mechanics*, 47:329–334, 1980.

[188] L. Iannucci. Progressive failure modelling of woven carbon composite under impact. *International Journal of Impact Engineering*, 32:1013–1043, 2006.

[189] T. E. Tay, G. Liu, V. B. C. Tan, X. S. Sun, and D. C. Pham. Progressive failure analysis of composites. *Journal of Composite Materials*, 42:1920–1966, 2008.

[190] E. J. Barbero. *Finite Element analysis of Composite Materials Using Abaqus*. Taylor and Francis Group, 2013.

[191] B. P. Bussadori, K. Schuffenhauer, and A. Scattina. Modelling of CFRP crushing structures in explicit crash analysis. *Composites: Part B*, 60:725–735, 2014.

[192] G. Zhang, B. Wang, L. Ma, J. Xiong, and L. Wu. Response of sandwich structures with pyramidal truss cores under the compression and impact loading. *Composite Structures*, 100:451–463, 2013.

[193] K. H. Safari, J. Zamani, S. M. R. Khalili, and S. Jalili. Experimental, theoretical, and numerical studies on the response of square plates subjected to blast loading. *Materials Science*, 46:805–816, 2011.

[194] J. H. Ha, N. H. Yi, J. K. Choi, and J. H. J. Kim. Experimental study on hybrid CFRP-PU strengthening effect on RC panels under blast loading. *Composite Structures*, 93:2070–2082, 2011.

[195] G. H. Farrow, G. N. Nurick, and G. P. Mitchell. Modelling of impulsively loaded circular plates using the ABAQUS finite element code. In: Symposium Finite Element Methods in South Africa; Stellenbosch, South Africa, 1995.

[196] N. Jones. Damage of plates due to impact, dynamic pressure and explosive loads. *Latin American Journal of Solids and Structures*, 10:767–780, 2012.

[197] B. Hopkinson. British Ordinance Board Minutes, 13563, 1915.

[198] C. Cranz. Lehrbuch der Ballistik, Springer-Verlag, Berlin, 1926.

[199] C. N. Kingery, G. Bulmash, and U. A. B. R. Laboratory. Air blast parameters from TNT spherical air burst and hemispherical surface burst, Ballistic Research Laboratories, 1984.

[200] P. Tan, B. Lee, and C. Tsangalis. Finite element analysis of sandwich panels subjected to shock tube blast loadings. *Journal of Sandwich Structures and Materials*, 13:263–278, 2010.

[201] J. W. Nam, H. J. Kim, S. B. Kim, N. H. Yi, and J. J. H. Kim. Numerical evaluation of the retrofit effectiveness for GFRP retrofitted concrete slab subjected to blast pressure. *Composite Structures*, 92:1212–1222, 2010.

[202] C. Soutis, G. Mohamed, and A. Hodzic. Modelling the structural response of GLARE panels to blast load. *Composite Structures*, 94:267–276, 2011.

[203] Z. L. Xing, K. L. Sheng, Y. Z. Tang, and J. J. Huang. Comparative Analysis of the numerical simulation results using ConWep algorithm with the

experimental results. *Applied Mechanics and Materials*, 90-93:3180–3185, 2011.

[204] CONWEP. Technical Manual TM5-855-1, Fundamentals of Protective Design for Conventional Weapons, US Department of the Army Washington, DC, 1986.

[205] C. N. Kingery, G. Bulmash, and U. A. B. R. Laboratory. The shape of the blast wave: studies of the Friedlander equation, Presented at the 21st International Symposium on Military Aspects of Blast and Shock, Israel, 2010.

[206] O. C. Zienkiewicz, R. L. Taylor, and P. Nithiarasu. The Finite Element Method for Fluid Dynamics, Butterworth-Heinemann, Oxford, UK, 6th edition, 2005.

[207] H. A. Bethe, K. Fuchs, J. O. Hirschfelder, J. L. Magee, R. E. Peierls, and J. von Neumann. "The point source solution" in *Blast Wave*, Eds., Report No. LA-2000, Los Almos Scientific Laboratory, 1958.

[208] T. Vo, Z. W. Guan, W. J. Cantwell, and G. K Schleyer. Modelling of the low-impulse blast behaviour of fibre-metal laminates based on different aluminium alloys. *Composites Part B: Engineering*, 44:141–151, 2013.

[209] J. A. Guerrero, J. P. Sánchez, and F. T. Dias. Blast wave dynamics: The influence of the shape of the explosive. *Journal of Hazardous Materials*, 331:189–199, 2017.

[210] E. L. Lee, H. C. Horning, and J. W. Kury. Adiabatic expansion of high explosives detonation products, Lawrence Livermore National Laboratory, University of Califonia, Livermore, 1968.

[211] Easy Composites Ltd. `www.easycomposites.co.uk`.

[212] ANSYS Incorporated. ANSYS Workbench Users Guide, ANSYS Incorporated, USA, 2010.

[213] Covestro LLC. `http://www.tpu.covestro.com`.

[214] R. S. Birch and N. Jones. Measurement of impact loads using a laser Doppler velocimeter. *Proceedings of the Institution of Mechanical Engineers*, 204, 1990.

[215] E. Wu and L. C. Chang. Woven glass/epoxy laminates subjected to projectile impact. *International Journal of Impact Engineering*, 16:607–619, 1995.

[216] K. S. Vecchio and F. Jiang. Improved Pulse Shaping to Achieve Constant Strain Rate and Stress Equilibrium in Split Hopkinson Pressure Bar Testing. *Metallurgical and Materials Transactions A*, 103:1–5, 2007.

[217] Z. Li and J. Lambros. Determination of the dynamic response of brittle composites by the use of the split hopkinson pressure bar. *Composites Science and Technology*, 59:1097–1107, 1999.

[218] G. N. Nurick, S. Mahoi, and G. S. Langdon. The response of plates subjected to loading arising from the detonation of different shapes of plastic explosives. *International Journal of Impact Engineering*, 89:102–113, 2016.

[219] N. Jacob, G. N. Nurick, and G. S. Langdon. The effect of stand-off distance on the failure of fully clamped circular mild steel plates subjected to blast loads. *Engineering Structures*, 29:2723–2736, 2007.

[220] Z. Petrovic and J. Ferguson. Polyurethane elastomers. *Prog. Polym. Sci.*, 16:695–836, 1991.

[221] H. Zhao, I. Elnasri, and S. Abdennadher. An experimental study on the behaviour under impact loading of metallic cellular materials. *International Journal of Mechanical Sciences*, 47:757–774, 2005.

[222] D. K. Balch, J. O'Dwyer, G. R. Davis, C. M. Cady, G. T. Gray III, and D. C. Dunand. Plasticity and damage in aluminum syntactic foams deformed under dynamic and quasi-static conditions. *Material Science and Engineering A*, 391:408–417, 2005.

[223] G. R. Cowper and P. S. Symonds. Strain hardening and strain rate effect in the impact loading of cantilever beams, Brown University, Division of Applied Mathematics, Report No. 28. 1957.

[224] W. Q. Shen and N. Jones. Dynamic response and failure of fully clamped circular plates under impulsive loading. *International Journal of Engineering*, 38:2655–2665, 1993.

[225] G. R. Johnson and W. H. Cook. Fracture characteristics of three metals subjected to various strains, strain rates, temperatures and pressures. *Engineering Fracture Mechanics*, 21:31–48, 1985.

[226] D. R. Lesuer. Experimental investigations of material models for Ti-6Al-4V titanium and 2024-T3 aluminum. Technical report, Lawrence Livermore National Laboratory, Livermore, CA, 2000.

[227] V. S. Deshpande and N. A. Fleck. Isotropic constitutive models for metallic foams. *Journal of the Mechanics and Physics of Solids*, 48:1253–2000, 2000.

[228] B. A. Gama and J. W. Gillespie Jr. Finite element modeling of impact, famage evolution and penetration of thick-section composites. *International Journal of Impact Engineering*, 38:181–197, 2011.

[229] J. Zhou, Z. W. Guan, and W. J. Cantwell. Modelling compressive crush of composite tube reinforced foam sandwiches, ICCM2014, Cambridge, England, 2017.

[230] M. I. H. Smith. *The Compressive Response of Novel Lattice Structures Subjected to Static and Dynamic Loading.* PhD thesis, Department of Engineering, University of Liverpool, 2012.

Appendices

Appendix A

Mould design for the manufacturing of the TSPU

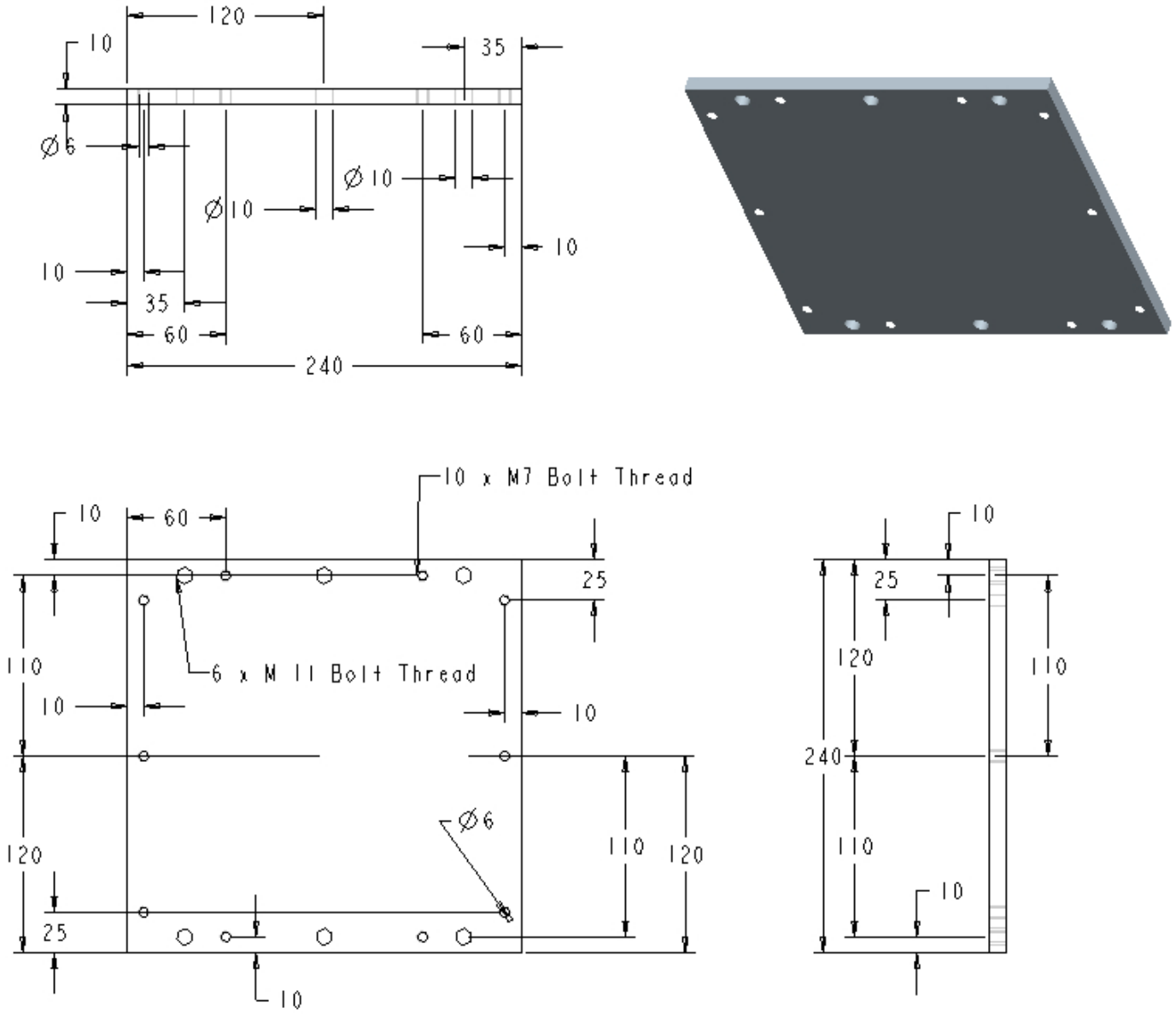

Figure A.1: Dimension of top plate (mm).

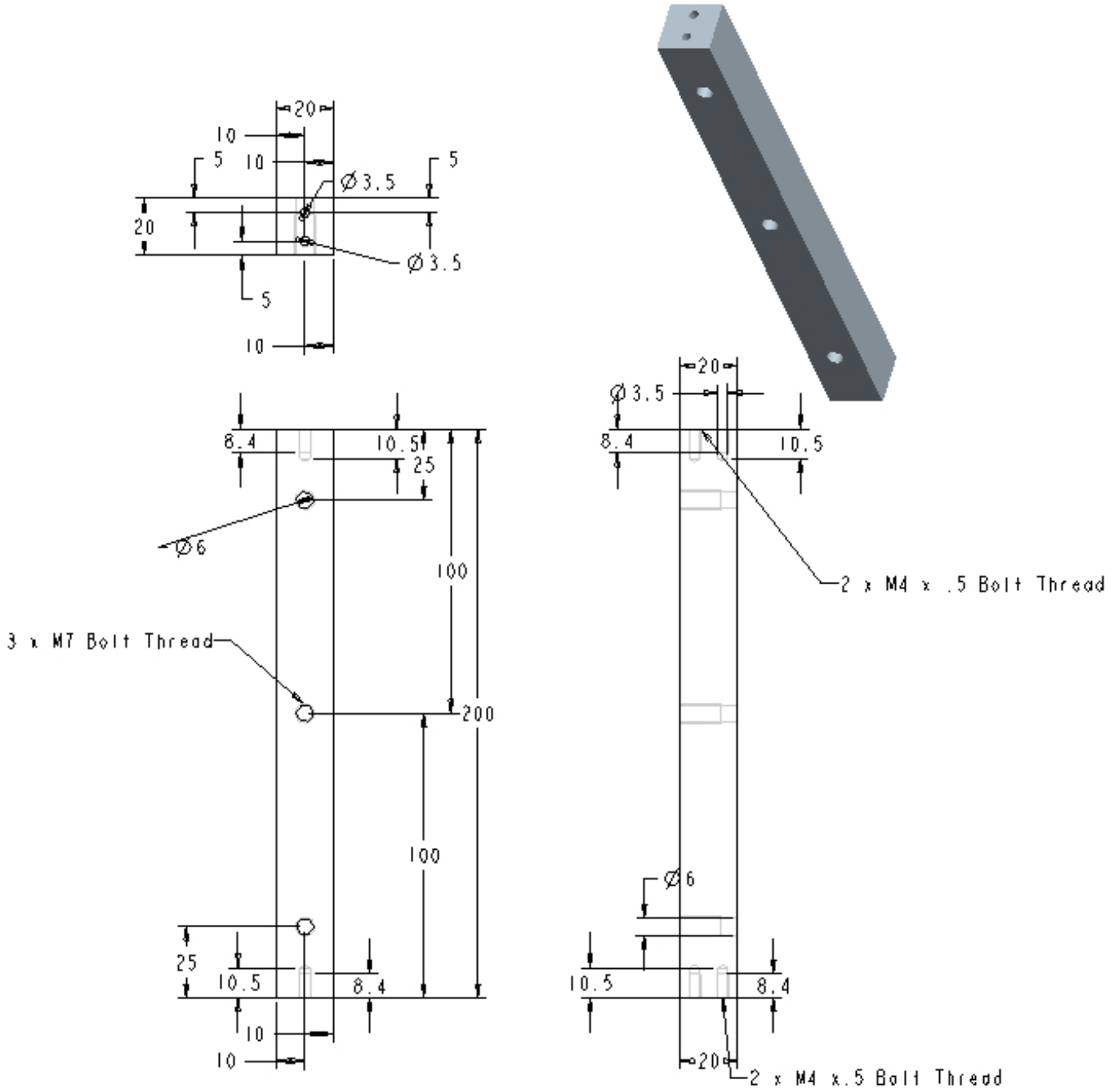

Figure A.2: Dimension of sections 1 and 2 (mm).

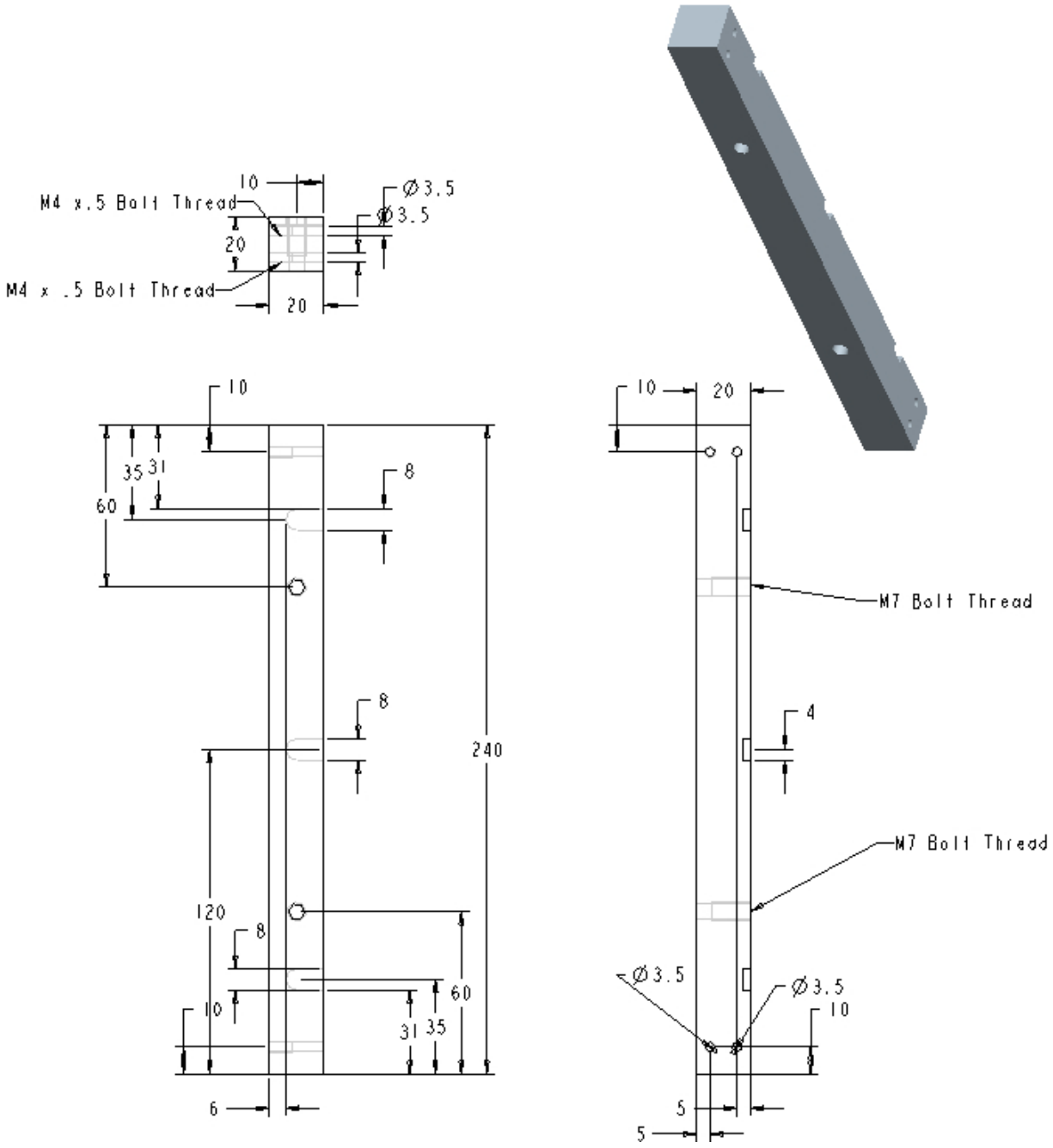

Figure A.3: Dimension of section 3 and 4 (mm).

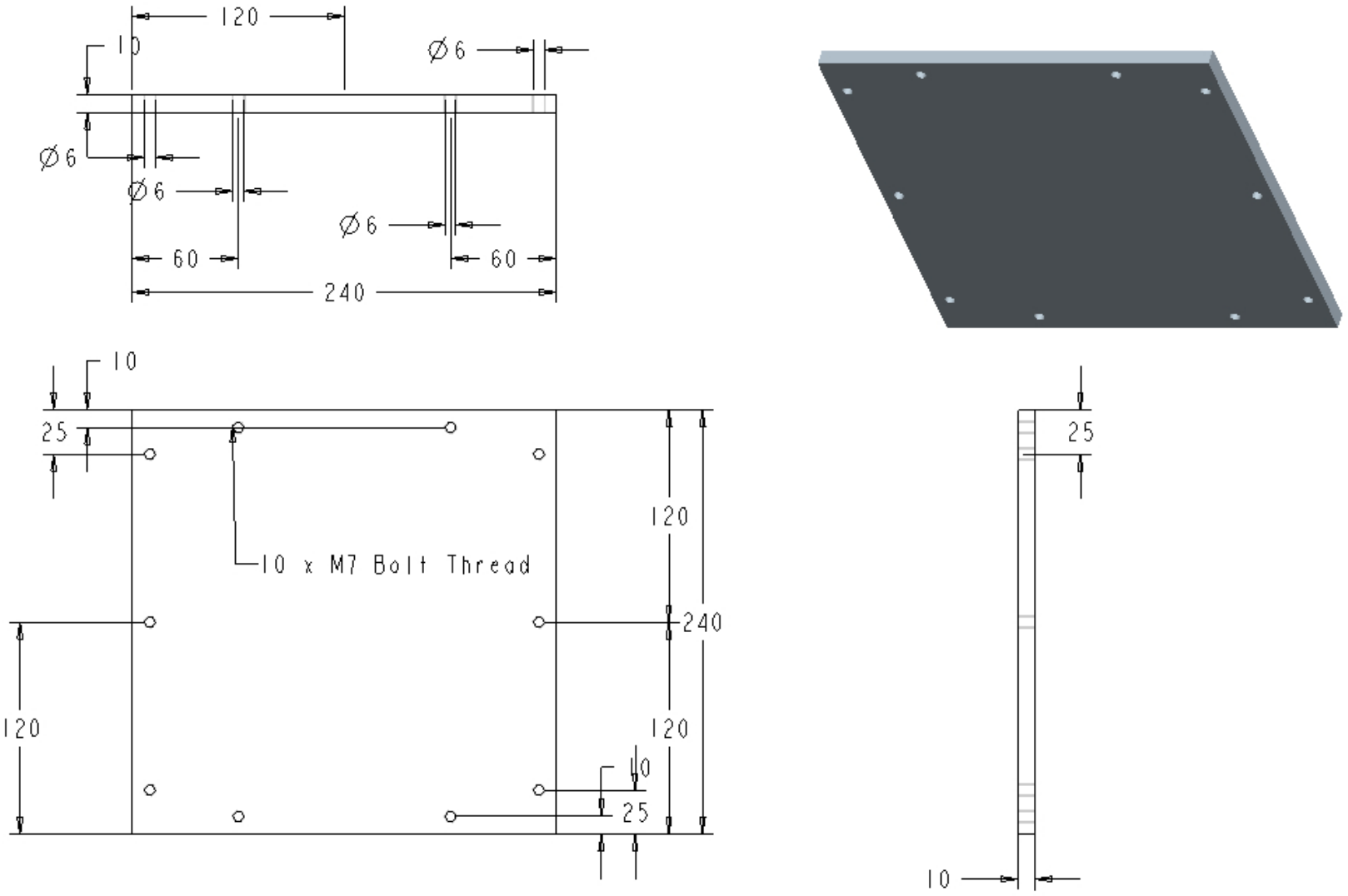

Figure A.4: Dimension of the bottom plate (mm).

Appendix B

SHPB Matlab code for data processing

```
clear;
clf;
load data_file.csv;

y=data_file(:,1);z=data_file(:,2);t=data_file(:,3);
%y = Channel 1, z= Channel 2, t = time

%Remove zero shift
n=100;
a1=sum(y(1:n))/n;
a2=sum(z(1:n))/n;
a3=0;

yi=y(1:1200)-a1;
zi=z(1:1200)-a2;

```

```
%Time increment
ti=t(1:1200)./5e-7;
ti1=t(1:1200)./5e-7;

figure(1)      %adjustments of waves
p1=-10;p2=-90;q=-10;
%p1 = start point, p2 = end point,q = transmission wave
qq=400+p2-p1;    %qq = interval length
R=y(200+p1:600+p2)-a1;
Rt=t(200+p1:600+p2);
F=y(600+q:600+qq+q)-a1;
T=z(600+q:600+qq+q)-a2;

plot(Rt,R,'-',Rt,F,'-.',Rt,T,'--');
%Plot incident (R),reflected (F),and Transmitted wave (T)
axis tight;
grid on

legend('Incident','Reflected','Transmitted')
xlabel('Time/s');
ylabel('Voltage/V');

R1=y(200+p1:600+p2)-a1;
Rt1=t(200+p1:600+p2);
RRR=[Rt1,R1]; %Extract incident wave seperately

%Filter data using FFT-based method
lv1=fir1(100,0.3); %Filter process, i.e. smoothing data
```

```
45 R1=fftfilt(lv1,R);
46 T1=fftfilt(lv1,T);
47 F1=fftfilt(lv1,F);
48 %Collect data for time, reflected, incident and
       transmitted waves
49 EEE=[Rt,F,T,R];
50 EE=[Rt,F,T];
51 E=[Rt,F1,T];
52
53 t=EE(:,1);
54 ur=EE(:,2);  %Reflection and transmission signals
55 ut=EE(:,3);
56
57 lv1=fir1(50,0.01);  %Filter process, i.e. smoothing data
58 ur1=fftfilt(lv1,ur);
59 ut1=fftfilt(lv1,ut);
60
61 figure(2)
62 subplot(2,1,1);
63 plot(t,ur1);
64 grid on
65 xlabel('Time (s)');
66 ylabel('Reflection');  %Reflection signal
67 hold on;
68 subplot(2,1,2);
69 plot(t,ut1);
70 grid on
71 xlabel('Time (s)');
```

```
72 ylabel('Transmission');     %Transmission signal
73 hold off;
74
75 er=abs(ur1./1600);    %Reflection strain
76 et=abs(ut1./1600);    %Transmission strain
77
78 E=7.2e10;             %Young's Modulus (bar)
79 p=2.7e3;              %Density (bar)
80 L=8.46/1000;          %Length (bar)
81 d=14.5/1000;          %Diameter (bar)
82 ds=8/1000;           %Diameter (specimen)
83 Co=sqrt(E/p);         %Wave velocity
84 A=(pi*d^2)/4;         %Cross-sectional area (bar)
85 As=(pi*ds^2)/4;       %Cross-sectional area (specimen)
86
87 s=er;
88 dt=1e-6;
89 X1=zeros(length(s));
90 xx1=X1(:,1);
91 n=length(s);
92 xx1(1,1)=0;
93
94 for i=2:1:n;
95     xx1(i,1)=xx1(i-1,1)+(s(i,1)-s(i-1,1))*dt/2;
96     xx1(i,1)=xx1(i,1)+s(i-1,1)*dt;
97 end
98 %Calculate nominal stress, strain and strain rate
99 NS=(xx1*2*Co)/L;          %Nominal Strain
```

```
100 NST=(E*(A/As).*et)/1e6;  %Nominal Stress
101 SR=(2*Co/L).*er;         %Strain rate
102 %Calculate true stress and strain
103 TS=log(1./(1-NS));       %True strain
104 TST=NST.*(1.-NS);          %True stress
105
106 figure(3)       % Plot Nominal Stress vs Nominal Strain
107 plot(NS,NST);
108 grid;
109 xlabel('Nominal Strain');
110 ylabel('Nominal Stress');
111
112 figure(4)              %Plot Strain rate vs Nominal Strain
113 plot(NST,SR);
114 grid;
115 xlabel('Nominal Strain');
116 ylabel('Strain rate');
117
118 figure(5)              %Plot True Stress vs True Strain
119 plot(TS,TST);
120 grid;
121 xlabel('True Strain');
122 ylabel('TrueStress');
123
124 %Extract stress, strain and strain-rate data
125 Z=[NS,NST,SR,TS,TST];
```